MULTIPLEXED LABEL-FREE INTEGRATED PHOTONIC BIOSENSORS

A Thesis
Presented to
The Academic Faculty

by

Farshid Ghasemi

In Partial Fulfillment
of the Requirements for the Degree
Doctor of Philosophy in the
School of Electrical and Computer Engineering

Georgia Institute of Technology
May 2015

MULTIPLEXED LABEL-FREE INTEGRATED PHOTONIC BIOSENSORS

Approved by:

Professor Gee-Kung Chang,
Committee Chair
School of Electrical and Computer Engineering
Georgia Institute of Technology

Professor Ali Adibi, Advisor
School of Electrical and Computer Engineering
Georgia Institute of Technology

Professor Stephen E. Ralph
School of Electrical and Computer Engineering
Georgia Institute of Technology

Professor John Cressler
School of Electrical and Computer Engineering
Georgia Institute of Technology

Professor Haomin Zhou
School of Mathematics
Georgia Institute of Technology

Date Approved:

ACKNOWLEDGEMENTS

I want to thank my family, to whom I am indebted the most. No attempt at a list of what they have provided to me would do their kindness justice. I am thankful to Professor Ali Adibi for his advise and support of my PhD research. I would like to thank my dissertation committee Professors Gee-Kung Chang, Stephen Ralph, John Cressler, and Haomin Zhou for the their discussions and comments on this work. My friends in our group have had invaluable contribution to my work. The initial form of the setup I carried out the majority of my experiments on was assembled by Ehsan Shah Hosseini, with the LabView software development by JD and Siva. Maysam Chamanzar helped me with the alignment of the setup and dealing with its various issues. I would also thank Reza (Ali) Eftekhar for his comments on data interpretation and the set up of the experiments. Just as helpful were Maysam and Amir Hossein Atabaki's ideas on fabrication process development and experiment design. Thanks to Arash Karbaschi for characterization discussions and ideas; Qing Li, Majid Sodagar, and Murtaza Askari for device design and nanofabrication; Charles H. Camp, Jr. for the discussions on biosensing experiments; and Hamed Moussavi and Reza Abbaspour for their help with performing surface chemistry protocols and the realization of microfluidics. This list goes on and on, and I would like to thank all other friends not mentioned here. Thanks to the proofreaders of this dissertation: Majid, Razi Dehghan-Nassiri, Ahmad Usman, and Hossein Taghinejad.

This research has benefited from the kind assistance and advise of technical and administrative people at Georgia Tech and Emory University. Especially, I would like to express my gratitude to Dr. David Gottfried for his numerous helpful comments in relation to biosensors. Dr. Mahmoud Mahmoud was kind to provide me with

his knowledge on surface chemistry and help me perform part of the optimization of surface activation protocols in Professor El-Sayed's labs, especially at the initial stages when I was new to the field. Cleanroom managers and staff at the Institute for Electronics and Nanotechnology (Professors Meindl and Brand, Gary, Devin, Eric, Vinny, John, Charlie Suh, Charlie Turgeon, Jie, Mikkel, Hang, Thomas, and others) always made their best to make this nanofabrication facility available for a variety of processes. I believe their dedication remarkably contributes to IEN being one of the best facilities of its kind in the US. Just as helpful were the core facilities of the Institute for Bioengineering and Biosciences (IBB), and especially fluorescence microscopy core. I want to thank Andrew Shaw in specific for his technical assistance with the microscopes. Our collaborators at Dr. Richard Cummings' group at Emory University; Dr. X. Song, Y. Lasanajak, and J. Heimburg-Molinaro; provided me with the knowledge required to work with glycans and lectins used in this dissertation. I also appreciate the students who run the Invention Studio at Mechanical Engineering department of Georgia Tech (ULIs, as they call themselves) for their effective assistance, without which the realization of microfluidics would have been a more difficult challenge.

In the course of my research I had the fortune to benefit from the vision and advise of numerous professors at Georgia Tech. Thank you to Professor Seth Marder for his advise on surface chemistry, Thomas Gaylord for the discussions on interferometry, Kurt Wiesenfeld for cavity thermodynamics, Peter Hesketh and James Gole for low-temperature oxide deposition, and Brani Vidakovic and Vladimir Koltchinskii for the discussions on statistical noise analysis and extreme value theory.

Outside the realm of research, I truly appreciate all my friends in Atlanta who enriched my life in these years. May we have many more times together.

TABLE OF CONTENTS

LIST OF TABLES

LIST OF FIGURES

SUMMARY

Optics and photonics enable important technological solutions for critical areas such as health, communications, energy, and manufacturing. Novel nanofabrication techniques, on the other hand, have enabled the realization of ever shirking devices. On-chip photonic micro-resonators, the fabrication of which was made possible in the recent decade thanks to the progress in nanofabrication, provide a sensitive and scalable transduction mechanism that can be used for biochemical sensing applications.

The recognition and quantification of biological molecules is of great interest for a wide range of applications from environmental monitoring and hazard detection to early diagnosis of diseases such as cancer and heart failure. A sensitive and scalable biosensor platform based on an optimized array of silicon nitride microring resonators is proposed for multiplexed, rapid, and label-free detection of biomolecules. The miniature dimension of the proposed sensor allows for the realization of handheld detection devices for limited-resource and point-of-care applications. To realize these sensors, the design, fabrication, stabilization, and integration challenges are addressed. Especially, the focus is placed on solving a major problem in using resonance-based integrated photonic sensors (i.e., the insufficiency of wavelength scan accuracy in typical tunable lasers available) by using an interferometric referencing technique for accurate resonance tracking. This technique can improve the limit of detection of the proposed sensor by more than one order of magnitude. The method does not require any temperature control or cooling, and the biosensor platform does not require narrow linewidths necessary for the biosensors based on ultrahigh quality factor resonators, thus enabling low-cost and reliable integration on the biosensor platform.

CHAPTER I

INTRODUCTION

Compact, sensitive, and low-cost sensors are of great interest in diverse areas such as medicine, threat-agent detection, automotive and aerospace industries, environmental monitoring, agriculture, food safety, and pharmacology. Advances in nanotechnology have enabled the fabrication of lab-on-chip sensors that serve this purpose. There is a sizable demand for biosensors of different kinds around the globe. The combined annual growth rate (CAGR) of the biosensor market for the 2008-2018 period is estimated to be 11% in Asia-Pacific, and 10.7% in the U.S. The global market for biosensors is estimated to reach US$16.8 billion by 2018 [1]. The projected biosensor market sectors for 2016 in Figure 1 shows that about two-thirds of the demand in the future years is expected to come from medical tests and diagnostic applications. The share of photonic biosensors out of this market is valued at an estimated amount of $0.5 billion, with a CAGR of approximately 9% [2].

On-chip electro-optical devices have a great promise for the realization of lab-on-chip biochemical sensors. The definition of the International Union of Pure and Applied Chemistry (IUPAC) for an electrochemical biosensor is "a self-contained integrated device which is capable of providing specific quantitative or semi-quantitative analytical information using a biological recognition element which is in direct spatial contact with a transducer element."[3] Scores of photonic [4], mechanical [5], and electrochemical [6–8] sensing mechanisms have been proposed and integrated into miniaturized sensor platforms to address biological and chemical detection needs.

While optical sensors rely on changes in the optical characteristics of the sensor

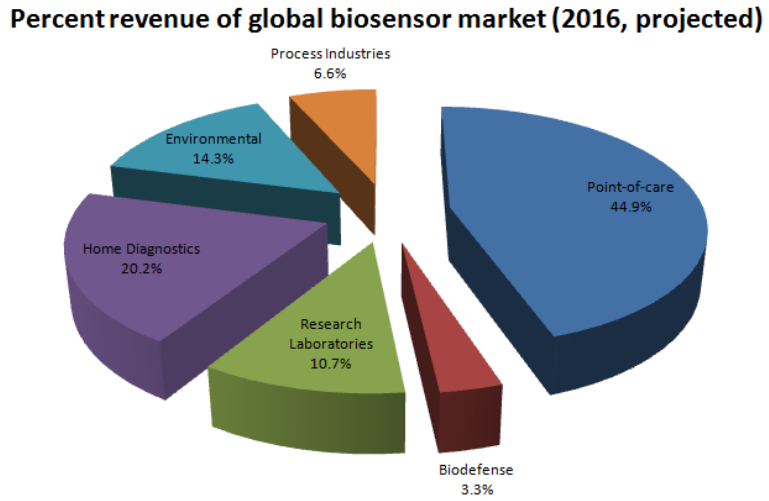

Figure 1: Projected percent revenue of global biosensor market for 2016 [9].

(such as resonance or light phase) for monitoring the environmental changes, electrochemical sensors rely on electrical potential (in the case of potentiometric transducers) or current (as in the case of amperometric transducers) detected using an electrode in contact with the biological recognition element [7]. I briefly introduce and compare major, relevant works on different types of integrated biosensors in subsequent sections.

1.1 Mechanical and Electrochemical Integrated Sensors

The binding of the target molecules to the surface of a free-standing structure causes a surface-tension and results in bending of the structure. Surface-stress mechanical sensors record the deflection of a cantilever as a measure of the number of molecules binding to the surface of the cantilever [10]. The static-mode deflection of a gold-coated silicon (Si) cantilever has been demonstrated to result in a limit of detection (LOD) of about 1nM for detecting proteins in solution phase [11]. In a static-mode sensor the cantilever does not move as long as the number and configuration of the molecules on its surface remain the same. In a dynamic-mode mechanical sensor, however, the cantilever resonates, and the detection measure is the resonance shift of

the cantilever [12]. The quality factor of the resonator (i.e., the cantilever) is important for an accurate detection. To increase the quality factor (Q) of these sensors, two common techniques include: designing the device to operate at higher resonance frequencies (by shrinking the dimensions or using higher order modes [13, 14]), and containing the test fluid inside the cantilever using suspended microchannel resonators (SMRs) [15]. Because of the fluid viscous damping, mechanical sensors typically have a much better mass resolution in vacuum than solution phase. By dynamic-mode *in vacuo* detection, the femtomolar detection of prostate specific antigen (PSA) in serum has been demonstrated [16]. Compared to micron-sized mechanical sensors, fluid-based [17] and *in vacuo* [18] quartz crystal microbalance (QCM) devices have larger dimensions (few centimeters), though they can also achieve femtomolar LODs.

Another major category of biosensors utilizes electrochemical mechanisms for sensing. The work of Clark and Lydon in 1962 marks the beginning of the history of modern electrochemical biosensors [19]. Clark oxygen detector, an early form of the modern electrochemical sensors, was manufactured by Yellow Spring Instrument Company in 1974 to serve as the first commercial glucose sensor. Today, glucose biosensors, which were initially called "enzyme electrodes", command half of the biosensor market in terms of the number of biosensors produced. Electrochemical sensors depend on the measurement of either the voltage or the current of the electrodes in contact with the analyte. The readout reports on the molecular reactions taking place at the vicinity of the electrodes. Biocatalytic electrochemical sensors are based on the reaction of enzymes, whole cells, or tissue slices with the target analyte. The majority of glucose sensors use glucose oxidase enzyme (GOx), and thus fall into this category. Affinity electrochemical sensors, in contrast, detect the reaction of biofunctional recognition elements such as antibodies and nucleic acids. These sensors can be employed for the specific detection of complex biomolecules using their specific biofunctionalities [20, 21].

In the more recent and modern versions of electrochemical sensors, nanowires, single wall, and multi wall carbon nanotubes (SWCNT and MWCNT), have been used as nano-electrodes to demonstrate LODs of few zetamolars for detecting proteins [22], and ∼10 pM for deoxyribonucleic acids (DNAs) [23]. On the flip side, according to some recent estimates of the binding kinetics at low concentrations for such tiny electrodes, the binding events occur once every few days [10, 24], a major hit to the turn-around time of these nano-electrode sensors. It has also been reported that the addition of bioreceptors on the surface can have a deleterious effect on the performance of semiconductor nanowires [25]. Furthermore, the performance of the device is sensitive to the Debye length of the analyte. In other words, a change in the pH or salt concentration can result in a different readout, for the same concentration of the target biomolecule [26–28].

1.2 Optical Integrated Sensors

The interaction of light with matter is another transduction mechanism upon the principles of which a sensor can be realized. Surface plasmon resonance (SPR) sensors monitor the shift in the resonance at a metal-dielectric interface [29]. The phase matching condition, for the evanescent light at the interface and the surface plasmon polariton (SPP) in the metal, determines the resonance wavelength of the structure. The binding of the biomolecules to the surface changes the real part of SPP propagation constant, and thus results in a resonance shift. Designs based on prisms, gratings, and fibers have been demonstrated for this type of transducer [30]. Commercial SPR systems are capable of reaching LODs of 0.1 pg/mm^2 [31]. For lab-on-chip devices, localized surface plasmon resonance (LSPR) is a more suitable option as the plasmon-polariton is formed in a nanoparticle, which can be excited by the elements of an optical circuit on the chip, in addition to their higher field enhancement that reduces the power consumption [30, 32]. The interest in LSPR sensors increased especially

after the discovery of surface-enhanced Raman scattering (SERS). As compared to SPR sensors, the decay length of the light is about 50 times shorter in LSPR sensors, which gives them a competitive edge over SPR sensors for single-particle spectroscopy and detection [33]. Recent notable works on LSPR sensors include the demonstration of an LOD of $\sim$40 fg/mm^2 for monolayers [34, 35], and detection of individual unbinding events for antibody-antigens [36] and individual molecules [37, 38]

Dielectric on-chip photonic devices have proven to be compact, sensitive transducers. Integrated grating couplers, interrogated by an angle-resolved detection system, can sense deposition of monolayers on their surfaces [39]. Using long-period gratings inscribed by UV light in a photonic crystal fiber, sensitivities of 1.4 nm/nm (resonance shift divided by the thickness of the monolayer) have been demonstrated [40].

On-chip waveguides in interferometric configurations are another category of sensitive devices. For instance, integrated Mach-Zehnder interferometers (MZI) are based on the splitting of light (typically coherent) into two arms; one of which exposed to the analyte, while the other covered with a protective layer [41]. Using 1.8 mm long silicon-on-insulator (SOI) waveguides, MZI sensors have achieved LODs of 0.3 pg/mm^2 [42]. In MZI sensors the light in the two arms are combined on the chip and the intensity of the combined light is detected as a measure of relative phase change. A closely related configuration, Young's interferometer, lets the two beams interfere in the free space to form interferometric fringes recorded by a charge-coupled display (CCD) or a detector array [43, 44]. This sensor has been commercialized [45], and in later improvements, by using 4 mm long arms in silicon nitride (SiN), an LOD of 20 fg/mm^2 [46] has been demonstrated, with the prospect of single-virus detection claimed [46].

In addition to interference, resonance can also provide us with sensitive transducers. Photonic crystals have proven to provide high Q and small mode volumes [47, 48]. High Q and small mode volume help achieve better LODs. Two-dimensional

(2D) photonic crystal sensors with surface detection limits of about 5×10^2 pg/mm^2 have been demonstrated [49]. By designing a photonic crystal with a slot void in the center, sensitivities up to 1500 nm/RIU with a Q of about 5×10^4 have been reported [50]. One-dimensional (1D) photonic crystals, also called nanobeams, fabricated by scalable deep ultra-violet (UV) lithography have recently been reported with a surface sensitivity of $\sim$0.1 nm/nm and a Q of $\sim 10^4$ [51]. Another report by the same group demonstrates the detection of single polystyrene particles with diameters down to 25nm using these resonators [52]. This report (Q=3.5×10^4 in water, at a wavelength of 1550 nm) matches the capabilities previously demonstrated for high-Q microspheres (Q=6.4×10^5) [53], and microtoroids (Q=10^8) [54].

Traveling wave resonators typically have higher Qs compared to photonic crystal structures. Microtoroids with linewidths as narrow as few femtometers in water (corresponding to Qs of $\sim10^8$) are possible to fabricate [54]. The higher the Q, the finer the measurement resolutions, provided that the resonance detection is limited by the amplitude noise on the detected signal. On the other hand, for linear systems, the LOD is determined by the resonance shift divided by the minimum detectable shift (measurement resolution). Since the sensitivity of these ultrahigh-Q devices is typically less than the lower-Q resonators, the improvement of the Q by itself does not guarantee an improved device performance. In fact, in cases where the minimum detectable shift is limited by spectral measurement resolution or thermal noise in the resonator, using a high-Q but otherwise low-sensitivity (in terms of resonance shift) device will result in a degradation of LOD. For example, the resonance shift of the microtoroid in [54] is $\sim$0.5 fm for 25 nm polystyrene beads, where the same shift for the nanobeam resonator in [52] is 170 fm. Considering the fact that the linewidth of the external cavity diode laser used in the former is on the same order as its shift ($\sim$0.1 fm), it has a slim margin before hitting the limit by the laser phase noise. Hence, the considerably higher Q of the microtoroid resonator, compared to the nanobeam

resonator, will not be of much help beyond this point, unless lasers with narrower linewidths are used.

Microring and microdisk resonators are another type of traveling wave resonators. Compared to photonic crystals, they are more tolerant to fabrication imperfections and can offer high Qs [55–57]. Microrings fabricated in polymers and dielectrics have been demonstrated for sensitive gas and biological sensing [58–61]. The CMOS compatible fabrication of dielectric microrings enables high-yield and high-throughput fabrication of large arrays of microring resonators. It is possible for this fabrication to be performed by deep UV lithography or by being taped out to foundries such as IMEC, as some groups in the academia and industry currently do. The relatively large refractive index contrast between the core and the cladding enables the realization of compact devices with dimensions down to a few microns, which helps to reduce the overall footprint of the multiplexed microarrays based on these elements.

1.3 Organization of the Dissertation

This dissertation is presented in three main sections: biosensor platform and multiplexed sensing results, an interferometric method for wavelength noise reduction, and theoretical noise studies. In Chapter 2, the optical theory and modeling of the microring resonators are presented. Important properties of silicon nitride material platform for the realization of a resonance-based integrated photonics resonator are discussed. The design of the microring sensors and their performance characteristics are presented using numerical simulations, and the optimum design is presented.

Chapter 3 includes the details of nano-fabrication, surface chemistry, bio-receptor immobilization, microfluidic packaging, and optical characterization. The problem of waveguide-resonator coupling optimization is investigated and a systematic optimization approach based on the specifics of noise characteristics in the system is presented. The results of multiplexed sensing experiments (for glycan-lectin and

antibody-antigen pairs) and preconcentration experiments are presented and discussed.

In Chapter 4, a statistical analysis of amplitude noise and its effect on the error in resonance detection are introduced. Closed-form relations for the estimation of resonance detection error for two commonly used resonance detection methods (i.e., absolute minimum method, and linear regression method) are derived. A fundamental difference between the two methods and the dependence of their performance on noise characteristics are explained for the case of quantization noise, as an example.

Chapter 5 describes a comprehensive study of the sources of noise in the characterization system. Three major categories of noise: temperature noise, amplitude noise, and wavelength noise are evaluated based on experimental measurements and numerical simulations (Monte Carlo and finite element method), to identify the dominant source noise. I find that the dominant source of the noise is wavelength noise, and introduce an efficient interferometric method based on inverse-function calculation of the wavelength to suppress the wavelength noise, without any need to temperature stabilization or requiring moving parts in the interferometer. Chapter 6 includes some suggestion for the continuation of the work.

CHAPTER II

SILICON NITRIDE MICRORING RESONATORS

2.1 Introduction

In this chapter, the preliminary work on the design of microring resonators is presented. Microring resonators provide a compact, sensitive, and scalable transducer that enable the realization of versatile and highly multiplexed arrays for label-free sensing. The immobilization of biological recognition elements, such as glycans or antibodies, makes the sensor both sensitive and selective to the target analyte of interest. Moreover, the integration of microfluidic channels facilitates the delivery of small volumes of analyte, in addition to helping to cope with the diffusion barrier.

2.2 Microring Resonator Transducers

The resonance wavelength of a microring resonator is dependent on the refractive index of the material surrounding the resonator. Thus, any refractive index changes around the resonator, within the evanescent tail of the resonator mode, result in a resonance shift. Having a higher refractive index than water, the biomolecules at the vicinity of the resonator can be detected by monitoring the resonance shift. For a ring-shaped resonator, the periodic boundary condition, necessary for satisfying the phase matching condition, determines the resonance wavelength (λ_0) as [62]

$$\lambda_0 = \frac{n_{eff}.2\pi R}{m}, \tag{1}$$

where m is azimuthal mode order, R is the average radius of the microring, and n_{eff} is the effective index of the waveguide comprising the resonator. The biomolecules change the effective index of the microring, which results in a shift in the resonance wavelength. Finite element method (FEM) implemented in a COMSOL environment

was used to solve axisymmetric Maxwell equations at the cross section of the microring. The theoretical basics of microring resonators can be found for instance in references [63–66]. The perturbation caused by the biomolecules is related to the resonance shift ($\delta\lambda$) by [67]

$$\delta\lambda = \lambda_0 \frac{\int \Delta\epsilon(\bar{r}).|\bar{E}(\bar{r})|^2 dv}{\int \epsilon(\bar{r}).|\bar{E}(\bar{r})|^2 dv}, \tag{2a}$$

$$\delta\lambda = \lambda_0 \frac{\int 2n\Delta n(\bar{r}).|\bar{E}(\bar{r})|^2 dv}{\int n^2(\bar{r}).|\bar{E}(\bar{r})|^2 dv}, \tag{2b}$$

where λ_0 is the resonance wavelength, $\epsilon(\bar{r})$ is permittivity as a function of location, $\Delta\epsilon(\bar{r})$ is the change in local permittivity, $n(\bar{r})$ is local refractive index, $\Delta n(\bar{r})$ is the change in local refractive index, and $\bar{E}(\bar{r})$ is electric field. Equations (2a) and (2b) are identical for infinitesimally small perturbations. However, both formulas deviate from the actual resonance shift for larger values of $\Delta\epsilon$ (or Δn). As illustrated in Figure (2), the perturbation relation based on refractive index introduces smaller error. This fact is observed for other resonators in our work as well. Thus, where required, refractive index, rather than permittivity, will be used as the perturbation parameter.

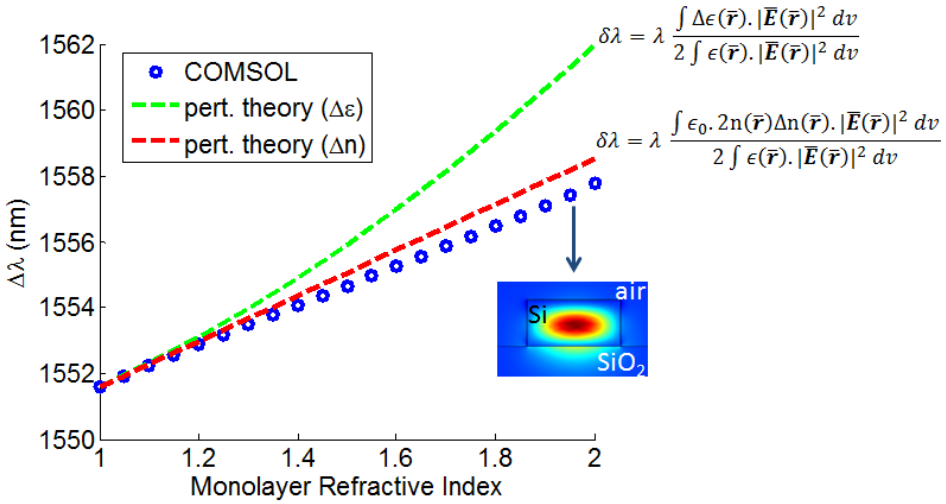

Figure 2: The COMSOL simulation and perturbation theory calculation of the resonance shift for a 5-nm-thick organic monolayer on the top, left, and right surfaces of the resonator. The cross section of a Si resonator on oxide substrate with air cladding is shown in the inset. The inner radius is 10 μm.

The smallest quantity of the target material (for instance quantified by the concentration of a target biomolecules) that can be differentiated from blank (the lack of any target biomolecules at the input), within a confidence interval of about 99%, is defined as the limit of detection (LOD). This figure of merit is conventionally quantified as

$$LOD = \frac{3\sigma}{S}, \tag{3}$$

where σ is the standard deviation of the output without any changes in the input, and S is the sensitivity. The sensitivity is defined as output shift per the unit of the input. The input is typically defined in terms of either the bulk refractive index in cladding, the thickness of the biomolecule layer bound to the surface, the surface density of bound biomolecules, or analyte concentration. Setting the detection limit at the 3σ-level of the system noise (assumed to be Gaussian) ensures that the probability of a false positive (a.k.a. type I or α error) for blank input is less than 0.003. The improvement of sensor performance comes through the enhancement of the sensitivity (S), or by employing more precise measurement techniques to reduce 3σ.

For the sensors relying on resonance shift, the error in resonance detection is assumed to scale with the linewidth of resonance. The rationale is that if the linewidth is scaled by a factor of two (for example), the sampling rate can also be scaled in the same way. Thus, if the integration time per sample is kept the same, the signal-to-noise ratio (SNR) remains as before, while the wavelength axis is scaled by a factor of two. Hence with any arbitrary signal processing method used for resonance detection, the error in resonance detection also scales by the same factor of two. This means that $3\sigma \sim \lambda_0/Q$, and we have

$$LOD \sim \frac{\lambda_0}{Q.S}. \tag{4}$$

This relation provides a basis to compare LOD of different sensors in a unified context. It should be noted that this simple equation does not relate all the details about the advantages and limitations of the sensors. As briefly discussed before, and

demonstrated in the next chapter, the introduction of other sources of noise, such as spectral noise or thermal fluctuations, makes the comparison more delicate.

2.3 Material Platform and Operation Wavelength

The sensor material platform affects critically the sensor performance. Dielectric resonators have been demonstrated in different material platforms including silicon (Si)[68], silicon nitride (SiN)[69, 70], indium phosphide (InP)[71], and polymers[58]. Stoichiometric SiN is an appropriate choice as it is compatible with the majority of surface functionalization protocols that use such chemicals as acetone and piranha. In addition, SiN has a relatively small thermo-optic coefficient (TOC). Despite several temperature compensation techniques proposed for integrated photonic resonators[72, 73], the temperature difference between the sensor and the reference resonators is still a source of device-level thermal noise. Small TOC of SiN results in the suppression of this thermal effect by one order of magnitude compared to Si, InP, gallium arsenide, and titania [74–76]. It is worth mentioning that designing the device to get $\partial n_{eff}/\partial T \simeq 0$, as is the rationale of most athermal designs, does not help in reducing the fundamental thermodynamic noise in the device. I will discuss this noise in detail in Section 5.3.1. As the origin of this noise is not just the fluctuations of the average temperature, athermal designs aimed at zeroing the average do not help. In this sense, SiN or silicon dioxide (SiO2) have an inherent advantage over Si for their smaller TOC.

Furthermore, stoichiometric SiN has two important advantages in terms of system cost. First, it can be deposited using inexpensive processes such as low-pressure chemical vapor deposition (LPCVD). Second, it is transparent to near infrared and visible wavelengths, which enables the use of low-cost Si photodetectors in the system. Si microrings have been used for biosensing at wavelengths around 1550 nm, where Si has a very low loss, and laser sources are widely available. The wavelength window

around 1300 nm is also of interest, for which water absorption is much less than that at 1550 nm, while Si is still transparent to the light. However, Si-based designs basically entail wavelengths that are not absorbed by Si, and thus Si detectors can not be used for the detection of light. This especially becomes an issue if large arrays of microrings are needed for multiplexed detection, for which either the microrings should be interrogated one by one, or an expensive III-IV detector array should be used. In contrast, stoichiometric SiN enables the employment of Si detectors, thus reducing system cost considerably. Furthermore, water absorption at 670 nm (red laser) is 4.7×10^{-3} cm^{-1}, compared to 1.3 cm^{-1} at 1300 nm, and 11.7 cm^{-1} at 1550 nm [77]. Thus, for biosensing applications, visible light is subject to much lower loss compared to infrared (IR). This enables the achievement of higher Qs and better LODs with water cladding. Visible wavelengths are also of interest for sensing as other sensing modalities such as fluorescence sensing can be integrated to the same platform without the need for additional laser sources [78]. Addition of parallel sensing mechanisms will provide extra information that will enhance the specificity and sensitivity of the whole sensing system. SiN microrings have been researched for gas [60] and biological sensing [79] at IR wavelengths. Other variations such as slot microring at $\sim$1300 nm [72, 80], and ultrathin microrings at 790 nm [81] wavelengths, have also been investigated. Furthermore, stoichiometric SiN has two important advantages in terms of system cost. First, it can be deposited using inexpensive processes such as low-pressure chemical vapor deposition (LPCVD). Second, it is transparent to near infrared and visible wavelengths, which enables the use of low-cost Si photodetectors in the system. Si microrings have been used for biosensing at wavelengths around 1550 nm, where Si has a very low loss, and laser sources are widely available. The wavelength window around 1300 nm is also of interest, for which water absorption is much less than that at 1550 nm, while Si is still transparent to the light. However, Si-based designs basically entail wavelengths that are not absorbed

by Si, and thus Si detectors can not be used for the detection of light. This especially becomes an issue if large arrays of microrings are needed for multiplexed detection, for which either the microrings should be interrogated one by one, or an expensive III-IV detector array should be used. In contrast, stoichiometric SiN enables the employment of Si detectors, thus reducing system cost considerably. Furthermore, water absorption at 670 nm (red laser) is 4.7×10^{-3} cm^{-1}, compared to 1.3 cm^{-1} at 1300 nm, and 11.7 cm^{-1} at 1550 nm [77]. Thus, for biosensing applications, visible light is subject to much lower loss compared to infrared (IR). This enables the achievement of higher Qs and better LODs with water cladding (see Equation 4). Visible wavelengths are also of interest for sensing as other sensing modalities such as fluorescence sensing can be integrated to the same platform without the need for additional laser sources [78]. Addition of parallel sensing mechanisms will provide extra information that will enhance the specificity and sensitivity of the whole sensing system. SiN microrings have been researched for gas [60] and biological sensing [79] at IR wavelengths. Other variations such as slot microring at ∼1300 nm [72, 80], and ultrathin microrings at 790 nm [81] wavelengths, have also been investigated.

2.4 Microring Design and Optimization

Numerical simulation is used to design the microring geometry so that the free spectral range (FSR) is about 4 nm, resulting in two azimuthal modes for each resonance within the 8 nm scanning window of our external cavity diode laser. This requires an outer radius of 8 μm. The width of the microring is chosen so that the microring is radially single-mode, desired for a spectrally multiplexed device. In the single-mode range of width, wider microrings will have better Qs, while the sensitivity decreases with the width. These specifications for a SiN microring with water cladding, oxide substrate, a SiN film thickness of 240 nm, an outer radius of 8 μm, and working around $\lambda = 655$ nm are presented in Table 1. The linewidth of the microring for

the range of widths and radii we are concerned with will depend on the quality of fabrication. However, other specifications of the microring are expected to closely match the simulations. The optimization of the sensor at this stage was performed with regard to Q.S as the figure of merit (see Equation 4). According to the sharp drop of Q observed for widths of 400 nm and narrower, and relatively slower variations of S in this range of widths, the highest LODs are expected to be achieved around widths of 500 nm, corresponding to Qs in the range of 3-6$\times 10^4$ in water. This width has been used in the fabrications.

Table 1: The specifications of a single-mode SiN microring versus its width (simulated by COMSOL). The cladding is water, the substrate is SiO2, the outer radius is 8 μm, and the SiN film thickness 240 nm. The surface sensitivity is calculated for an organic monolayer with an index of 1.45. The temperature sensitivity reported here corresponds to material TOC (excluding thermal expansion).

width	FSR (nm)		n_{eff}		$\Delta\lambda/\Delta T$ (pm/°C)		Bulk S. (nm/RIU)		Surface S. (pm/nm)	
(nm)	TE	TM	TE	TM	TE	TM	TE	TM	TE	TM
300	3.95	4.00	1.66	1.64	-3.4	-2.5	70	65	159	137
400	3.97	3.97	1.74	1.68	-0.75	-1.5	40	53	102	119
500	4.05	4.00	1.78	1.71	0.28	-1.1	29	48	75	109
600	4.10	4.01	1.88	1.80	0.79	-0.88	23	45	62	105

In order to compensate for temperature drifts, a subset of the microrings are dedicated to referencing by means of the differential measurement of resonance shift [73, 82]. The reference microring is isolated from the solution by a protective oxide layer. Thus, the differential resonance shift, as the measure of the bound analyte on the surface, is not affected by the common temperature drift in the microrings, or a homogeneous wavelength drift in the laser.

CHAPTER III

MULTIPLEXED LABEL-FREE BIOSENSING

3.1 Introduction

In addition to material platform, which was discussed in the previous chapter, proper sensor design includes the optimization of its geometry. For optimization of LOD in resonance-based sensors, typical design procedures seek to minimize 1/Q.S, where Q is the quality factor of the resonance, and S is its sensitivity[83]. On the other hand, it is a well established design procedure to maximize the signal-to-noise ratio (SNR), with the "signal" typically defined as the extinction of the resonance[84]. However, in optimization cases that require a compromise between the SNR and Q, a unified approach encompassing both these factors simultaneously is missing from the literature. An example of such a compromise is the optimization of waveguide-resonator coupling that simultaneously affects the SNR (through changing the extinction) and loaded Q.

In this chapter, I demonstrate that to achieve optimal LOD, the resonance lineshape curvature at the resonance wavelength is the single important parameter of the lineshape that should be optimized. This parameter includes contributions from both the linewidth and the extinction. The waveguide-resonator gap is then used to tune the coupling strength, which in turn tunes the resonance curvature. A full biosensor based on the optimized elements is fabricated, and functionalized with glycan bioreceptor molecules. Glycans are carbohydrate molecules that specifically recognize toxins and other bio-functional molecules[85]. The solution of target molecules is delivered through a microfluidic flow cell to reduce the response time and minimize the required sample volume[86].

In Section 3.2, I explain device theory, methods, and fabrication. The device is covered with a protective oxide layer to isolate the reference microrings from the test sample, and also to protect the waveguides from physical damages. To pattern the protective oxide layer, I use a swabbing lift-off method to increase lift-off quality compared to oxide lift-off using sonication. The optimization of resonance-waveguide coupling is elaborated in Section 3.3. The objective of this optimization is to minimize detection vulnerability to noise while accommodating the effects of the resonance extinction and the loaded Q. Section 3.4 explains microring surface activation, glycan immobilization, and the fabrication of microfluidic flow cell are also described in this section. The sensor is used for label-free, specific, and multiplexed detection of Aleuria Aurantia Lectin and Sambucus Nigra Lectin in Section 3.5. Specificity to target bio-molecules is achieved by the immobilization of 3FL and 2,6-NA2 glycans on the surface of the microrings. The conclusion is presented in Section 3.8.1.

3.2 Biosensor Platform: Fabrication, Packaging, and Optical System

3.2.1 Photonic Device Fabrication

The sensor array consists of five SiN microring resonators coupled to a common bus waveguide, as shown in Figure 3. The width of the bus waveguide and the microrings is 500 nm to ensure single-mode operation. The outer radius of each microring is about 8 µm. Slight offsets in the radii of the microrings on each waveguide result in spectral offsets on their resonance wavelengths. This offset prevents resonance overlap in the spectral domain. It should be noted that the addition of organic bio-receptor layers also shifts the resonances, depending on the size of the bio-receptor molecules and their surface density. This fact should be taken into account if the resonances are to be designed equidistant in the spectrum.

Device thin film stack is fabricated by thermal oxidation of a standard eight-inch Si wafer to grow 4 µm thermal silicon oxide (SiO_2), followed by the deposition of

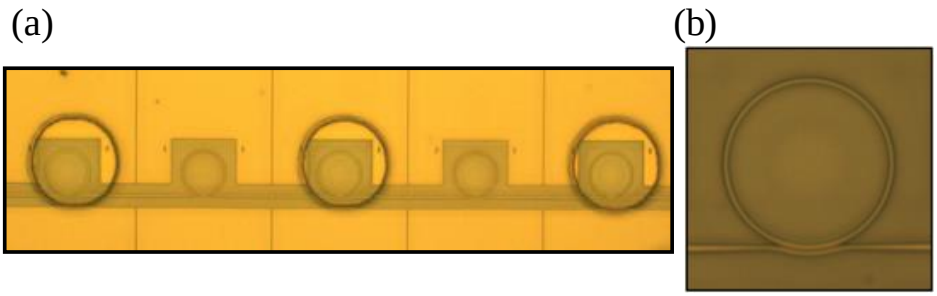

Figure 3: Microscope images of (a) a microring array, and (b) an individual microring. The width of each microring is 500 nm to ensure single-mode operation, and its radius is about 8 µm.

240 nm stoichiometric SiN using low-pressure chemical vapor deposition (LPCVD). Thermal oxidation and SiN deposition are performed by Rogue Valley Microsystems (Medford, OR, USA) The device pattern is written into ZEP520A electron-beam resist (Zeon Corp.) by JEOL JBX-9300FS electron-beam lithography (EBL) system, and transferred into the SiN layer by inductively coupled plasma etching using CF_4 chemistry, leaving no SiN pedestal. Standard ZEP520A spin coat protocol and a dosage of 220 µC/cm^2 is used for the EBL. I use ESPACER 300Z (Showa Denko K.K.; Singapore) in EBL process to prevent excessive charge-up. The resist is rinsed by de-ionized (DI) water for 1 min, developed for 2 min in amyl acetate, and then soaked for 30 s in isopropyl alcohol (IPA). The residual resist after etching is stripped using Microposit remover 1165 (Shipley).

3.2.2 Protective Layer: Oxide Lift-off

Oxide deposition and lift-off are performed to open circular windows above the three sensing microrings on an otherwise oxide-covered chip. To do so, Shipley 1827 resist is spin coated at 500 RPM for 10 s and then 4000 RPM for 60 s, followed by 1 min bake at 150 °C on a hotplate. Photolithography is done using 365 nm UV light with a dosage of 150 mJ/cm^2. Subsequently, the chips are developed in Microposit MF-319 for 50 s with gentle agitation, and then rinsed in DI water. A final one-minute descum in oxygen plasma removes the residual resist. As a result, the three sensing microrings

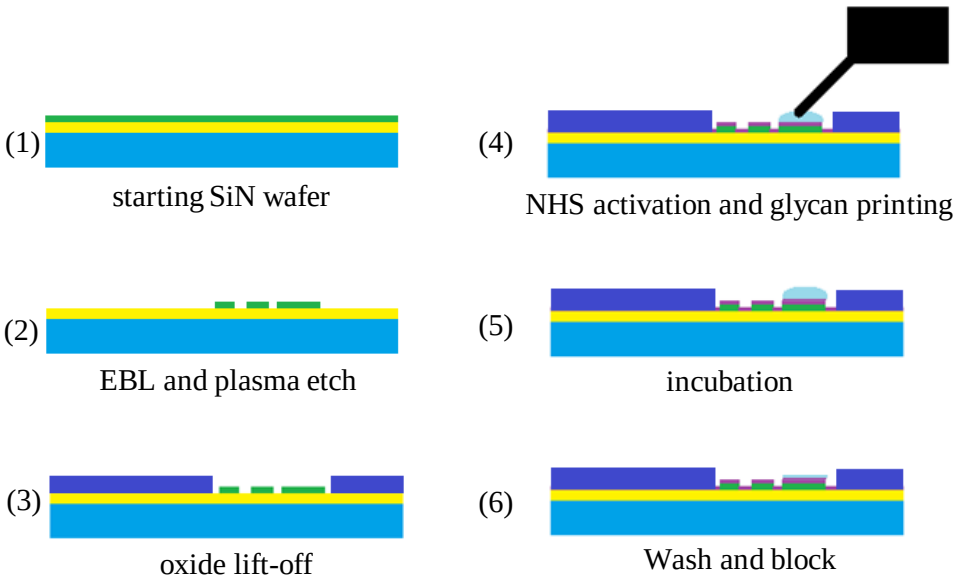

Figure 4: A schematic illustration of major device fabrication steps.

are covered by the Shipley 1827 resist while the rest of the substrate is exposed. Using low-temperature plasma enhanced chemical vapor deposition (PECVD), 2 µm of protective oxide is deposited on the chip at a temperature of 100 °C. Next, the chip is submerged in acetone for 10 min and then gently brushed with an acetone-soaked swab to remove the residue of Shipley 1827 resist and expose the sensing microrings. The chip is finally cleaved to make the waveguides accessible at the edges of the chip for input/output laser coupling. Major fabrication steps are schematically demonstrated in Figure 4.

I found the use of a swab more reliable than ultrasonics bath for oxide lift-off. The force applied by the swab is mainly exerted to the bumps created by the circular patterns of the resist, as opposed to other flat areas. Since the adhesion of low-temperature oxide to the SiN layer is not strong, the ultrasonic agitations can lift the oxide off at undesired areas.

One of the challenges in the EBL on SiN was charge-up. Because of the insulating nature of the ZEP, SiN, and SiO_2 layers, incoming EBL electrons cannot leave the area

easily after hitting the surface. This results in a charge accumulation that deflects the EBL electrons beam. Hence, even with sufficient calibration of the EBL machine position accuracy is severely lost. Figure 5a shows stitching error in the EBL machine, a common cause of which is charge-up. The EBL machine parses the pattern into windows of 500 nm by 500 nm, and the segments of a waveguide that cross the borders of these windows will be exposed at different occasions. Considerable accumulation of charge in between writing these two segments results in beam deflection and a shift between these segments as observed in this figure. To solve this problem, I added a thin film of of Espacer on my samples right before EBL exposure, as explained above.

For less severe charge-up situations, the pattern may not be totally displaced but still the resist can get over-exposed or under-exposed at critical locations. This change in the effective dosage occurs because of EBL beam deflection. After the development of the resist, the under-exposed areas will contain too much residue of the resist, and not-to-be-exposed areas will be partially dissolved in the developer. This process results in an undesirable etch profile. One such example, which was observed when Espacer was not used, is shown in Figure 5c.

After the EBL and development, the sample is etched in a plasma chamber. Figure 5b shows the top surface of ZEP resist after etch. Because of the considerable roughness in the ZEP surface, a relatively thick layer of ZEP is coated on the samples (typically, about 600 nm at the above-mentioned spin speed) to prevent a complete removal of the resist at any points on the SiN device. With a typical etch rate of 40 nm/min, only around half of the ZEP layer is expected to be etched.

Eventually, the sample is cleaved at the edges for light coupling. The cleaving process usually generates debris and particles, an example of which is shown in Figure 5d. For this reason, the cleaving is deferred until the very last step of fabrication when the device has a protective oxide layer. Even if a fraction of the debris do not leave from the surface after thorough cleaning and sonication, the protective oxide

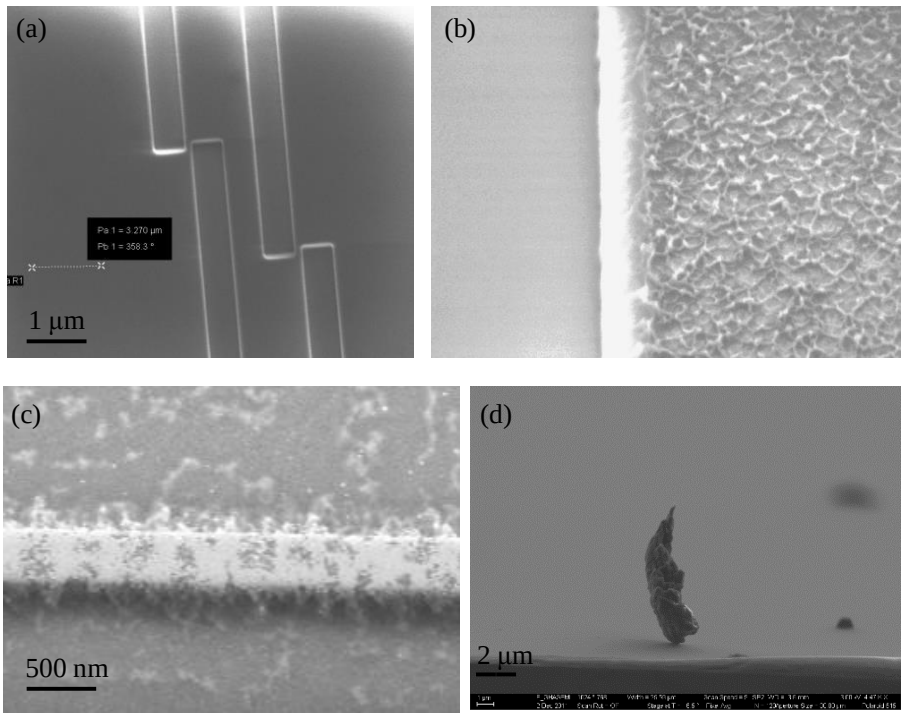

Figure 5: Common fabrication imperfections. (a) Electron beam lithography stitching error, a typical reason of which is charge-up. (b) Uneven etching of ZEP e-beam resist on the top, which necessitates the spin coating of relatively thicker layers of ZEP. (c) A roughly etched SiN waveguide. This is most likely due to severe EBL charge-up that has changes the exposure dosage of the resist. (d) An example of debris and particles sitting on the chip after cleaving that can result in substantial optical loss if they remain on the waveguides or resonators.

layer keeps them few microns away from the waveguides or resonators.

3.2.3 Biosensor Characterization Setup

As shown in Figure 6, the laser light ($652 - 660\,\text{nm}$, Newport TLB 6305) is passed through a half-wave plate, a polarizing beam splitter, and a lens to have the light with transverse magnetic (TM, magnetic field in the device plane) polarization focused at the input facet of the sensor chip. The light exiting the output waveguide is projected onto a photodetector (Thorlabs PDA36A silicon amplified detector) using another long working distance lens. The laser is controlled by a LabVIEW software that scans the wavelength over the $652.4 - 660\,\text{nm}$ window, while the readout of the

photodecetors is synchronously recorded by a USB-6211 National Instrument data acquisition (DAQ) device. The laser scan rate is 1 nm/s and sampling resolution is 0.25 pm. Normalized transmission spectrum is calculated by dividing the transmitted power to baseline power. The baseline power is calculated by low-pass filtering the transmitted power to remove higher frequency features of the spectrum. An in-house data analysis software in MATLAB environment tracks the resonance shifts in time.

3.3 Sensor Optimization: Q versus SNR

3.3.1 Defining the Figure of Merit

Waveguide-resonator coupling determines the extinction and the loaded Q of the resonance. The strength of this coupling depends on the gap between the waveguide and the resonator. Proper choice of this gap helps maximize resonance sharpness. A sharper lineshape helps detect the resonance more accurately at any specific noise level.

An important aspect of the resonance detection procedure is the specific data processing algorithm employed. Our argument here is mainly focused on a quadratic fit to the data around the resonance, as the resonance detection algorithm. A quadratic fit using linear regression[87] is a fast, universal, and versatile method that can rival more sophisticated but sensitive detection methods such as a non-linear parametric fit[72]. Although parametric fits in general are more accurate when we have an accurate parametric model of the lineshape (e.g., Lorentzian function), in practice the uncertainty about the actual resonance function impedes the performance of these parametric fits. The discrepancy between the model and actual lineshape comes from various sources of reflection in the device, such as fabrication imperfections and the edges of circular openings on the waveguides, which result in lineshape deformation. In this condition, a Lorentzian fit does not necessarily lead to a more accurate detection of the resonance. In contrast, for the majority of mechanisms leading to a

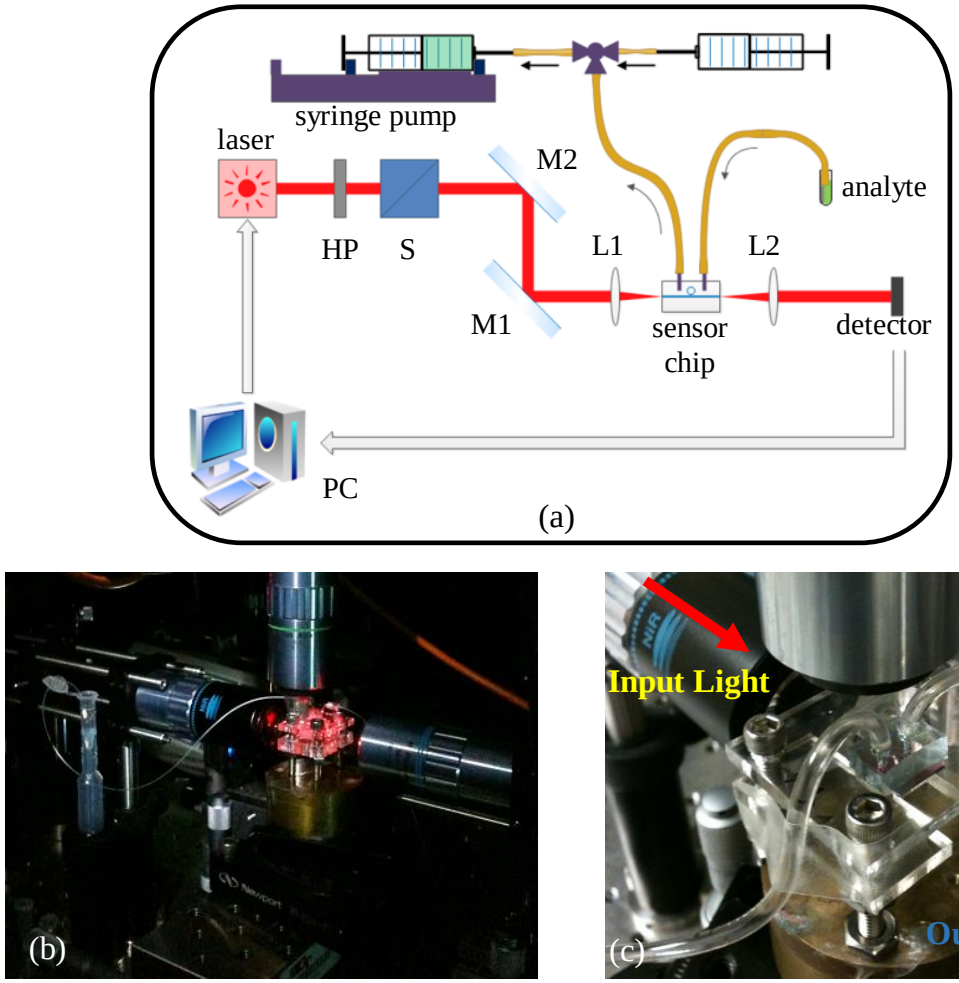

Figure 6: Optical characterization system. (a) The dominant polarization axis of the laser light is rotated by a half-wave plate (HP) to make it parallel to the surface of the sensor chip, and a polarizing beam splitter (S) passes only the TM polarization toward two alignment mirrors (M1 and M2). The TM-polarized light is focused on the input facet of the bus waveguide using a long working distance lens (L1). Using a second lens (L2), the light leaving the chip is projected on a photodetector, the data of which is sampled by a data acquisition card and processed by a personal computer (PC). A syringe pump in negative pressure mode draws the analyte solution into a microfluidic chip and then into a waste syringe. (b) Characterization setup and packaged sensor. (c) A packaged sensor on the characterization setup.

lineshape deformation, the lineshape still follows a general quadratic function around the resonance.

The Lorentzian lineshape of the microring resonances can be approximated by

a quadratic polynomial around its dip. The quadratic polynomial is determined by two parameters: its curvature (κ_0), and the amplitude of its minimum point (i.e., a vertical offset). The latter does not affect the resonance detection accuracy because a homogeneous shift in the amplitudes of all data points does not shift the resonance along the wavelength axis. Thus, as far as detection accuracy is concerned, the only important parameter is the lineshape curvature.

Beside the lineshape curvature, noise level should also be considered in the coupling optimization. If the noise is intensity-independent, the extinction of the resonance does not affect the noise level. However, for an intensity-dependent noise, the extinction determines the noise level around the resonance dip. It is therefore necessary for the optimization procedure to simultaneously minimize the noise level (σ_n) while maximizing the curvature (κ_0). The end goal of this optimization to minimize the error in resonance detection when the measurement contains noise. In this regard, it should be noted that an identical scaling of all measurements (i.e., the lineshape and the noise level) does not change the resonance detection accuracy. Hence, we would like the figure of merit (FOM) not to change under such a scaling. Hence, I define the figure of merit as the ratio of σ_n and κ_0, since both parameters scale identically and the scaling factors is eliminated from their ratio:

$$\text{FOM} = \frac{\sigma_n}{\kappa_0}. \tag{5}$$

Although I introduced the FOM in Equation 5 through a general discussion of its requirements and some hand-waving, a rigorous analysis of my resonance detection method (using quadratic fit) supports this FOM.[87] In the argument presented above I highlighted the general characteristics of this FOM, such as invariance to scaling, beyond the quadratic fit method in specific.

By using the FOM defined in Equation 5, we do not need to optimize the Q or SNR separately. This FOM is the ultimate criteria for optimizing the performance of the sensor in terms of amplitude noise, which is the objective in the optimization of

Q and SNR.

3.3.2 Noise Measurement for Calculation of FOM

To calculate the FOM in Equation 5, I first study the σ_n in the numerator. To measure the intensity dependence of noise in my setup, I replace the sensor chip with a polarizer. The polarizer acts as a variable attenuator since the laser light has a major axis of polarization. At any specific wavelength, the sensor device is a linear system with a determined attenuation (and a phase response that is not picked up by the photodetector). Thus, an attenuator can be used to measure the effective noise on every data point of the spectrum.

For noise measurement, the laser wavelength is scanned from 652.4 to 660 nm with a constant current of 43.5 mA. Photodetector gain is 40 dB. Since laser output power varies slowly over the scan window, the baseline is calculated by applying a 21-point moving average filter to the data in a MATLAB environment. The difference between the raw readout and the baseline is considered as the noise. For each specific attenuation (i.e., polarizer angle), the standard deviation of noise (σ_n) is calculated over the data in $654 - 659$ nm window. The resulting curve in Figure 7 shows the intensity-dependence of noise as

$$\sigma_n(V) = (0.35\,\mathrm{mV}) + (0.3\,\mathrm{mV/V})V, \tag{6}$$

where V is the average light intensity on the photodetector, expressed in terms of the equivalent voltage that the photodetector generates at its output (including the amplification).

In the next step, I address the denominator in Equation 5. The resonance curvature (κ_0) and its extinction can be calculated using coupled-mode theory (CMT). The power transmission through a device with a single microring, $T(\omega)$, is[88, 89]

$$T(\omega) = \frac{P_{out}}{P_{in}} = \left| \frac{-2j(\lambda - \lambda_0)/\lambda_0 + 1/Q_0 - 1/Q_c}{-2j(\lambda - \lambda_0)/\lambda_0 + 1/Q_0 + 1/Q_c} \right|^2. \tag{7}$$

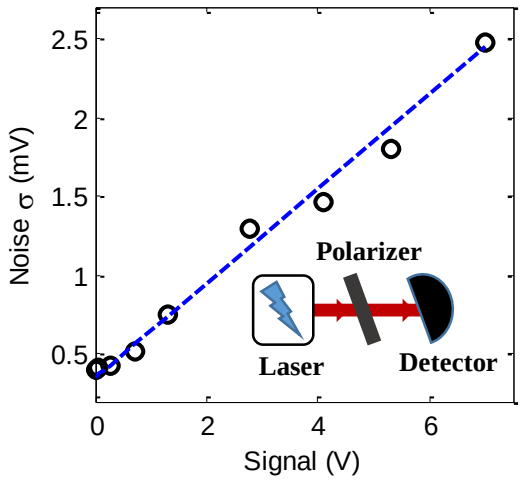

Figure 7: Noise intensity as a function of the average intensity of incoming light on the photodetector. Since the laser output is partially polarized, a polarizer serves as a variable attenuator to control the average intensity of the light on the photodetector.

Here, λ_0 and Q_0 are resonance frequency and intrinsic Q of the microring, respectively. The wavelength is denoted by λ, and the coupling quality factor by Q_c. The curvature of this lineshape at its resonance is

$$\kappa_0 = V_0 \left.\frac{\partial^2 T}{\partial \lambda^2}\right|_{\lambda=\lambda_0} = 32 V_0 \left(\frac{Q_0}{\lambda_0}\right)^2 \frac{(Q_c/Q_0)^3}{(1+Q_c/Q_0)^4}, \tag{8}$$

in which V_0 denotes the photodetector voltage readout for a all-pass transmission.

The FOM can be calculated using the noise characteristics from Equations 6 and 7; and resonance curvature from Equation 8. Assuming a typical all-pass voltage of $V_0 = 1\,\mathrm{V}$ through the device, and arbitrary but constant λ_0 and Q_0, I am to minimize Equation 5:

$$\mathrm{FOM} = \frac{\sigma_n(V_0 T(\lambda_0))}{\kappa_0}. \tag{9}$$

The result is plotted in Figure 8 for different values of coupling factor. Optimum coupling occurs for $Q_c/Q_0 \approx 2.21$, which corresponds to an extinction of about 8.5 dB (undercoupled).

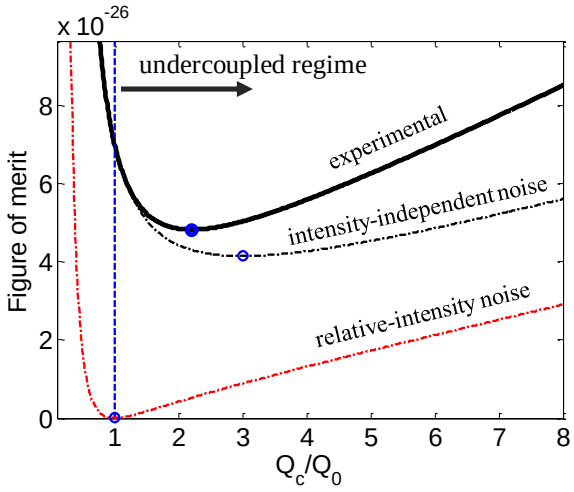

Figure 8: The figure of merit (FOM) defined in Equation 9 for different coupling Qs and noise characteristics. The solid line shows the FOM corresponding to the experimentally measured noise. The two broken lines show the cases for intensity-independent noise ($\sigma_n(V) = 0.35\,\mathrm{mV}$), and relative-intensity noise ($\sigma_n(V) = (0.3\,\mathrm{mV/V})V$). In all the three cases, the FOM is less sensitive to the variations of the coupling Q in the undercoupled regime ($Q_c/Q_0 > 1$). The circles show the minimum FOM in each case.

3.3.3 Discussion on Optimal Coupling

It is a widely invoked optimization rationale to choose sensor parameters that result in maximum light-matter interaction, which occurs at critical coupling regime ($Q_c/Q_0 = 1$) [58]. However, it is seen in Figure 8 that at the critical coupling regime (∞ dB extinction) the figure of merit degrades by 45% compared to its optimum value (i.e., an undercoupled 8.5 dB extinction here). For a quadratic fit, this improvement in the FOM leads to 45% smaller error in resonance detection, with the error defined as three times the standard deviation of the detected resonance ($3\sigma_\lambda$) in the presence of amplitude noise [87]. Note that the limit of detection (LOD) is linearly dependent on the error of resonance detection. Hence, the above mentioned improvement in the error lead to a similar improvement in the LOD.

3.4 Surface Chemistry and Microfluidics

3.4.1 Surface Chemistry

The transducer discussed in the previous section will show a response for every biomolecule entering the evanescent tail of the microring mode, without differentiating among different molecules. Specificity for a biosensor is typically achieved through a variety of methods. Affinity-based sensors rely on the immobilization of receptor molecules that are biologically functional and can capture the target molecules, while let other molecules leave the surface. Some of the bioreceptors such as antibodies are very specific to the target, while other categories such as glycans are less specific but will provide a fingerprint for complex solutions when an array of them is used. Spectrometric methods, on the other hand, probe the biomolecules to measure their mass or optical properties (e.g., Raman signature) to recognize their target.

Index sensing mechanism of the microring resonators allows sensing biomolecules without attaching a fluorophore, radiolabel, or Raman label to them. This label-free sensing scenario simplifies sample preparation steps and results in reduced cost and turn-around time of the whole sensing system. Moreover, labeling can lead to steric hindrance and improper binding to the receptors. Based on these considerations, the development of label-free sensors is of great interest.

Sensor surface chemistry is important as it can contribute negatively to the accuracy of detection. A challenging issue with the choice of bioreceptor and surface chemistry is the non-specific binding of irrelevant molecules to the surface. Such molecules result in an unwanted resonance shift. Another level of non-specific binding occurs when irrelevant molecules bind to the bioreceptors or linkers on the surface through undesirable binding mechanisms. These effects lead to biochemical interference in the functioning of the sensor. On the other hand, binding and unbinding events on the surface of a cell or a microring resonator are stochastic processes. This fact results in stochastic fluctuations in the number of molecules bound to the surface,

even when the system is at its saturation. These fluctuations can be characterized by the Equation (4.15) in the reference [90]:

$$\frac{\delta C_{eq}}{C_{eq}} = \sqrt{\frac{K_D}{LR_T}}, \tag{10}$$

where C_{eq} is the number of ligand/receptor complexes at the equilibrium, δC_{eq} is root-mean-square deviation of C_{eq}, K_D is the dissociation constant, L is the concentration of target molecules, and R_T is the total number of surface receptors. At low concentration of target molecules, these fluctuations do not disturb LOD calculations, since the measurement system noise is dominant. Maximum uncertainty occurs for $L = K_D$ at which $\delta C_{eq}/C_{eq} = 1/\sqrt{R_T}$. For a typical receptor surface density of 10^{12}cm^{-2}, the number of receptors on a typical microring resonator used in our platform[1] is $R_T \sim 10^6$. This number amounts to an uncertainty of 0.1%. For example, if the resonance shift of a saturated surface for a specific type of target molecule is 100 pm, the noise originating from stochastic binding fluctuations is about 0.05 pm, occurring fora half-saturated surface.

For the sensor discussed here, the bioreceptors are covalently bound to the surface of SiN microring. The bioreceptors either already have, or they are derivatized to include, an amino functional group (-NH2). Amine groups covalently bind to carboxyl functional groups (-COOH) to form a peptide bond (-C(=O)NH-). This is the same type of bond that holds together the chains of amino acids that comprise proteins and DNA. The absorption wavelength of peptide bond is around 190-230 nm [91], far enough from the working wavelength of the biosensor. Thus if the surface is prepared with carboxyl groups, bioreceptors will firmly bind to it. For this preparation, I activate -OH bonds on the surface using oxidizing solutions like Piranha or oxygen plasma. Subsequently, one or two crosslinking steps are performed that result in availability of NHS esters on the surface that enable incoming amino groups to react

[1] radius of 8 µm, height of 240 nm, width of 500 nm

with the carboxyl groups. I have tested and optimized two surface chemistry protocols for this purpose outlined below.

The first method, depicted in Figure (9), uses a homobifunctional linker containing two NHS esters at the two ends. The chips are cleaned in Piranha (5:1 H_2SO_4 and H_2O_2) for 10 minutes and then rinsed with DI water. They are dehydrated for 10 minutes on a hot plate at 100 °C. After cooling, they are put in 5% (3-aminopropyl)-triethoxysilane (APTES) in anhydrous ethanol for one hour. The chips are thoroughly rinsed with anhydrous ethanol and dried with nitrogen stream. The APTES film is cured at 100°C for 20 minutes, to stabilize the siloxane bonds and reduce their hydrolysis rate in aqueous solutions [92, 93]. Silanized chips are then placed in a Petri dish and their surfaces are covered with drops of 1% w/v BS(PEG)9 in anhydrous dimethyl sulfoxide (DMSO, from Acros Organics; Pittsburgh, PA, USA). High concentration of this homobifunctional crosslinker is necessary to ensure high competition between crosslinker molecules and having majority of them attached only at one end to the surface. The Petri dish, sealed with Parafilm, is left undisturbed at room temperature for 5 hours. Afterward, the NHS-functionalized surfaces are washed in anhydrous ethanol thoroughly and dried by nitrogen stream. The poly(ethylene glycol) spacer arm in BS(PEG)9 crosslinker decreases non-specific binding of any molecules attaching to the surface with binding mechanisms other than the specific glycan-lectin binding. The spacer arm is 3.6 nm, which is much shorter than the 90 nm penetration depth of the TM mode into the water clad.

The use of a homobifunctional group in the first method caused low corsslinking efficiency from time to time. As the crosslinker has similar functional group at both ends, it was possible for the linker to attach to the surface at both ends. Especially the PEG chain gives the linker extra flexibility facilitating this event. To prevent this event, high concentration of the crosslinker can be used to produce a strong competition among the crosslinker molecules in attaching to the surface, and thus minimizing

the fraction of the crosslinkers which are attached at both ends. This method, however, imposes a restriction on the concentration that restricts the control on density of the crosslinker on the surface. Proper optimization of the surface chemistry depends on specific bioreceptor and the target biomolecule. The surface is desired to be capable of capturing maximum number of molecules. On the other hand, overcrowding the surface with crosslinkers results in straight PEG chains which inhibits proper functioning of this chain in reducing non-specific binding. Furthermore, the spatial flexibility of the linker+bioreceptor reduces steric hindrance and decreases the odds that a bioreceptor is blocked by neighboring bioreceptor from capturing the target. Hence, I developed a second surface chemistry protocol based on a heterobifunctional crosslinker, which is explained below.

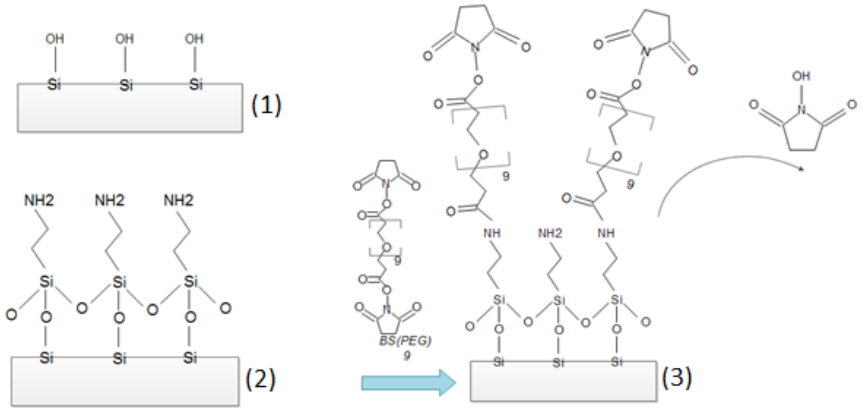

Figure 9: The surface chemistry protocol for NHS activation on the surface based on the homobifunctional crosslinker BS(PEG)9.

In the second method, the -OH bonds of the surface are activated by cleaning it with piranha (5:1 mix of H_2SO_4 and H_2O_2) for 30 min, a DI water rinse, and a 10 min exposure to UV/ozone plasma in a UVOCS cleaner. The chips are then immersed in a 2% v/v solution of (3-mercaptopropyl)trimethoxysilane in anhydrous toluene for one hour (in nitrogen ambient), thoroughly rinsed with IPA, dried, and baked at 80 °C for 20 min. When the samples cool down, a drop of 2 mM SM(PEG)12 linker (Pierce; Chicago, IL, USA) in anhydrous dimethyl sulfoxide (DMSO, from Acros

Organics; Pittsburgh, PA, USA) is placed on the chip to cover its surface. The sample is left unperturbed in nitrogen ambient for about 12 h, and then thoroughly rinsed with IPA. SM(PEG)12 linker contains a polyethylene glycol (PEG) chain that helps reduce the non-specific binding of undesired molecules to the surface[59]. At this stage, carboxyl functional groups containing N-Hydroxysuccinimide (NHS) esters are covalently grafted on the surface and can immobilize any molecules containing amine functional groups. Figure 10a shows a schematic representation of the NHS activation protocol. All chemicals, except SM(PEG)12 and DMSO, were obtained from Sigma-Aldrich (St. Louis, MO, US).

A 200 mM solution of amine-derivatized glycan[94] is printed selectively on the microrings using a BioForce Nano eNabler. Using this tool, each microring can be coated with a specific glycan. Prior to the printing, the specific glycan solution is mixed 1:1 with phosphate buffered saline (PBS, pH 7.4) containing 10% glycerol to impede evaporation of the glycan solution in the open-top reservoir of the printing cantilever. After the glycans are printed, the chip is left at a relative humidity of 80% to prevent evaporation of the printed droplets. This allows the glycan molecules to bind to the surface through their amine functional groups. Next, the sample is incubated in a high humidity (at about saturation) chamber at 50 °C for 1 h. The chips are dried and thoroughly washed in a PBS solution with 0.05% Tween 20, and then in DI water. Remaining NHS esters are de-activated in a solution of 50 mM ethanolamine in 0.1 M Tris buffer (pH 9.0) for 1 h. This finalizes the glycan immobilization step and prepares the chip for microfluidic integration.

To verify the efficacy and specificity of the activated surface, I tested the binding of the glycans using fluorescence microscopy. GM1 glycan[95] was immobilized using the above mentioned method on SiN surface, and a 50 µg/ml drop of biotin conjugated Cholera toxin B subunit (CTB from Sigma Aldrich; St. Louis, MO, US) was placed on the surface for 1 h. The SiN surface was then thoroughly washed with

PBS solution containing 0.05% Tween 20, and then by DI water. Subsequently, a 200 µg/ml drop of Alexa 488 conjugated Streptavidin (Life Technologies; Carlsbad, CA, USA) was placed on the surface for 1 h, followed by same wash process mentioned above. Figure 10b shows an image of the surface using a Carl-Zeiss LSM 710 confocal fluorescence microscope. The bright spots in this figure correspond to the areas where the glycans have been printed. In these areas, the glycans capture biotin-CTB, and then biotin-CTB captures Alexa-Streptavidin. In other areas, biotin-CTB and thus Alexa-Streptavidin can not effectively bind to teh PEG-coated surface. The image shows a high contrast between glycan-coated areas and the rest of the surface, which demonstrates a low non-specific binding on the areas lacking any glycan receptors.

3.4.2 Microfluidic Integration

After immobilization of the bioreceptors, test solution can be applied to the sensor using a reservoir (static mode), or by means of microfluidic channels (flowing mode). As the binding can be mass-transport limited, having the test fluid in flow helps to reducing response time of the sensor. The integration of microfluidic channels allows for sample preparation (e.g., preconcentration [96]) on the chip. One of the methods for realizing microfluidic channels is patterning a hard and resistant material (such as CYTOP) to form microfluidic channels walls and then capping the chip before flowing the analyte in the device. Alternatively, the microfluidic channels can be cast using polydimethylsiloxane (PDMS) and then integrated to the chip using SU-8 glues or by clamps that hold the chip and PDMS microfluidic channels together by applying a small force. In this work I used an SU-8 2050 mold for casting PDMS microfluidic channels and a custom-made Plexiglas holder to keep the sensor chip and microfluidic channels together.

After glycan immobilization, a polydimethylsiloxane (PDMS) microfluidic flow cell is aligned to the SiN sensor chip using Finetech flip-chip bonder. The microfluidic

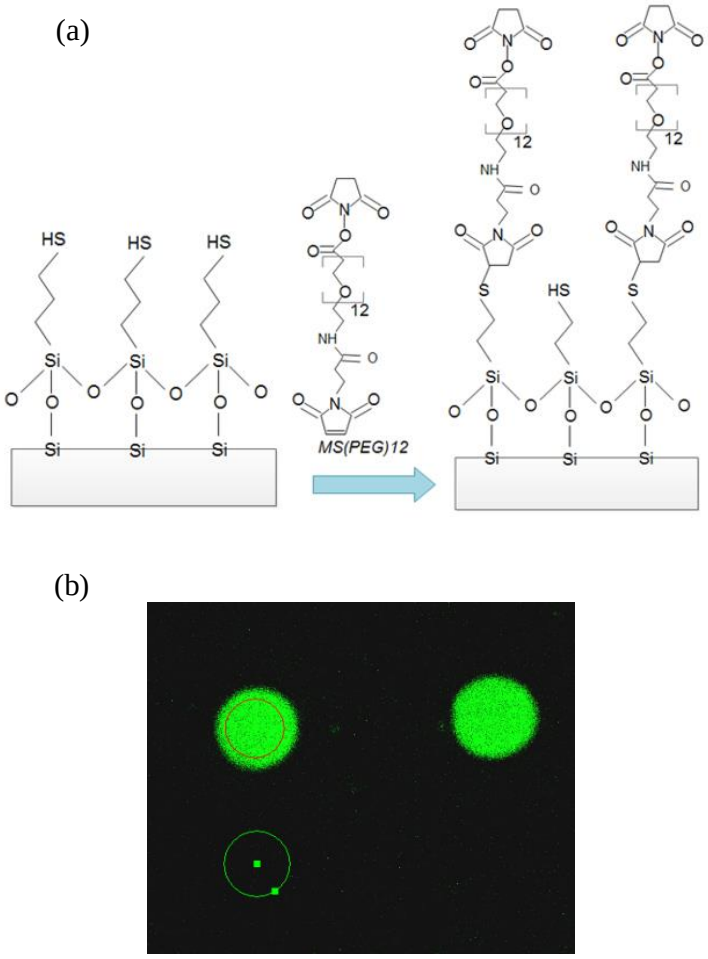

Figure 10: (a) A schematic representation of the heterobifunctional surface chemistry for NHS activation on SiN surface. (b) A fluorescence image showing selective binding of CTB to GM1 glycan with negligible binding to the areas lacking GM1 (but having a PEG brush). The average fluorescence signal intensity is about two orders of magnitude larger in the areas containing GM1 receptors than otherwise.

flow cell helps reduce the response time of the sensor by overcoming the diffusion barrier. As illustrated in Figure 11, two acrylic plates hold the chip and the flow cell together by applying a gentle force exerted by four cap screws and nuts at the corners. A syringe pump in negative pressure mode draws the analyte, with a flow rate of 2 µL/min, into the input tube, the microfluidic chip, and finally the output tube. The microfluidic channel is 100 µm wide and 50 µm high, and it is cast using an SU-8 mold.

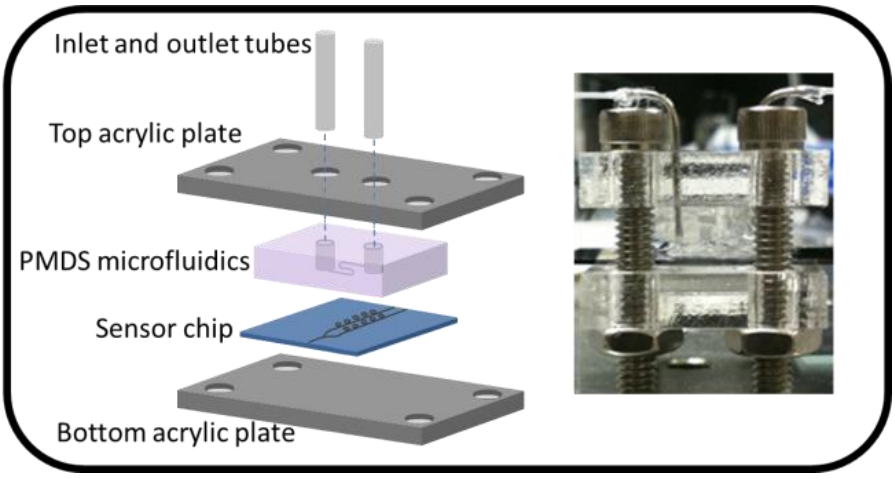

Figure 11: The PDMS flow cell and fluidic holder structure. Two acrylic plates, cut into proper dimensions using a Hermes lasercutter, hold the SiN sensor chip and PDMS flow cell together. Four cap screws and nuts at the corners apply a gentle force to seal the PDMS/chip interface. Inlet and outlet needles are inserted into the holes already made by a puncher in the PDMS flow cell.

To make the mold, SU-8 2050 (MicroChem; Newton, MA, USA) is spin coated on a Si wafer (500 RPM for 10 s, then 2000 RPM for 60 s), and baked at 95 °C for 5 min. The pattern of the microfluidic channel is written into the resist using a Microtech LW405 laserwriter. The sample is then baked, first at 65 °C for 1 min, and then at 95 °C for 4 min. Unexposed resist is removed by 6 min development in SU-8 developer (MicroChem; Newton, MA, USA). The sample is rinsed and cleansed with acetone and IPA, and further baked at 250 °C for 30 min. This finalizes the preparation of the mold.

To cast PDMS, Dow Corning Sylgard 184 PDMS base and curing agent (Ellsworth; Loganville, GA, USA) are mixed 10:1 w/w, stirred well, and degassed in vacuum for about one hour. The mixture is poured into the mold, degassed in vacuum for about one hour, and baked at 90 °C for about 10 hours to produce the PDMS microfluidic flow cell.

3.5 Results

3.5.1 Saltwater Titration

I performed an initial round of fabrication with varying waveguide-resonator gaps to find the gap resulting in an undercoupled 8.5 dB extinction. Figure 12 shows a spectrum scan for devices fabricated with a nominal gap of 100 nm in the device EBL pattern. I conducted saltwater titration to measure the bulk sensitivity of the resonators. Bulk sensitivity is defined as the resonance shift normalized to the refractive index change in the cladding material. I used finite element method (COMSOL environment), with a refractive index of 2.05 for SiN, 1.44 for SiO_2, and 1.33 for water clad, which resulted in a bulk sensitivity of 48.1 nm/RIU (RIU is the refractive index unit of the clad). For experimental measurement of this figure, I tested the sensor with different concentrations of saltwater and measured the resonance shift for each concentration eight times. Having the refractive index of saltwater [97] for different concentrations at 25 °C, the slope of the resonance shift versus refractive index gives the bulk sensitivity. Figure 13 shows the average resonance shift of the three exposed resonators, referenced to the average shift of the two protected resonators. This referencing helps compensate the temperature variations and homogeneous laser wavelength drifts from one scan to the next. The experimental bulk sensitivity is 49 nm/RIU. The difference between the simulation and the experiment is due to fabrication imperfections resulting in small changes in the dimensions and angles of the resonators.

3.5.2 Lectin Detection: Individual Tests

I immobilized amine-derivatized [94] 3-fucosyl lactose (3FL) on two of the exposed microrings for specific detection of biotinylated Aleuria Aurantia Lectin (AAL). All the glycans and lectins in this work were purchased from Vector Labs (Burlingame, CA, USA). The glycan solution was not printed on the middle microring to serve as

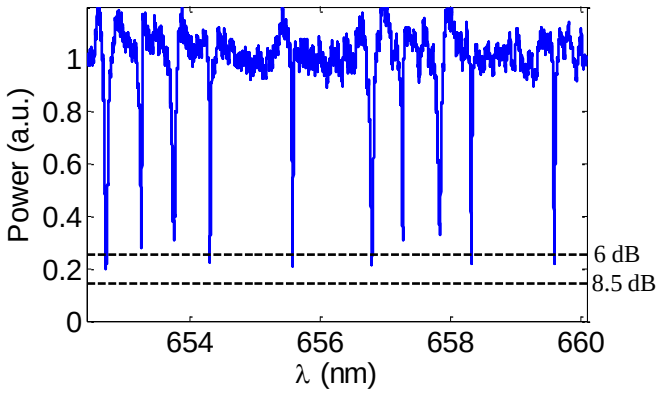

Figure 12: An exemplary spectral scan of the sensor with water cladding. Each microring is radially single-mode, but two azimuthal orders of same mode are present in the scan window. Typical Qs for sensing microrings with water or oxide cladding is 3×10^4.

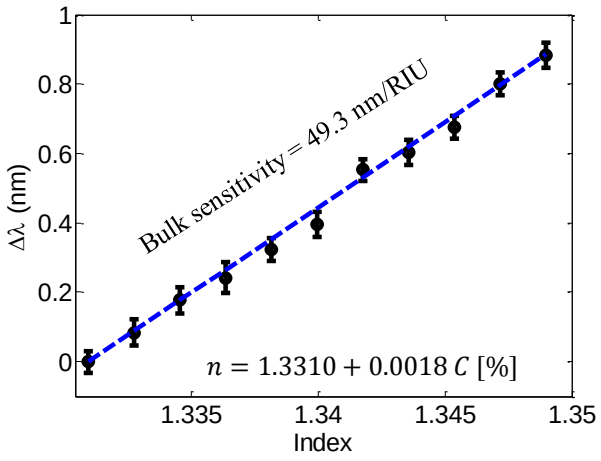

Figure 13: The saltwater titration of the fabricated microrings. Each measurement is repeated eight times. The slope of the fitted line is the bulk sensitivity. Error bars indicate the standard deviation of the repeated measurements.

a control microring. Packaged sensor was fed with different concentrations of AAL and the device spectrum was measured every 10 s. The introduction of each solution, as shown in Figure 14a, results in a red shift in the resonance wavelength of the two glycan coated microrings. The response of the middle microring sensor (lacking any glycan receptors but having a PEG coating) slowly shifts negatively. This shift can be due to non-covalently bound linker molecules that gradually leave the surface when the analyte flows in the channel. The dose-response curve for this glycan/lectin pair

is shown in Figure 14b. The dose-response curve is expected to follow a Sigmoid curve:

$$R = R_s \frac{C}{C + K_D}, \tag{11}$$

where R is the resonance shift corresponding to the concentration C; R_s is the resonance shift for saturated surface (i.e., all binding sites occupied); and K_D is the dissociation constant for the glycan/lectin pair. The average dissociation constant is $K_D = 6 \pm 2\,\mu g/ml$. After the completion of the test the chip was dyed with the protocol described in Section 3.4.1. The inset of Figure 14b shows the fluorescence image of the dyed chip, which shows the binding of Streptavidin molecules only to the microrings with immobilized glycan/lectin molecules.

Similarly, I tested the biosensor with α2,6-disialylated biantennary N-glycan (2,6-NA2) as the bio-receptor, for detecting biotinylated Sambucus Nigra Lectin (SNA). Figure 15 shows the resonance shifts. By fitting the Sigmoid curve to the resonance shifts for three highest concentrations, the dissociation constant is $K_D = 27 \pm 15\,\mu g/ml$.

3.5.3 Multiplexed Lectin Detection

For a multiplexed experiment, I coated the first microring with 3FL, and the last microring with 2,6-NA2 glycan. Each of these glycans are specific to their respective lectins [85], and I process the data from each resonator independently (a theoretical model of multiplexed sensing with cross-binding is discussed in Appendix B). Two mixtures of lectins were prepared: a low concentration solution consisting of 5.4 µg/ml AAL and 10.7 µg/ml SNA; and a high concentration solution consisting of 42.8 µg/ml AAL and 85.6 µg/ml SNA. The low concentration solution was fed for about 15 min to the sensor, followed by the high concentration solution for the same period of time. The sensor response is demonstrated in Figure 16.

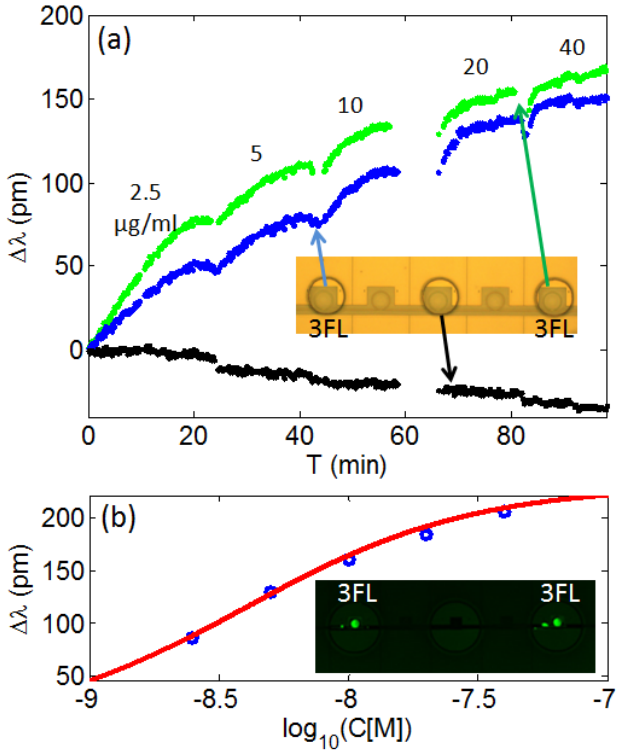

Figure 14: The binding of AAL to 3FL on the surface of the microrings. (a) The resonance shifts of the three sensing microrings, referenced to the average of the resonance shifts of the two oxide-covered microrings. The concentration of AAL in each cycle is noted on the graph in μg/ml. (b) The dose-response curve and fluorescence image of the sensor chip. To compensate the contribution of non-specific binding, the average shifts from the two glycan coated resonators are referenced to that of the PEG coated resonator.

I use the data from the high concentration solution for calibration purpose to calculate the saturated resonance shift (R_s) in Equation 11. This calibration is necessary since the efficiency of the immobilization of the glycans changes from one round of surface chemistry to the next, which alters the number of glycan binding sites. Subsequently, the concentrations of the low concentration cycle (C_L) can be estimated by rearranging Equation 11 to

$$C_L = K_D \frac{R_L}{R_s - R_L}, \tag{12}$$

where R_L is the steady state resonance shift for the low concentration cycle, calculated using an exponential fit to the data. I denote similar parameter for high concentration

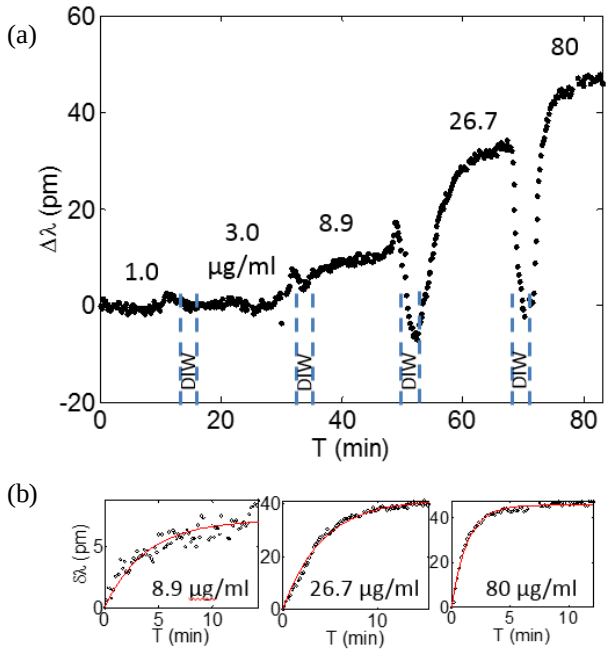

Figure 15: The binding of SNA to 2,6-NA2 on the surface of the microrings. (a) The average of resonance shifts of the two 2,6-NA2 coated microrings is referenced to the resonance shift of PEG coated microring. Different concentrations of SNA (noted on the graph in μg/ml) are fed to the sensor sequentially. (b) The resonance shifts for three last phases of the test for concentrations 8.9, 26.7, and 80 μg/ml.

cycle by R_H. The resonance shifts and calculations are presented in Table 2.

Table 2: Calculated concentrations from the multiplexed test. R_H and R_L are steady state shifts for high and low concentration phases in Figure 16, respectively. R_s is the saturated response. C_L is the estimated concentration of low concentration phase from the multiplexed measurement.

	R_H(pm)	R_s(pm)	R_L(pm)	C_L(μg/ml)
AAL	969	1104	385	3.2
SNA	167	219	81	16

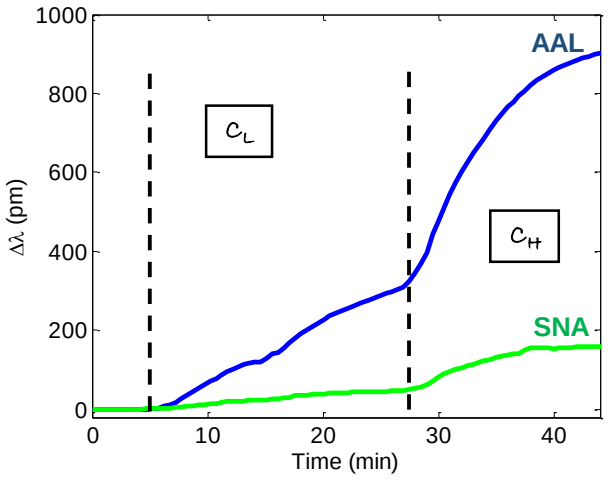

Figure 16: Sensor response to the mixture of the two lectins. The low concentration solution is fed to the sensor in the C_L phase, followed by feeding the high concentration solution in the C_H phase. The resonance shift and saturation time constant for each microring depends on the concentration of the corresponding lectin and the binding dynamics of the glycan/lectin pair.

3.6 Discussions

3.6.1 Limit of Detection

With a repeatability of $3\sigma \sim 0.1\,\text{pm}$ for the resonance detection in our system [98], and a sensitivity of 49 nm/RIU from Section 3.5.1, the sensor LOD is 2×10^{-6} RIU for bulk refractive index sensing. The sensitivity of the microrings to the deposition of an organic monolayer with a refractive index of 1.45 in water is about 109 pm/nm (resonance shift per homogeneous layer thickness, from COMSOL simulations). This leads to a minimum resolvable thickness of 1 pm that corresponds to an LOD of $1\,\text{pg/mm}^2$, which is in the same range as comparable integrated photonic sensor systems based on Si microrings [99], folded cavities [100], and LCORR [101].

For the detection of lectins, the sensor LOD depends linearly on the saturated response, and thus on the density of immobilized receptors on the surface. According to Equation 12, the smallest concentration corresponding to a minimum resonance

shift of $3\sigma_\lambda$ is

$$LOD \approx K_D \frac{3\sigma_\lambda}{R_s}. \tag{13}$$

Hence, according to the saturated resonance shifts (R_s) in Table 2, the LOD is about 0.5 ng/ml (or 7 pM) for AAL detection, and about 12 ng/ml (or 86 pM) for SNA detection. The molecular weights of AAL and SNA are 72 kDa and 140 kDa, respectively. In the calculation of this LOD only the effects of optical, electrical, and thermal noises are included. The $\sim$ µg/ml differences between the calculated C_L concentrations in Table 2 and the actual concentrations, are most likely due to the variations in the surface chemistry, and the non-uniformity of flow originating from air bubbles in the flow cell. I did not carry out a systematic study on the variations originated from the surface chemistry or the analyte flow uniformity.

3.6.2 Coupling Optimization: Special Cases

I optimized the waveguide-resonator coupling in Section 3.3 for the specific noise measured in the setup, and I also focused on quadratic fit as the method of resonance detection. In this section, I discuss alternative possibilities for noise model and for resonance detection method. First, I elaborate on the optimal coupling for two common noise models: 1. intensity-independent noise, and 2. relative-intensity noise. Figure 8 in Section 3.3.2 includes the plots of FOM for these noise models. In this figure, it is worth noticing that for an intensity-independent noise a 6 dB undercoupled condition ($Q_c/Q_0 = 3$) leads to the optimal FOM. Since the noise is independent of the intensity in this case, our optimization approach seeks the coupling condition that produces sharpest resonance. Although at critical coupling the extinction is maximum, the loaded linewidth is wider than undercoupled case. According to our optimization procedure, the 6 dB undercoupled condition is the ideal compromise between extinction and the linewidth. For this coupling point, the figure of merit is 40% larger than that for the critically-coupled case, which results in 40% improvement in

the LOD. For a relative-intensity noise, on the other hand, the optimal condition is critical coupling. In this case, the noise vanishes around the resonance wavelength of a critically-coupled resonator. That is because the output light intensity vanishes at the resonance, and so does the relative-intensity noise by its definition. Hence, the critical coupling regime results in a nearly zero noise level around the resonance and an optimal detection condition.

Next, I discuss the case of using an alternative method of resonance detection, that is defining the resonance as the wavelength at which the light transmission, including noise, is minimum (a.k.a absolute minimum method). The absolute minimum method is a fast and common detection method [84], although it is less accurate than the quadratic fit in general. Nonetheless, rigorous analysis shows that the same FOM proposed in Equation 5 results in the optimal coupling for absolute minimum method as well. The LOD scales as $\sim \sqrt{\text{FOM}}$ when the absolute minimum method is used; while it scales as $\sim$ FOM for the quadratic fit method [87].

3.6.3 Bioreceptor Density on Sensor Surface

I used BioForce Nano eNabler tool to print 3FL glycan first, and then 2,6-NA2, as explained in Section 3.4.1. The printing process requires a high humidity (a relative humidity of about 80% in our case) for the analyte to flow from the reservoir to the surface. This high humidity deactivates water-sensitive NHS functional groups. Therefore, the later a glycan solution is printed, the fewer NHS groups will be available for covalent capture of the glycan molecules. This process results in a relatively lower level of response for SNA compared to AAL in Figure 16. This trend was observed in other similarly prepared sensor chips as well.

For mass manufacturing, it is necessary to calibrate the sensor to compensate the variations in the density of immobilized bioreceptors. This calibration can be performed by dedicating few samples in each batch for the calibration purpose. For

a more accurate detection, each sensor can be fed with a high (known) concentration of the analyte after the actual test to measure the saturated shift of those specific resonators. This measurement determines the number of binding sites for each sensor and reduces the uncertainty originating from surface chemistry variations.

3.7 Preconcentration

Affinity sensors rely on the binding of target molecule to the bioreceptor for the detection. In doing so, the binding dynamics of target molecules and bioreceptors directly affects the LOD of the sensing system or sensing instrument. A key parameter that affects the instrument LOD is the dissociation constant (K_D) of the bioreceptor and target molecule. At lower concentration, the fraction of bioreceptors capturing a target molecule decreases, and this decrease is quantified by a Sigmoid dose-response curve (see Equation12). Then, the overall LOD of the system (or *instrument* LOD) is the multiplication of two factors: dissociation constant, and instrument-noise LOD. To further improve the LOD, however, the sample can also be processed or *prepared* before being fed to the sensing instrument. One such sample preparation is the preconcentration of the sample using microfluidic devices [102]. The contributions of sample preparation, binding dynamics, and instrument detection accuracy will then define the method detection limit (MDL) as the overall LOD of the sensing method used.

Ion concentration polarization (ICP) mechanism has been demonstrated for preconcentration of negatively charged particles [103]. An ion selective membrane is used in this method to create a depletion region from where the positive charges of the sample are evacuated, leaving behind the negatively charged molecules. This region acts as a barrier for incoming negatively charged particles and leads to their accumulation behind the barrier region.

Nafion is an ion selective membrane through which only positive ions can pass

[102]. Having two adjacent channels connected by a thin Nafion layer to each other, positive charges can be transferred across the Nafion bridge by applying a constant voltage. This Nafion bridge helps form a depletion region wherein negatively charged molecules accumulate and form a barrier. This barrier can be employed in a batch-type [102] or a continuous-flow [103] configuration. In a batch-type configuration, the molecules accumulate behind the barrier up to a point where the diffusion balances the blocking effect. In a continuous-flow configuration, the main channel is bifurcated to two channels: blocking channel containing the barrier, and open channel which will contain the redirected charged molecules. A continuous-flow preconcentrator provides better control over the preconcentration ratio, which is an advantage for a biosensor system. The preconcentration ratio is almost equal to the flow rates inside the two bifurcated channels, and this flow rate can be controlled by designing the hydrodynamic resistance of the two channels.

The design of the preconcentrator is shown in Figures 17a. Nafion (Sigma Aldrich; St. Louis, MO, USA) was first printed on a standard glass slide using a specific PDMS microfluidic chip (shown by green in Figures 17b). The sample is left for an hour for the Nafion to be dried. As Nafion is incompatible with solvents such as Acetone or DMSO, it should be printed after bioreceptor immobilization. With bioreceptors already immobilized baking of the Nafion is not possible. As a result, I let the Nafion dry in room ambient rather than baking it. After the Nafion bridge is dried, the preconcentrator PDMS chip is aligned to the Nafion bridge (see Figure 17c) and the structure is fixed using plexiglass holders cut for this microfluidic chip. Figure 17d shows a packaged device on a fluorescence microscope stage. The voltage is applied by the wires connected to the inlet needles.

Prior to testing the preconcentrator chip with target molecules, the channels of the device are treated with phosphate buffer saline (PBS, pH 7.4) containing 0.05% Tween 20 for about 10 minutes to reduce non-specific binding of Streptavidin to

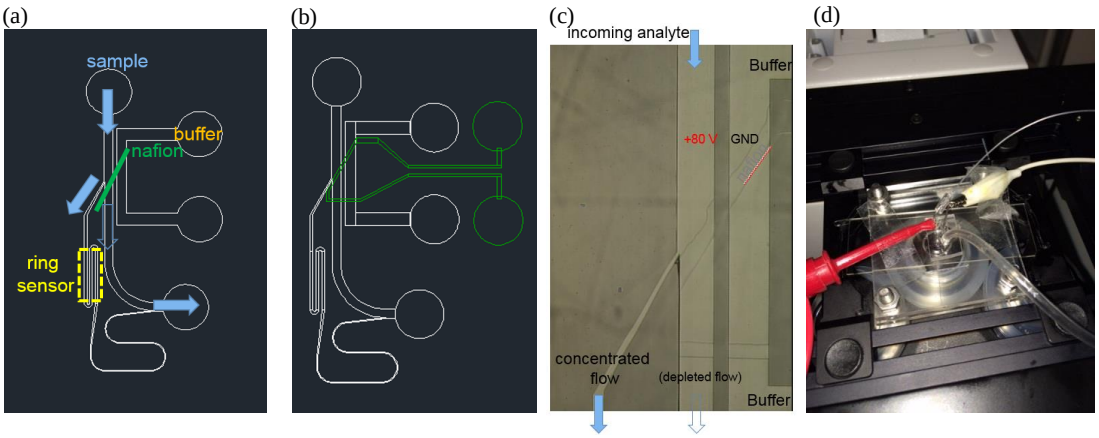

Figure 17: Continuous-flow preconcentrator microfluidic chip. (a) Preconcentrator design showing the position of Nafion layer and flow directions. (b) The green pattern shows the Nafion printing microrlfuidic design, used for printing the Nafion bridge before integrating the main preconcenator microfluidics (white). (c) A microscope image of the PDMS preconcentrator device showing the voltages and flow directions. (d) A picture of the packaged device under tests on a fluorescence microscope.

PDMS channel, Nafion, and glass. The buffer channel is filled with 100X diluted PBS. Then, A solution of $2\,\mathrm{ng\,mL^{-1}}$ Streptavidin tagged with Alexa 488 (Life Technologies; Carlsbad, CA, USA) in 100X diluted PBS was injected into the device with a flow rate of $1\,\mu\mathrm{L\,min^{-1}}$. After about 10 minutes of continuous flow, the voltage applied to the inlets is increased every few minutes in steps of about 5 V, while the preconcentrator chip is monitored under a fluorescence microscope in real time.

The experiment revealed an unexpected result for Streptavidin under working conditions of the experiment. Streptavidin molecules were observed to demonstrate sever aggregation for voltages around 30 V and above. Figure 18a shows a fluorescence image of the chip at preconcentration junction before applying any voltage. The fluorescence signal is uniform across the main channel, while the buffer (lacking Streptavidin) channel is dark. As I increased the voltage gradually to 10 V, an accumulation of Streptavidin on Nafion is observed (Figure18b), which is normal since the barrier consists of accumulated Streptavidin molecules. For higher voltages however, Streptavidin starts to aggregate before an adequate depletion region has a chance to

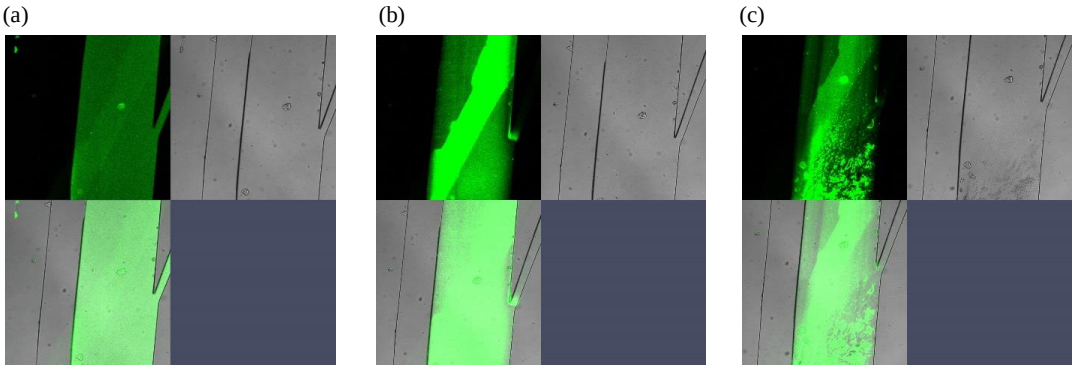

Figure 18: An experimental test of the continuous-flow preconcentrator microfluidic chip. (a) Before applying voltage. Top left panel shows the fluorescence image (green fluorescence color is an arbitrary color coding), top right is a white light image of the junction, and bottom left panel is the two images overlaid. (b) Few seconds after applying a voltage of 10 V. (c) Few seconds after applying a voltage of 25 V. The aggregation of Streptavidin molecules is observed in both fluorescence and white light images.

form (Figure18c). This aggregation was consistently observed in multiple tests with different combinations of buffer dilution and Streptavidin concentration. Light brown layers of the aggregated molecules are observable with naked eye on the glass slide after disassembling the PDMS chip.

The aggregation effect makes this preconcentration technique unsuitable for Streptavidin molecule in specific. In general, aggregation problem can turn out to be detrimental in highly multiplexed sensors that are meant to work with mixtures of many proteins such as unknown water samples or blood plasma. If the aggregation occurs for one molecule type in the solution, deposited layers can potentially shut down the preconcentration mechanism. This concern, requires further preparation steps to effectively filter and capture unfavorable molecules before the sample is fed to the preconcentrator.

3.8 Point-of-care cardiac biomarker detection

The sensor platform discussed here fits the bill for many applications, including point-of-care (e.g., bed-side) or at-home blood analysis. One important application is monitoring the blood biomarkers that indicate a heart attack. Biomarkers like Troponin and BNP are routinely checked in hospitals and emergency room for the diagnosis of a heart attack. Extending such a capability to patients' homes can save thousands lives[2]. I tested the sensor for the detection of Troponin by coating the microrings with the antibodies of Troponin (Fitzgerald, U.S.). Figure 19a shows the response of the sensor for different concentrations of the Troponin fed to the sensor. Estimated LOD from this curve is about 0.1 ng/ml (without interferometry), which is close to the golden threshold of 0.04 ng/ml. This test indicates the potential of this technology for clinical and at-home monitoring of this biomarker. The design of a prototype of a handheld reader and a disposable cartridge including a microring sensor chip is shown in Figure 19b. The same platform can be also used for screening other blood biomarkers such as cancer biomarkers in the blood.

3.8.1 Multiplexed Sensing Summary

Total system cost is one of the commercialization challenges for highly multiplexed biosensors based on integrated photonic resonators. In this chapter a label-free optofluidic sensor was presented that benefits from low-cost SiN device layer, and Si photodetectors. Common design rules of thumb recommend maximum light-matter interaction, which occurs at critical coupling for traveling-wave resonators. However, I showed that while the critical coupling condition is optimum in the presence of a relative-intensity noise, the optimum design in the presence of an intensity-independent noise is an undercoupled resonator with 6 dB extinction. The details

[2]In the U.S., half of the heart-related mortality is caused by a delayed action on the initial symptoms of a heart failure. Only in the U.S., this amounts to about 300,000 lives annually.

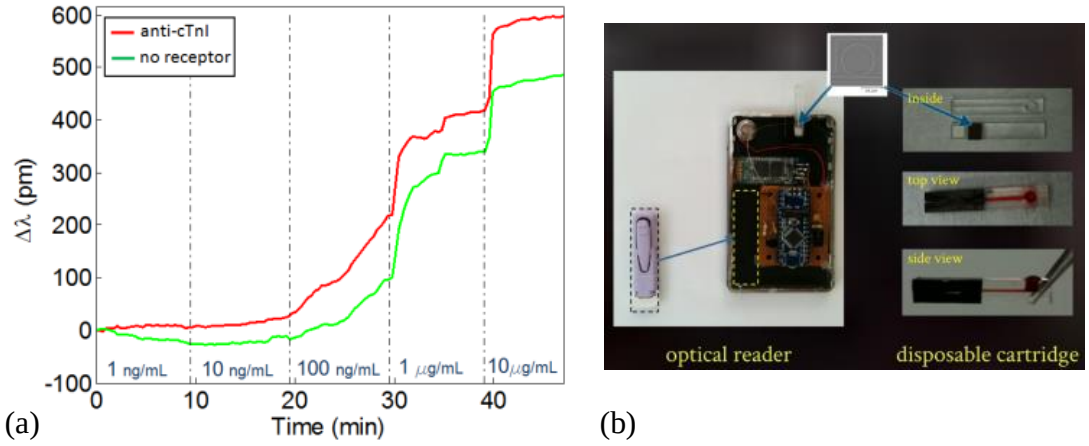

Figure 19: Troponin detection using Troponin antibody on SiN microrings. (a) The resonance shifts of antibody-coated and PEG-coated microrings, referenced to under-oxide microrings. The concentration of Troponin solution diluted in PBS buffer in mentioned on the graph for each phase of the test. The data is collected using the setup shown in Figure 6. (b) An initial prototype of a handheld sensor being designed to work with disposable cartridges that carry the microring sensor chip. The cartridge has a microfluidic channel to draw in the sample using capillary action only.

of fabrication, surface chemistry, and microfluidic packaging of the sensor were explained. Oxide lift-off was performed using swabbing, rather than sonicating, to enhance lift-off quality. Multiplexed label-free detection experiment was performed for Aleuria Aurantia Lectin (AAL) and Sambucus Nigra Lectin (SNA). 3FL and 2,6-NA2 glycans were used as specific bio-receptors for the detection of the lectins. Further analysis shows that the sensor limit of detection is $\sim 2 \times 10^{-6}$ RIU for bulk refractive index, $\sim 1\,\mathrm{pg/mm^2}$ for surface-adsorbed mass, and $\sim 10\,\mathrm{pM}$ for the glycan/lectin pairs studied here. This platform provides a viable solution for the challenges in the scalability of integrated photonic biosensors.

CHAPTER IV

AMPLITUDE NOISE ANALYSIS

4.1 Introduction

Resonance-based sensors are capable of detecting minute amounts of material, even down to individual molecules [36, 104, 105]. To achieve its full potentials, the sensor has to be adequately optimized. This optimization has two facets: highest sensitivity and least vulnerability to system noises. The evaluation of the effect of noise on resonance detection requires efficient numerical and analytical tools to determine how each type of noise affects the accuracy of the resonance detection.

The random error in resonance detection results from various system noises. This error can be quantified in terms of the standard deviation of the detected resonance. I refer to this standard deviation as *the error* (in resonance detection.) The error caused by amplitude noise is not linearly dependent on noise level in general. Electronic, shot, or thermal noise in the system are examples of amplitude noise in resonance spectrum measurements. The aggregate effect of these noises can be represented by an effective random noise on the measured samples [106, 107]. Basically, the components of the aggregate noise fall into two general components of light intensity-dependent and light intensity-independent noises [108]. For small noise levels, the noise level can be assumed almost constant around the resonance, although its dependence on the intensity should be considered in the calculations. The relations for estimating the error from amplitude noise are especially important as they help estimate the power consumption of the sensor. That is becuase the higher the amplitude noise, the higher the required signal power to achieve a target level of error. The target level of error is determined by the limit of detection (LOD) or the false-positive rate that we desire

the sensor to achieve [98].

A widely used method for resonance detection is to scan the spectrum point by point, and then to retrieve the resonance by spectral data analysis. The spectrum measurement approach is especially of interest for spectrally multiplexed sensors (consisting of multiple resonators) in which tracking the resonators one by one is costly and complicated. To analyze the measured spectral data, a variety of processing algorithms have been proposed including parametric fits [109], polynomial fits [110, 111], parametric regression [112], centroid method [113, 114], and optimal linear data analysis [115, 116]. The resulting error in each of these algorithms has an idiosyncratic behavior. Having a closed-form formula for this unique behavior obviates the need for extensive Monte Carlo simulations.

Monte Carlo method is an effective tool to estimate the error originating from system noises [117]. However, a blind Monte Carlo simulation in a multi-dimensional optimization space is time-consuming, and it does not provide the designer with an insight on system trends. Curve fitting to Monte Carlo simulation data has been used to propose ad hoc formula for the error when the resonance of a Lorentzian lineshape is detected subject to a white Gaussian noise [84]. Such a formula for the error not only depends on the lineshape and noise statistics, but also on the specifics of the measurement technique and the resonance detection algorithm. Analytical relations have also been proposed for the estimation of the error on a case-by-case basis. For example Nenninger et al. [118] studied the noise in surface-plasmon-resonance sensors and provided an analytical framework, which can be used along with computer simulations to estimate the effect of noise. Piliarik and Homola [29] proposed a closed-form relation for the error in the centroid data processing method. However, similar relations for other commonly used processing methods are lacking in the literature.

In this chapter, I derive closed-form relations for the error in the two most commonly used resonance detection methods:

1. *absolute minimum* method, which defines the resonance wavelength as the wavelength for which the detector has recorded the minimum (or maximum) readout [84],

2. *linear regression* method, which finds the resonance using a quadratic fit to the data. The majority of the lineshapes of practical interest are quadratic around their resonance, and thus a quadratic fit is usually adequate [119].

A mentionable characteristic of these two methods is their relatively low computational load. I use a simple additive model for noise, which is sufficiently comprehensive for the majority of practical cases [108, 120].

My analysis clarifies the effect of sampling resolution on the error in the above mentioned methods. The ensuing formulas accommodate a large class of noise statistics and resonance lineshapes. Empirical data on the statistics of the aggregate amplitude noise in a conventional laser-scanning setup is presented in Section 4.3. In Section 4.3.1, a theoretical framework based on extreme value theory is developed to propose a parametric formula for the error in the absolute minimum method. In Section 4.3.2, a closed-form relation is derived for the error when the resonance is detected by the linear regression method. For both methods, the proposed formulas are compared against Monte Carlo simulations. Next, I discuss the fundamental difference between the trends of the absolute minimum method and the linear regression method in Section 4.4. The implications of these trends in the presence of quantization noise are also elaborated. Final conclusions are made in Section 4.5.

4.2 False-positive and false-negative rates

The error rate of a two-state sensor (p_E) can be presented in a general form as [121]:

$$p_E = p(NM)p(M|NM) + p(M)p(NM|M), \tag{14}$$

in which $p(M)$ is the probability of having target molecules present in the test solution, $p(M|NM)$ is the conditional probability of the detection of molecules by the sensor while there are no molecules present, $p(NM)$ is the probability of lacking any target molecules present in the test solution, and $p(NM|M)$ is the conditional probability of the sensor not detecting any molecules while there are target molecules present. Two important factors for the evaluation of the performance of a sensor are the false-positive ($p(M|NM)$) and false-negative ($p(NM|M)$) rates. False-positive rate is dependent on the threshold for resonance shifts above which we consider the sensor as detecting target molecules. If repeated measurements of resonance shift has a Gaussian distribution with a standard deviation of σ_λ, a false-positive rate of 0.1% requires a detection threshold that is about $3\sigma_\lambda$ above zero. For any arbitrary detection threshold, the corresponding false-positive rate can be calculated from the cumulative distribution function of a Gaussian distribution (or the real distribution function of the detected resonance otherwise). It should be noted that the false-positive rate depends on all types of noise and interference in the sensing system. In this chapter, I will focus on the amplitude noise and how it affects the standard deviation of the detected resonance shift.

4.3 Experimental Noise Measurement

Laser-scanning setups are common configurations to scan the spectrum of photonic resonators and detect their resonances. Figure 20a shows the scanning electron micrograph (SEM) of a microring resonator coupled to a waveguide in a nitride-on-oxide material platform. Figure 20b shows the transmitted power of the structure shown

in Figure 20a as a function of wavelength (λ) measured using a laser-scanning setup. (The details of fabrication and characterization are explained in Reference [98], and they are not repeated here for brevity.) Figure 20c shows an enlarged view of the recorded spectrum samples along with a Lorentzian fit and a quadratic fit obtained by the linear regression method. Within this wavelength window, these methods result in closely similar fits. Figure 3d shows the detected resonance according to the absolute minimum method and the linear regression method. The difference between the two methods is visible.

I used the laser-scanning setup mentioned above to measure the amplitude noise statistics. The light from a tunable laser (Newport TLB 6305, $652-660\,\mathrm{nm}$, operated at a constant current of $43.5\,\mathrm{mA}$) is passed through a polarizer and then detected by a photodetector (without passing through the integrated device). The photodetector gain is $40\,\mathrm{dB}$, and its analog output is connected to a data acquisition device (National Instrument USB-6211) that samples the (detected voltage) signal and sends the digital readout to a computer. The setup is controlled by a LabView software to synchronously scan the laser wavelength and record the photodetector readout. Laser scan rate is $6\,\mathrm{nm/s}$; and the spectrum sampling resolution is $250\,\mathrm{fm}$. The setup is run at its normal measurement condition (i.e., scanning from 652 to $660\,\mathrm{nm}$) for a fixed polarizer angle. Since the laser output is partially polarized, the polarizer acts as a simple attenuator.

Noise analysis is carried out on the data in the $654-659\,\mathrm{nm}$ window to exclude the power oscillations occasionally observed at the beginning or at the end of the scan window. Since laser output power slowly varies over the scan window, the baseline of the readout is calculated by applying a 100-point moving average filter to the data. The difference between the raw readout and its baseline is regarded as the amplitude noise. This noise excludes lower frequency components such as optical Fabry-Perot oscillations (from the optical components such as the glass/air interfaces

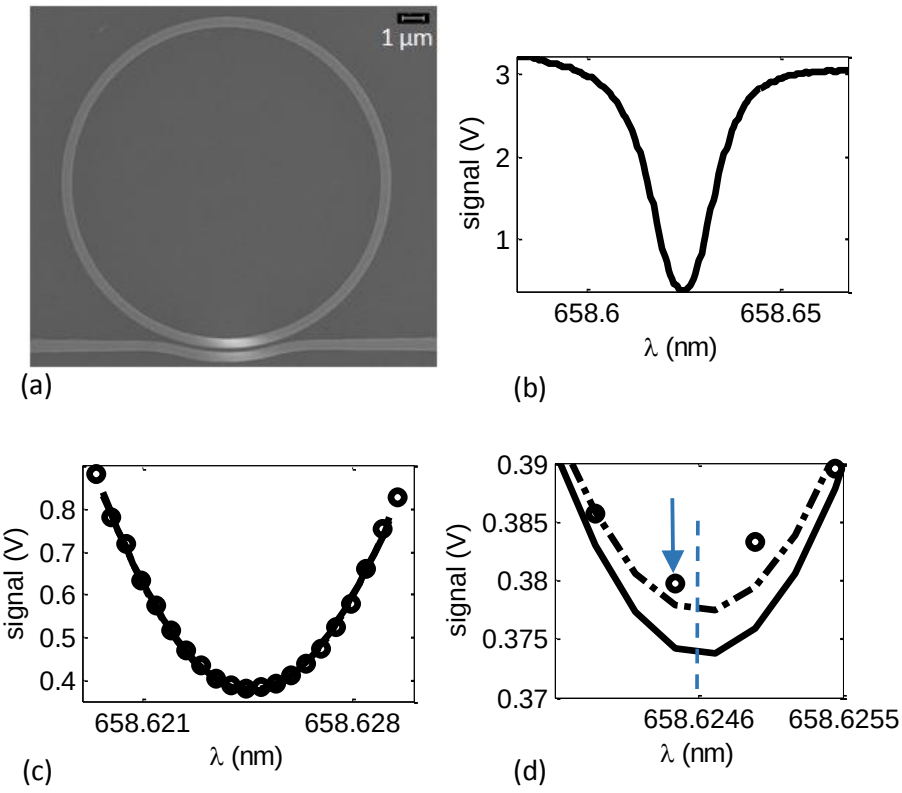

Figure 20: An SiN microring resonator and its resonance lineshape. (a) An SEM of an SiN microring resonator coupled to a bus waveguide. The widths of the microring and bus waveguide are 500 nm to ensure single-mode operation, and the radius of the microring is about 8 µm. (b) Measured resonance lineshape. (c) An enlarged view of the measured data points (circles), a Lorentzian fit (solid line), and a second order polynomial fit using linear regression (dash-dotted line). The Lorentzian and quadratic fits almost overlap in this figure. (d) Further enlargement showing the resonance wavelength as determined by the absolute-minimum method (arrow) and the linear regression method (dashed line).

of the polarizer) and the harmonics of the power grid frequency. Since the behavior and characteristics of such noises are known, they can be removed from transmission measurements using parametric fitting or filtering. Although the recorded samples correspond to different wavelengths of the laser, I assume the amplitude noise not to depend strongly on the wavelength. Figures 21a,b show the noise, extracted as explained above, and its probability distribution function (p.d.f). In this scan, average light intensity on the detector is 68 mV.

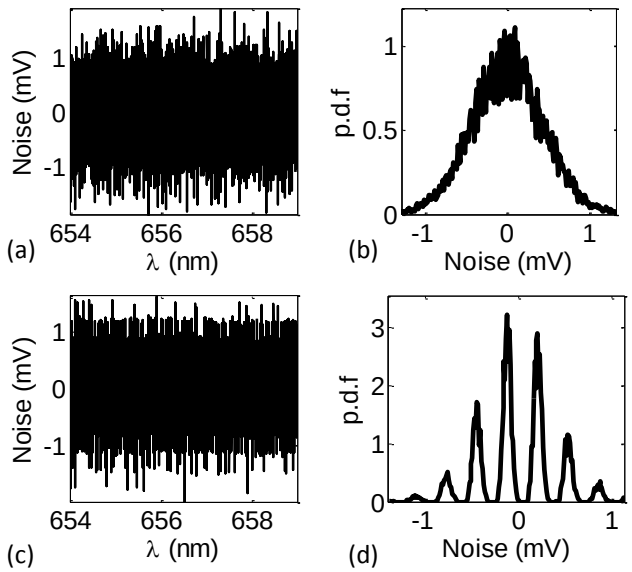

Figure 21: Noise measurement and the calculation of its p.d.f. Photodetector samples are uniformly measured in time as the laser wavelength is scanned. (a) The noise after removing the baseline of the readout. The average light intensity measured by the photodetector is 68 mV. (b) Calculated p.d.f of the noise shown in (a). (c) The photodetector readout (i.e., noise) with the laser light physically blocked. (d) Noise p.d.f after removing the baseline from the readout shown in panel (c). The presence of multiple peaks is due to a quantization noise.

Next, I repeated this experiment with the laser light physically blocked. The photodetector readout is shown in Figure 21c, which demonstrates the quantized values of the readout. The quantization leads to a multi-peak p.d.f, shown in Figure 21d. Since the same setup is also used for spectral measurements of photonic resonators, Figure 21d essentially represents the amplitude noise of the setup on a near-zero resonance dip. The measurements presented here will inform my discussion in Section 4.5.

4.3.1 Absolute minimum method for error estimation

In the absolute minimum method, the resonance wavelength (λ_{res}) is defined as $\lambda_{res} = \lambda_i$, where $i = \text{argmin}\{D_i\}$, and D_i is i-th detector readout. The wavelength of the i-th data point is $\lambda_i = i\ \delta$, where δ is the sampling resolution in the wavelength domain. Based on the Monte Carlo simulations for a Lorentzian resonance lineshape with unity height (amplitude extinction) and subject to a white Gaussian noise, White and Fan

[84] have proposed the following relation for the estimation of the error when absolute minimum method is used:

$$\sigma_\lambda \approx \frac{1}{4.5}\Lambda\sqrt{\sigma_n}, \tag{15}$$

where σ_λ is the standard deviation of resonance wavelength detection, Λ is the full width at half maximum of the Lorentzian lineshape, and σ_n is the standard deviation of the white Gaussian noise. Using extreme value theory in Appendix A, I have shown that the $\Lambda\sqrt{\sigma_n}$ trend in Equation 15 is in fact the dominant term of the Taylor series expansion of the error (σ_λ). It is worth mentioning that the argument in Appendix A holds for a general quadratic lineshape (i.e., non-zero second order coefficient in its Taylor expansion around the resonance wavelength). Thus, the $\Lambda\sqrt{\sigma_n}$ trend can be generalized to other quadratic lineshapes such as Fano. However, the scaling factor depends on the noise p.d.f and the sampling resolution. Following Equation A.13, I let this scaling factor to be a function of δ/Λ and denote it by α_1 to give the error as:

$$\sigma_\lambda(\Lambda, \sigma_n, \delta) = \Lambda\sqrt{\sigma_n}\ \alpha_1(\frac{\delta}{\Lambda}). \tag{16}$$

The analysis in Appendix A provides us with a parametric model in Equation A.19, which is based on the asymptotic trend of α_1. To verify that model, I used Monte Carlo simulations to calculate $\alpha_1(\delta/\Lambda)$ for three separate cases with a) Gaussian, b) uniform, and c) Laplacian noises. Noise standard deviation is assumed $\sigma_n = 0.01$ in all the cases, and the lineshape is Lorentzian as defined in Equation A.5 with $\Lambda = 1$. After adding the random noise to the lineshape, the resonance is detected by the absolute minimum method, and this test is repeated 10^4 times. The standard deviation of the resulting resonances is σ_λ from which we can calculate $\alpha_1 = \sigma_\lambda/\Lambda\sqrt{\sigma_n}$. Finally, the parametric model of Equation A.19 is fitted to the numerical data for $\alpha_1(\delta/\Lambda)$ to estimate optimal parameters. The results are shown in Table 3.

Even though suggested parametric relations are derived from the asymptotic behavior of $\alpha_1(\delta/\Lambda)$, the parametrization allows for the extension of these relations to non-asymptotic regimes of δ/Λ. As demonstrated in Figure 22, the parametric models fit very well to the numerical data over a large range of sampling resolutions. The data point that corresponds to the estimate provided by Equation 15, i.e. Gaussian noise and $\alpha_1 = 1/4.5$, is marked by an arrow on Figure 22. This figure clearly shows that for a fixed Lorentzian linewidth (Λ) and noise standard deviation (σ_n), the error (σ_λ) changes considerably depending on the noise p.d.f and the sampling resolution (δ).

Table 3: The parametric estimates of α_1 for Gaussian, uniform, and Laplacian noise p.d.fs. See Appendix A for the definitions.

	Gaussian	uniform	Laplacian
$p_n(n)$	$\frac{1}{\sigma_n\sqrt{2\pi}}e^{-\frac{n^2}{2\sigma_n^2}}$	$\begin{cases} \frac{1}{c} & \lvert n\rvert < c/2 \\ 0 & \text{otherwise,} \end{cases}$	$\frac{1}{\sigma_n\sqrt{2}}e^{-\sqrt{2}\frac{\lvert n\rvert}{\sigma_n}}$
a_m	$\sqrt{2\ln m}$	m	constant
$\alpha_1(\delta/\Lambda)$	$\frac{A}{\sqrt[4]{\ln(B\Lambda/\delta)}}$	$A\left(\frac{\delta}{\Lambda}\right)^{(1+\epsilon)/2}$	A
A	0.320	0.764	-0.297
B	0.166	-	-
ϵ	-	-0.412	-

Next, I explain how this result can be extended to other lineshapes. First, note

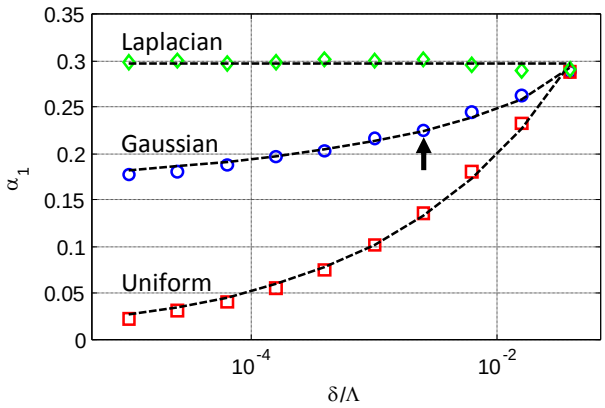

Figure 22: The scaling factor α_1 in Equation 16 for various amplitude noise p.d.fs (Gaussian: circles, uniform: squares, Laplacian: diamonds). The standard deviation of the error (σ_λ) is obtained by Monte Carlo simulations, from which $\alpha_1 = \sigma_\lambda/(\Lambda\sqrt{\sigma_n})$ is calculated. For each noise p.d.f, the corresponding parametric model presented in Table 3 is fitted to the numerical results to find optimal A and B coefficients.

that in Appendix A I replaced the real resonance lineshape with a quadratic approximation early on in the argument. Hence, the $\sigma_\Lambda \sim \Lambda$ behavior is expected to be true for any general lineshape with a quadratic form around its resonance. But to extend the results beyond a Lorentzian lineshape, we need a general definition for the linewidth. According to Appendix A, if the functional variation of the resonance lineshape with wavelength (λ) is given by $R(\lambda)$, the parameter Λ is in fact related to the second order derivative of $R(\lambda)$ at the resonance wavelength as:

$$\frac{\partial^2 R}{\partial \lambda^2}|_{\lambda_{res}} = \frac{8}{\Lambda^2}. \tag{17}$$

Thus, Λ can be defined more rigorously as:

$$\Lambda = \sqrt{\frac{8}{|\partial^2 R/\partial \lambda^2|_{(\lambda=\lambda_{res})}}}. \tag{18}$$

This is the equation that we needed to generalize the results in Table 3 beyond a Lorentzian lineshape. In order to show the versatility of the definition in Equation 18, I discuss it in the case of a Fano lineshape. Following reference [122], I define Fano linehsape as:

$$R(\lambda) = R_0 \frac{(F\gamma + \lambda)^2}{\lambda^2 + \gamma^2}, \tag{19}$$

where F is the so-called Fano parameter, and γ is the width in the wavelength domain. Fano lineshape is quadratic around its both extrema and their respective second order derivatives are

$$\lambda_{min} = -\gamma F, \qquad \frac{\partial^2 R}{\partial \lambda^2}|_{\lambda_{min}} = 2R_0 \frac{1}{\gamma^2(1+F^2)}; \tag{20a}$$

$$\lambda_{max} = \gamma / F, \qquad \frac{\partial^2 R}{\partial \lambda^2}|_{\lambda_{max}} = -2R_0 \frac{F^4}{\gamma^2(1+F^2)}. \tag{20b}$$

Hence, by plugging Equation 20 in Equations 18 and 16, the error at the maximum and minimum points of a Fano lineshape are given by

$$\sigma_\lambda^{(min)} = 2\gamma\sqrt{1+F^2}\sqrt{\frac{\sigma_n}{R_0}}\alpha_1; \tag{21a}$$

$$\sigma_\lambda^{(max)} = 2\gamma\frac{\sqrt{1+F^2}}{F^2}\sqrt{\frac{\sigma_n}{R_0}}\alpha_1. \tag{21b}$$

The factor α_1 in these equations is the same as that presented in Figure (22). I will use of this relation in my discussion in Section 4.4.

4.3.2 Linear Regression method for error estimation

Another conventional method of resonance detection is fitting a parametric function to the lineshape around the resonance wavelength [119, 123]. Specifically, linear regression can be used to fit a quadratic function to the data with a relatively small computational load. The fitting function, $f(\lambda)$, is

$$f(\lambda) = p_1\lambda^2 + p_2\lambda + p_3, \tag{22}$$

from which, the resonance wavelength is estimated as $\lambda_{res} = -p_2/2p_1$. Using the matrix representation of linear regression [119], I have calculated the error approximately to be

$$\sigma_\lambda(\Lambda, \sigma_n, \delta) = \sqrt{\frac{3}{N^3}}\frac{\Lambda^2\sigma_n}{4\delta}. \tag{23}$$

The window length (i.e., the number of data samples used in the linear regression) is denoted by N. I have made three assumptions in deriving Equation 23: 1) N is large

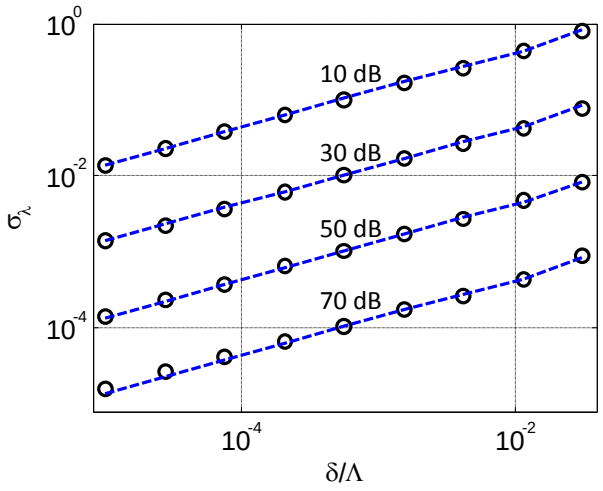

Figure 23: The Monte Carlo simulations (circles) and theoretical estimates (dashed lines) of the resonance detection error (σ_λ) for linear regression method. The theoretical estimate is obtained from Equation 23. The Monte Carlo simulations are performed for $\Lambda = 1$, uniform noise p.d.f, N being the closest integer to $\Lambda/10\delta$, and 10^3 iterations. The number next to each curve is the SNR defined as $20 \log \sigma_n$. The Lorentzian amplitude is unity, as in Equation A.5.

($\gg 1$), so that only the dominant terms in N are kept in the calculations. 2) The fitting window is symmetrically positioned around the actual resonance wavelength. Although the actual resonance wavelength is not known initially, a fairly accurate positioning for this window can be achieved either by few iterations of the linear regression method, or by the absolute minimum method provided its error is relatively small. 3) The resonance linewidth, i.e., Λ in Equation A.5, is known. So, I let $p_1 = 4/\Lambda^2$. This is a reasonable assumption as in most practical cases the resonance shift does not alter the linewidth considerably.

Figure 23 compares the results of the Monte Carlo simulations ($\Lambda = 1$, uniform noise p.d.f, N set to be the closest integer to $\Lambda/10\delta$, and 10^3 iterations) and those estimated by Equation 23. In these simulations, I assume an estimation window symmetrically positioned around the actual resonance wavelength, and calculate the resonance wavelength using $\lambda_{res} = -p_2\Lambda^2/8$ (assuming a known Λ). The good agreement between the two sets of results is visible from Figure 23.

Since my definition of lineshape is similar to that in Appendix A, the result of Equation 23 can be extended to any lineshape with quadratic behavior around the extremum point. Hence, the Λ calculated from the Equations 18 and 20 can be plugged in Equation 23, to give the σ_Λ error when linear regression is used on a Fano resonance:

$$\sigma_\lambda^{(min)} = \sqrt{\frac{3}{N^3}}\frac{\sigma_n}{R_0}\frac{\gamma^2(1+F^2)}{\delta}, \tag{24a}$$

$$\sigma_\lambda^{(max)} = \sqrt{\frac{3}{N^3}}\frac{\sigma_n}{R_0}\frac{\gamma^2(1+F^2)}{\delta F^4}. \tag{24b}$$

Finally, it is worth discussing the implications of Equations 16 and 23 for the optimization of LOD in resonance-based sensors. A conventional definition for LOD is $3\sigma_\lambda/S$, with S being the sensitivity of the resonance [98]. Subject to a fixed δ/Λ, τ (detector integration time per sample, affecting σ_n), and $(N\delta)/\Lambda$; we have LOD $\sim 3\sigma_\lambda \sim 1/Q$ ($Q = \lambda_{res}/\Lambda$). This result is observed both for the absolute minimum method in Equation 16 and for the linear regression method in Equation 23. Whereas, if we use the linear regression method with fixed δ, τ, and $(N\delta)/\Lambda$; Equation 23 results in LOD $\sim 3\sigma_\lambda \sim 1/\sqrt{Q}$ (as opposed to $\sim 1/Q$). This example shows the importance of resonance detection method in determining what figure of merit (e.g., $\sim 1/\sqrt{Q}$ or $\sim 1/Q$) should be used. Similar to the argument above, for any arbitrary case with its specific restrictions, Equations 16 and 23 provide proper analytical tools to optimize LOD based on the specifics of the sensor system.

4.4 Discussion: Statistics tail versus average noise power

Although our estimates of σ_λ for both methods depend on the noise standard deviation (σ_n), the interpretation of σ_n is fundamentally different in these two cases. In the absolute minimum method, the resonance is determined by the sample that has the smallest (i.e., largest negative) noise. Thus, the *tail* section of the noise p.d.f (i.e., the

section corresponding to extreme values) most critically affects the resonance detection. That is to say, if we keep the negative tail of the noise p.d.f intact and replace the rest of the p.d.f arbitrarily, the absolute minimum method is not expected to produce much different σ_λ. In marked contrast to this rationale, the linear regression method leads to a linear relationship between the noise standard deviation (σ_n) and the error (σ_λ), no matter what the noise p.d.f is. Thus, σ_n is directly related to and represented by the *noise power* in the linear regression method.

To better discern the σ_n interpretations, I carried out a numerical experiment on a Fano lineshape subject to a two-level quantization noise. Quantization noise is especially important for near-zero signals. One such example is a resonance dip (see Figure 21d). I let the noise p.d.f, $p_n(n)$, be comprised of two similar Gaussian peaks with different centers μ_1 and μ_2:

$$\begin{aligned} p_n(n) =& \frac{1}{2}\frac{1}{\sigma_0\sqrt{2\pi}}\exp-\frac{(x-\mu_1)^2}{2\sigma_0^2}+ \\ & \frac{1}{2}\frac{1}{\sigma_0\sqrt{2\pi}}\exp-\frac{(x-\mu_2)^2}{2\sigma_0^2}. \end{aligned} \tag{25}$$

By changing the spacing between the quantization levels ($|\mu_1 - \mu_2|$), the standard deviation of the noise changes while the overall tail stays almost the same. In this situation, for the tail-dependent absolute minimum method, we do not expect σ_λ to change with the spacing between the quantization levels. Whereas, for the linear regression method, σ_λ is expected to change almost linearly with the spacing between the quantization levels.

For this numerical experiment, I use a Fano lineshape as defined by Equation 19 with $F = 1$, $R_0 = 1$, $\gamma = 1$, and I focus on the detection of the Fano dip at $\lambda = -1$. The sampling resolution is $\delta = 0.01$, and the standard deviation of each individual Gaussian peak in Equation 25 is $\sigma_0 = 0.01$. Linear regression is applied in a window of $N = 30$ samples around the Fano peak. The results presented in Figure 24 confirm the hypothesis that the performance of the absolute minimum method depends on

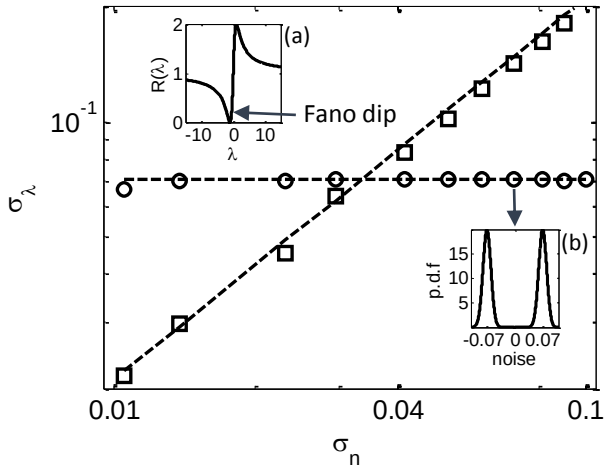

Figure 24: The error in the absolute minimum method (circles) and the linear regression method (squares), in the presence of a bi-level quantization noise. The resonance is a Fano dip with $F = 1$, $R_0 = 1$, and $\gamma = 1$, as shown in inset (a). The standard deviation of the noise (σ_n) is changed by increasing the spacing between the two Gaussian peaks in the noise p.d.f, shown in the inset (b). Each of the two quantized levels is represented by a Gaussian with $\sigma_0 = 0.01$. Dashed lines demonstrate the theoretical formula for: the absolute minimum method, with $\alpha_1 = 0.25$ and $\sigma_n = \sigma_0$ in Equation 21b; and the linear regression method, with σ_n in Equation 24b being the total standard deviation of the noise (which is the same parameter shown on the horizontal axis in this figure).

the tail of the noise p.d.f, while in the linear regression method the noise standard deviation is the determining factor.

It should be noted that the invariability of the error (σ_λ) with the noise standard deviation (σ_n) for the absolute minimum method in this experiment does not contradict the $\sigma_\lambda \sim \sqrt{\sigma_n}$ trend implied by Equation 16. The $\sqrt{\sigma_n}$ trend there was derived for a *self-similar* noise p.d.f subject to merely a linear scaling[1]. However, the standard deviation of noise in the numerical experiment of Figure (24) changes by a shift in the individual peaks, and not a linear scaling. Thus, the α_1 factor also changes when $|\mu_1 - \mu_2|$ varies. The combined variation of σ_n and α_1 results in the nearly-invariable

[1]two random variables X and Y are said to be self-similar if there exists a scaling factor like c such that $p_Y(y) = cp_X(cy)$ for any y.

behavior of σ_λ in Figure 24. This numerical experiment also demonstrates considerable variations of α_1 for noise p.d.fs other than the Gaussian distribution. This fact entails caution in using the $\Lambda\sqrt{\sigma_n}$ trend for absolute minimum method in general.

The formulas derived in Equations 16 and 23 for the resonance detection error allow for the systematic optimization of resonance-based sensors in a large set of applications. Compared to previous results (e.g., Equation 15), the proposed closed-form formulas are not limited to specific cases such as Gaussian noise or Lorentzian lineshape.

4.5 Conclusions

In this chapter, I presented closed-form formulas for the estimation of the error in resonance detection. The focus was on two algorithms with low computational load: absolute minimum method, and linear regression method. The proposed formulas accommodate a wide class of noise statistics and resonance lineshapes. Noise measurements in a conventional laser-scanning setup revealed a dominant quantization noise for near-zero signals. The two above mentioned methods were juxtaposed in the specific case of quantization noise, to discuss that while in the former the error depends on the tail behavior of the noise p.d.f, in the latter the total power of noise is the important noise characteristic. The presented formulas remarkably simplify the optimization process of resonance-tracking sensors.

CHAPTER V

EXPERIMENTAL NOISE STUDY: AN INTERFEROMETRIC TECHNIQUE FOR WAVELENGTH NOISE SUPPRESSION

5.1 Introduction

As I discussed in Section 2.2, the LOD is defined as $3\sigma/S$. Smaller LODs are achieved either by the enhancement of the device sensitivity (S), or through the improvement of detection accuracy (by reducing σ). Although an increase in the device sensitivity can compromise other system performance measures, such as multiplexing capability within a fixed bandwidth, an improvement in the detection accuracy does not cause such compromises. Our discussion throughout this chapter examines the σ in Equation 13 for the resonance tracking of integrated photonic resonators. Spectrally multiplexed sensor arrays function over a relatively wide bandwidth including several multiplexed resonances. Hence, it is also important for a highly multiplexed sensor system to maintain its low LOD (i.e., small σ) over a wide bandwidth.

Sensor uncertainties can arise from device-level and system-level phenomena. A drift in temperature, for example, can lead to a resonance shift practically indistinguishable from the one originated from the binding of the target molecules. For the suppression of the effect of temperature drift, several solutions including active temperature control [4], athermal strucures [72], and on-chip differential referencing [73, 82] have been proposed. Biochemical interference is another source of device-level noise, causing an ambiguity in relating the resonance shift to the presence of the target molecules [124, 125]. To increase the specificity of the sensor and reduce biochemical interference, the surface of the sensing resonator is functionalized with

selective receptor biomolecules to capture only the desired molecules [126].

In contrast to the above-mentioned effects, the system-level uncertainties arise from the inaccuracies of optical interrogation system. For resonance-based integrated sensors, the employment of a tunable laser to scan the spectrum of the resonator is a conventional method for resonance tracking [127]. In this method, shot and thermal noises, either at the laser source or at the detector, are among the fundamental sources of amplitude noise [128]. Additionally, electronic noises and mechanical vibrations at the coupling points in the light path contribute to the random variations, not readily amenable to parametric modeling. Optical spectrum processing [129] and curve fitting [126, 130] have been used to reduce these amplitude noises. In parallel, proper device and system designs help remove some unwanted spectral features such as Fabry-Perot oscillations. On the other hand, to reduce the inaccuracies in laser wavelength, precise wavelength measurement techniques have been proposed to correct for the wavelength deviations of tunable lasers [54, 127, 131].

This chapter investigates the sources of uncertainty in resonance detection for resonance-based lab-on-chip sensors using SiN microring resonators as the sensing device. Microring resonators have attracted extensive attention because of their simple structure and CMOS-compatible fabrication [86, 132]. I present here a systematic and detailed statistical study of the experimental data from an array of SiN microring resonators to compare the relative significance of different sources of uncertainty. The measurement variations are shown to originate from the laser scan, and a simple and effective interferometric correction technique is proposed and demonstrated to suppress this noise by more than one order of magnitude down to $3\sigma \sim 120\,\mathrm{fm}$ (wavelength error). Contrary to conventional fringe-counting methods, this technique takes advantage of the whole interferometric data to correct for sub-periodic wavelength deviations (i.e., wavelength deviations much smaller than the spectral period

of the interferometer). Our technique is simple, low-cost, suitable for on-chip integration, and excludes the use of active temperature controllers and high end wavemeters. The performance is studied across a relatively wide (6 nm) wavelength tuning range, as it is demanded in highly multiplexed sensing systems.

The structure of the chapter is as follows. In Section 5.2, I discuss device theory, fabrication, and experimental characterization setup. The sources of noise and their relative significance are discussed in Section 5.3. Based on these results, Section 5.4 is devoted to an effective wavelength measurement technique for the compensation of the dominant source of noise. The discussion of the results and final conclusions are summarized in Sections 5.5 and 5.6, respectively.

5.2 On-chip Device and Optical System

Figure 25a shows the scanning electron micrograph (SEM) of a one-dimensional array of five microring resonators with a width of 500 nm and an outer radius of about 20 µm, serially coupled to a common bus waveguide with a width of 500 nm. The resonance wavelengths of adjacent resonators differ by 0.25 nm, which is consistent with our design. The fabrication of the device is similar to that explained in Chapter 3, but here I cover the whole surface with the protective oxide layer without any openings.

A setup similar to that described in Section 3.2.3 was used for device characterization. The setup is controlled by LabView software to scan the laser wavelength (from 652 nm to 660 nm) and record the detector readout synchronously. Laser scan rate is 1 nm/s; and the spectrum sampling resolution is 20 fm. Normalized transmission spectrum is calculated by dividing the transmitted power (through the waveguide in Figure 25a) to the baseline power. The baseline power is obtained by low-pass filtering the transmitted power to remove the resonance features of the spectrum.

The presence of five adjacent resonances is clear in Figure 25b. From the repeated resonances, the FSR of the resonators is measured to be 1.65 nm, which is consistent

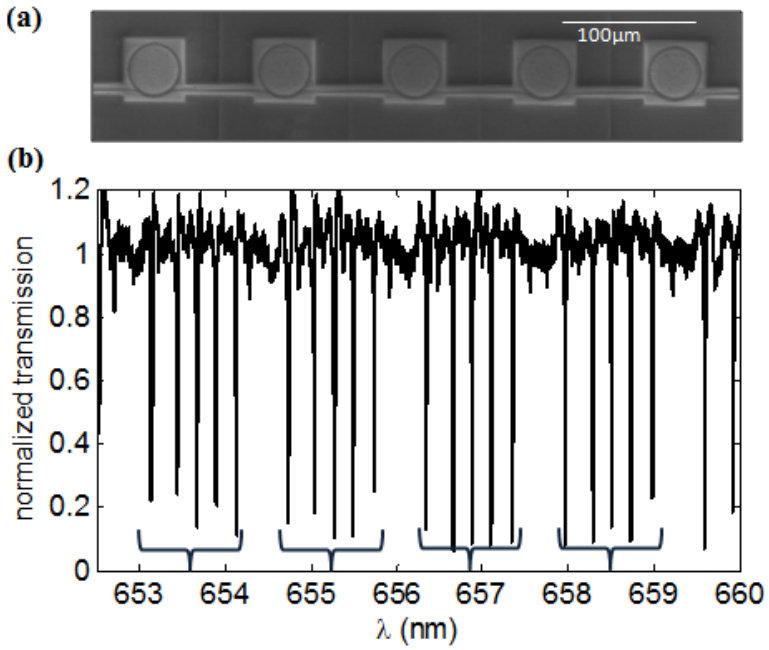

Figure 25: (a) An SEM of five SiN microrings coupled to a bus waveguide. The width of each microring is 500 nm to ensure single-mode operation, and its radius is about 20 µm. (b) The experimental transmission spectrum of the device. Marked resonances are four azimuthal mode orders of the five microrings. The normalized transmitted spectrum is calculated by dividing the transmitted power to the baseline. The baseline is obtained by low-pass filtering the transmitted power.

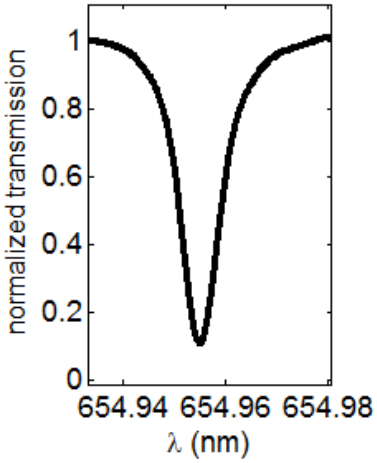

Figure 26: Normalized transmission spectrum for a single resonance shown in Figure 25. The linewidth is about 10 pm, and the Q is 6.5×10^4.

with our finite-element simulations implemented in the COMSOL environment. I measured quality factors of 1.8×10^4 to 7.1×10^4 for the resonators, with an average

of 5.4×10^4 and standard deviation of 1.4×10^4. This variation is primarily caused by fabrication imperfections. The spectrum of a single resonance is shown in Figure 26. The transmission of the device is measured repeatedly 60 times without changing any experimental settings. I will use this ensemble for our statistical analysis in Sections 5.3 and 5.4.

5.3 Noise sources

In this section, noise sources are discussed; and their effects on the repeatability of the resonance detection, i.e., σ in Equation 13, are examined. The result of this examination will then be used to minimize the uncertainty in resonance detection.

5.3.1 Temperature effects

For integrated photonic devices, temperature fluctuations are among the most important environmental factors introducing undesired resonance drifts. In this regard, two distinct mechanisms should be distinguished from each other: 1) homogeneous temperature drifts; and 2) thermodynamic temperature fluctuations. On the one hand, the microrings are in contact with an environment with a time-dependent temperature. Thus, the temporal variations of average temperature lead to undesired resonance shifts. On the other hand, even if the average temperature is ideally stabilized, the temperature of the microring will fluctuate because of its finite volume. The temperature fluctuations of a microring in contact with a heat bath (i.e., the second noise source mentioned above) can be evaluated according to the thermodynamics of this system.

The resonance wavelength drifts (with a standard deviation of $\sigma_{\lambda,T}$) originating from the homogeneous temperature drifts can be expressed in terms of average temperature drifts (with a standard deviation of σ_T) as [133]

$$\sigma_{\lambda,T} = \left(n_{eff}\alpha_L + \frac{\partial n_{eff}}{\partial T} \right) \frac{\lambda_0}{n_g} \sigma_T. \tag{26}$$

Assuming a resonance wavelength (λ_0) of 655 nm, a group index (n_g) of 2.16; an effective index (n_{eff}) of 1.73 (from COMSOL simulations); $\partial n_{eff}/\partial T$ of $2.4 \times 10^{-5}\,\mathrm{K}^{-1}$, close to the thermo-optic coefficient (TOC) of SiN [75]; and an effective coefficient of thermal expansion (CTE or α_L) of $\simeq 2 \times 10^{-6}\,\mathrm{K}^{-1}$ [134, 135]; the temperature sensitivity ($\sigma_{\lambda,T}/\sigma_T$) is about 8.3 pm/K according to Equation 26. Equivalently, from our finite-element calculations of the resonance wavelength of the microring resonators implemented in the COMSOL environment, assuming a TOC of $2.4 \times 10^{-5}\,\mathrm{K}^{-1}$ for SiN; a TOC of $1 \times 10^{-5}\,\mathrm{K}^{-1}$ for SiO_2 [75]; and CTE of $\simeq 2 \times 10^{-6}\,\mathrm{K}^{-1}$; the temperature sensitivity is about 8.2 pm/K.

This type of temperature drift can be avoided by athermal designs that compensate the wavelength drifts originating from the thermo-optic effect in the core with that from the cladding and the substrate of the structure by employing materials with positive and negative TOCs, so that $\partial n_{eff}/\partial T = 0$ [72, 133, 136]. Another compensation technique is to use one or a subset of the microrings as reference. In doing so, each reference microring is isolated from the test solution by a protective layer [73, 82]. The wavelength drifts of the reference microrings are attributed to the temperature variations and subtracted from the wavelength drifts in the sensing microring to compensate for the homogeneous drifts. This differential resonance shift is not affected by a common drift in the temperatures of the microrings.

Although the average temperature drift can be compensated by athermal designs or differential measurements, such techniques do not help with the thermodynamic fluctuations of the temperature, where the contributions of different regions of the device (with either positive or negative TOC regions) are random variables adding up to form the overall resonance shift. The addition of these random variables will always result in an increased overall standard deviation, whether the TOCs are positive or negative. In this sense, SiN or SiO_2 resonators have an inherent advantage over Si resonators, because of their considerably smaller TOCs.

Thermodynamics sets a fundamental temperature noise floor for a microring in contact with a heat bath through the well-known equation [137]

$$< u^2 >= \frac{\kappa T^2}{\rho C V}, \tag{27}$$

with κ, T, ρ, C, and V being the Boltzmann constant, absolute temperature, material density, specific heat capacity of resonator material, and mode volume, respectively. For SiN microrings studied here with $\rho = 3.3\,\mathrm{g/cm^3}$; $C = 7 \times 10^2\,\mathrm{J/kgK}$; and $V \simeq 15\,\mu\mathrm{m}^3$; we will have fundamental thermal fluctuations of $\sqrt{< u^2 >} \simeq 0.2\,\mathrm{mK}$ at room temperature ($T = 300\,\mathrm{K}$). Hence, with a sensitivity of $8.3\,\mathrm{pm/K}$, the corresponding fundamental thermorefractive noise in the system is $\sigma_{\lambda,T} \simeq 2\,\mathrm{fm}$ at room temperature.

5.3.2 Amplitude Noise

Ideally, we need as many data points as the number of model parameters to estimate the resonance lineshape and determine the resonance wavelength. Practically, two types of nonidealities hinder an accurate estimation: 1) random amplitude noises; and 2) the lack of an exact model for the system. While the former results in an uncorrelated noise on the sampled spectrum, the latter generates a correlated pattern in the measurements. Shot noise and thermal noise, either at the laser, at the detector, or at the electronics, are examples of such random noises [138, 139]. Spectrum processing techniques, including denoising and the use of parametric fitting, have been used to reduce the random amplitude noise [129, 140]. On the other hand, fabrication imperfections lead to resonance lineshape deformation, causing a correlated noise that can be most effectively removed by proper modeling. Examples of these deviations include Fabry-Perot oscillations and Fano-like resonance features [141], added to the transmission spectrum because of fabrication imperfections introducing partial reflections.

The effect of random amplitude noises can be studied statistically by Monte Carlo simulations. I used a Lorentzian resonance with $Q = 5 \times 10^4$, an additive white

Gaussian noise, and a sampling rate of 20 fm in our Monte Carlo simulations (with 10^4 iterations per data point), carried out similar to Ref. [84]. The generation of the Lorentzian resonance feature, the addition of the noise, and the determination of the resonance from the noisy resonance feature are performed in MATLAB. The ratio of the amplitude of the resonance feature (1 V) to the standard deviation of the noise is defined as the signal-to-noise ratio (SNR). To estimate the resonance wavelength from the noisy data, I used and compared three different algorithms. The first algorithm simply searches for the minimum of the noisy resonance feature. The second algorithm considers a window of 201 samples, selected symmetrically around the minimum point of the noisy resonance feature, and fits a quadratic polynomial to the data using linear regression. The third algorithm fits a Lorentzian function, within the same window as the second method does, to find the resonance features. The results shown in Figure 27 compare three resonance detection algorithms in terms of the standard deviations of detected resonance.

By performing multiple experimental measurements of microring resonances, the amplitude noise around the resonance wavelengths is measured to be few millivolts. Thus the experimental SNR is around 50 dB, for which the standard deviation of these three detection techniques are respectively, 176 fm, 7 fm, and 5 fm according to the Monte Carlo simulation (see Figure 27). The difference between the quadratic fit and the Lorentzian fit becomes noticeable for higher SNRs, but for the working range of our experiment (with a SNR around 50 dB) a simple quadratic fit is sufficiently accurate and will be used. The expected ~ 7 fm variations of the resonance wavelength using a quadratic fit will be compared against the experimental level of noise in Section 5.3.4 to determine whether the noise mechanism discussed in this section can be the dominant noise factor in our setup.

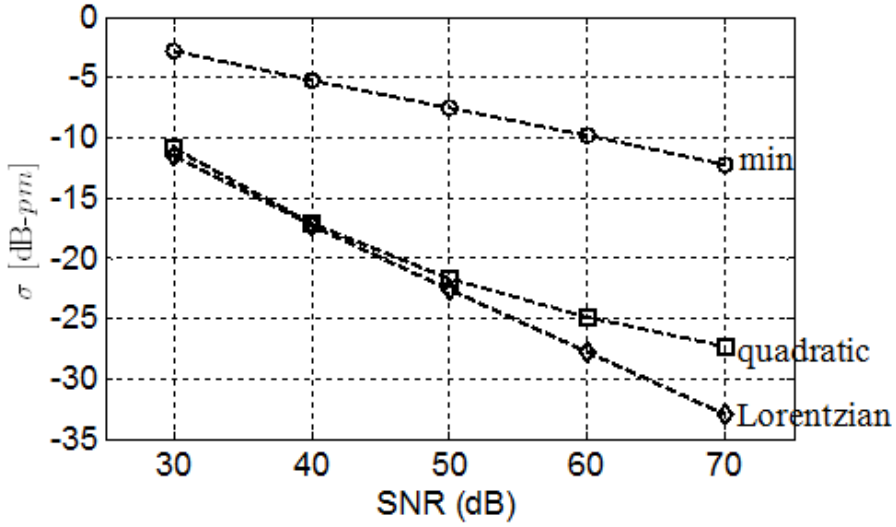

Figure 27: A comparison of the performance of the three detection methods for different noise levels calculated using Monte Carlo simulations. dB_{pm} is defined as $10log(\sigma/1pm)$.

5.3.3 Wavelength noise

Our measurement setup measures $\{\lambda, T(\lambda)\}$ samples, providing the transmission, $T(\lambda)$, at each wavelength, λ. Section 5.3.2 described the effect of the amplitude noises on $T(\lambda)$. This section looks into the wavelength noise on λ. In our setup, the LabView software instructs the laser controller to scan the wavelength with a fixed forward slew rate (r) in time (t) as

$$\lambda(t) = 652\,\text{nm} + r \times t, \tag{28}$$

while collecting the readout of the detector to form data points $\{\lambda(t_0), T(\lambda(t_0))\}$ at each time instant t_0. If the laser wavelength is off by $\delta_\lambda(t_0)$, the detector will record $T(\lambda(t_0) + \delta_\lambda(t_0))$, instead of $T(\lambda(t_0))$, in the absence of any other noises. This deviation can also be modeled as an equivalent amplitude noise of

$$\delta_T(t_0) = T(\lambda(t_0) + \delta_\lambda(t_0)) - T(\lambda(t_0)). \tag{29}$$

However, the conventional representation of this noise is in the form of a noise on the wavelength, and it is referred to as the spectral noise [84] or the wavelength noise

[106].

The prominent sources of wavelength noise in our setup are the phase noise of the laser; the inaccuracy of the tunable laser in setting the wavelength, resulting in a difference between the actual wavelength and the set wavelength of the laser at each time; and the jitters of analog-to-digital converter (ADC). Phase noise of the laser results in the broadening of the linewidth. Thus, the wavelength noise contribution from phase noise is on the order of the effective laser linewidth. The laser used in our setup has a linewidth of $< 300\,\text{kHz}$, which amounts to a wavelength noise of $\sigma_\lambda < 0.4\,\text{fm}$. Practically, the laser linewidth is rarely the dominant limiting factor for the microring resonators discussed here considering typical $\sim 100\,\text{kHz}$ linewidths of existing commercial tunable lasers. For integrated photonic systems, hybrid on-chip Si photonic lasers have been demonstrated with a linewidth of 3.6 MHz, opening up the possibility for $<$ MHz linewidths in near future [142, 143]. Recent proof-of-concept demonstrations also indicate the possibility of kHz (i.e., $\sim$ 10 attometers) linewidths [144].

At the above-mentioned linewidths, typically the variations induced by the *tuning mechanism* dominate the phase noise of the laser, especially where the tuning mechanism is mechanical or thermal. This implies the possibility of employing external on-chip calibration devices, such as Mach-Zehnder interferometers, to improve the performance of system-on-chip devices without requiring complex laser stabilization circuitry. The external-cavity laser of this experiment uses Littman-Metcalf [145, 146] configuration, which is commonplace for commercial external-cavity tunable lasers. A mirror mounted on a rotating arm tunes the cavity length and thus the wavelength. The coarse mechanical movement of the mirror is controlled by a DC motor to cover the whole scan range. For higher-frequency and finer tuning, a piezoelectric actuator with a working range equivalent to few steps of the DC motor is used. The controller of the laser uses the feedback data of an angle detector mounted on the rotating mirror

and a reference table to control the wavelength. Commercial tunable lasers are also available with an internal wavelength meter that directly measures the wavelength to be fed back to the controller. The nominal wavelength tuning resolution of our laser is 20 pm.

5.3.4 Noise measurement

The measurement of σ (total standard deviations in the resonance wavelength) from the experimental data described in Section 5.2 helps evaluate the dominant source of noise. I use the differential resonance shifts here in order to remove the effect of temperature and other environmental drifts. This also eliminates the undesired scan-to-scan variations of the laser wavelength (i.e., the variations of actual wavelength for a fixed set wavelength from one scan to another), although it does not compensate for within-scan variations (i.e., the differential variations of actual wavelengths for any two set wavelengths in each scan). The total scan-to-scan variations were observed to be around 10 pm in the setup without differential resonance measurements. In order to compensate the scan-to-scan variations, I use the average of a number of neighboring resonances for each resonance as its reference resonance wavelength. The N_r neighboring resonances are selected such that the resonance of interest (indexed i) falls in the middle, i.e., these neighbors range from $i - \lfloor N_r/2 \rfloor$ (closest integer smaller or equal to $N_r/2$) to $i + \lceil N_r/2 \rceil$ (closest integer larger or equal to $N_r/2$). I calculate the differential shift for the i-th resonance R_i as

$$\tilde{R}_i = R_i - \frac{1}{N_r} \sum_{j=i-\lfloor N_r/2 \rfloor, j \neq i}^{i+\lceil N_r/2 \rceil} R_j. \tag{30}$$

Assuming the noises on the detected resonances to be independent and identically distributed random variables, the standard deviation of the i-th resonance referenced to its N_r neighboring resonances will be

$$\sigma(i, N_r) = \hat{\sigma} \sqrt{1 + \frac{1}{N_r}}, \tag{31}$$

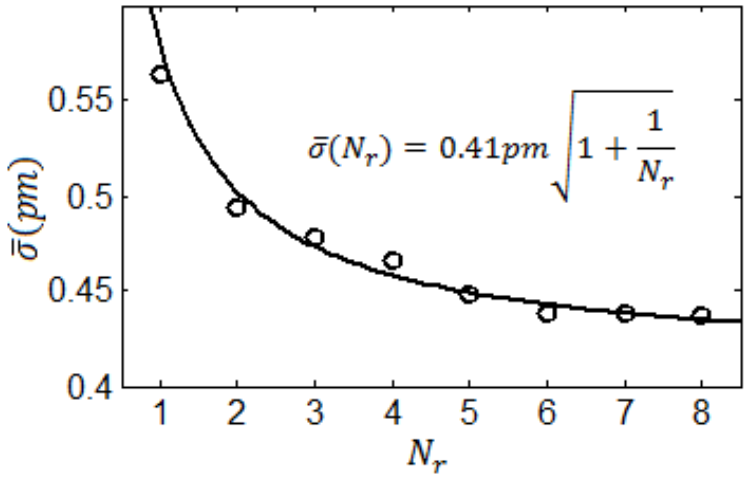

Figure 28: Experimental referencing performance (the standard deviation in Equation 30) with different numbers of reference resonances involved. The solid line is the fit according to the model in Equation 31.

where $\hat{\sigma}$ is the standard deviation of each detected resonance, originating from within-scan wavelength variations. I have plotted $\overline{\sigma}$, defined as: $\sigma(i, N_r)$ averaged over $i \in \{6, ..., 15\}$, in Figure 28. Fitting Equation 31 to this plot determines individual deviations of $\hat{\sigma} = 410\,\text{fm}$, which if accounted for by temperature only, corresponds to a temperature standard deviation of $\sigma_T \sim 0.2\,\text{K}$. As the farthest resonators are located 400 µm apart on the chip and all are scanned in about 8 seconds, the observed resonance variations of 410 fm cannot be solely attributed to temperature changes, as it corresponds to a temporal temperature fluctuation of $\sim 1\,\text{K/s}$, or a spatial temperature gradient of $\sim 2\,\text{K/mm}$, which is very unlikely for the practical condition of our setup. On the other hand, as argued in Section 5.3.2 for the amplitude noise, the measured SNR in our system corresponds to resonance variations of $\sim 7\,\text{fm}$ using a quadratic polynomial fit. According to the nominal 20 pm accuracy of the laser in tuning the wavelength, I believe that the laser scan wavelength noise is the dominant source of noise. Thus, any effort to reduce this noise will result in considerable improvement in the sensor performance. The experiments and observations presented in the Section 5.4 will further support this claim.

5.4 Wavelength correction

In this section, I discuss an interferometric technique to monitor the wavelength and reduce the wavelength noise. The critical point in the resonance detection algorithm, where the dominant noise is added, is the assignment of pertinent wavelengths to the data points homogeneously sampled in time. This wavelength assignment is a projection from the time axis of the measurement to the wavelength axis, and I will refer to this projection as t-λ mapping.

To remove the wavelength noise, I measured a known and well-characterized spectral response simultaneously with our microring sensor, and used the inverse function of the spectral response to find the relative wavelengths. As shown in Figure 29, I used a Michelson interferometer to meet this goal, although the method can work with any other device with a robust spectral response. As I am interested in the relative, rather than absolute, resonance shifts; the interferometer does not need any moving parts [147, 148].

The measurement of the transmission power of the device by detector D_1, and all the parameters of the measurement system (laser scan rate, sampling resolution, etc.) are similar to those explained in Section 5.2. The Michelson interferometer in Figure 29 is designed to have a period of 1.58 pm. This period is chosen to be wide enough so that the system can densely sample the interferometer oscillations, but narrow enough to keep the detector noise of the interferometer much smaller than the interferometer peak-to-peak oscillations. Since analog-to-digital converter (ADC) samples are evenly spaced in time, a uniform wavelength scan is expected to result in a sinusoidal readout by the interferometer detector (D_2 in Figure 29).

The wavelength difference among the data points is calculated using the inverse function of the sinusoidal response of the interferometer. This process is depicted in

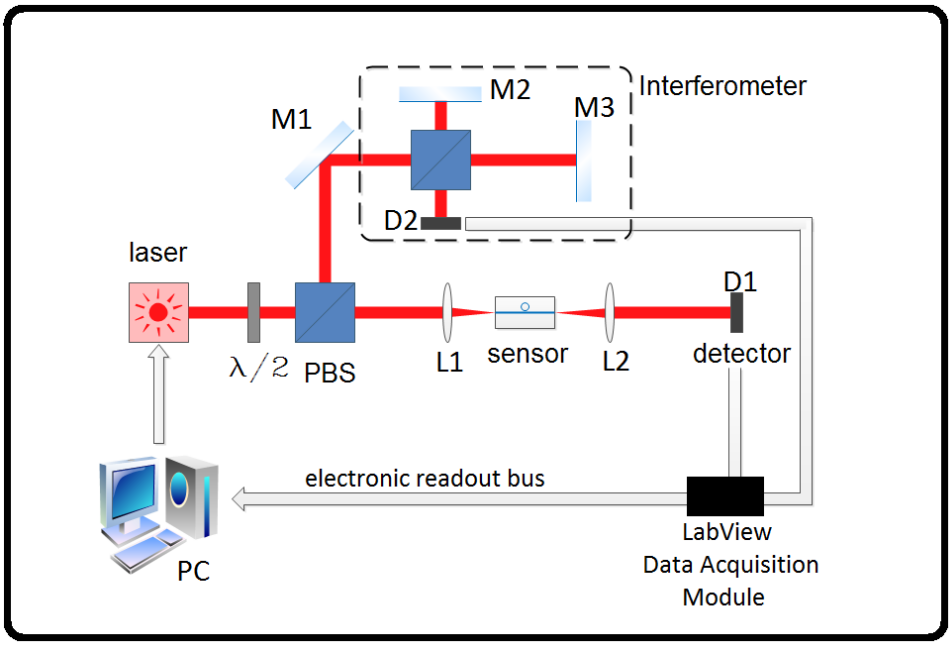

Figure 29: Sensor characterization setup with a Michelson interferometer for the compensation of wavelength noise. After a polarizing beam splitter (PBS), the TM polarization is used as the input to the sensor chip, while the TE polarization is directed toward the Michelson interferometer. M denotes mirror; L, objective lens; D, detector; and $\lambda/2$, half-wave plate. The LabView module includes an analog-to-digital converter that samples the analog readout of the detectors D_1 and D_2, and sends the digitized samples to a personal computer (PC).

Figure 30, where the wavelength offset, $\delta\lambda(t)$, relative to the closest peak (λ_n^{peak}), is

$$\begin{aligned} \lambda(t) &= \lambda_n^{peak} + \delta\lambda(t) \\ &= \lambda_n^{peak} \pm \Delta\lambda \left[\frac{1}{4} - \frac{1}{2\pi} sin^{-1} \left(\frac{I(t) - I_0}{I_1} \right) \right], \end{aligned} \tag{32}$$

in which $I(t)$ is the interferometer readout at time t, and $\Delta\lambda$ is the interferometer period in the wavelength domain. The baseline (I_0) and local interferometer amplitude (I_1) are estimated by fitting a sinusoid locally to the data. The $\pm$ in Equation 32 refers to the temporal positioning of the data point after (for $+$) or before (for $-$) the closest peak (λ_n^{peak}). Equation (32) provides the required inverse function for t-λ mapping.

Figure 31 shows the experimental readout for forward slew rates (i.e., scan speeds) of 0.5, 1, and 6 nm/s. A MATLAB code was prepared to identify and count all the

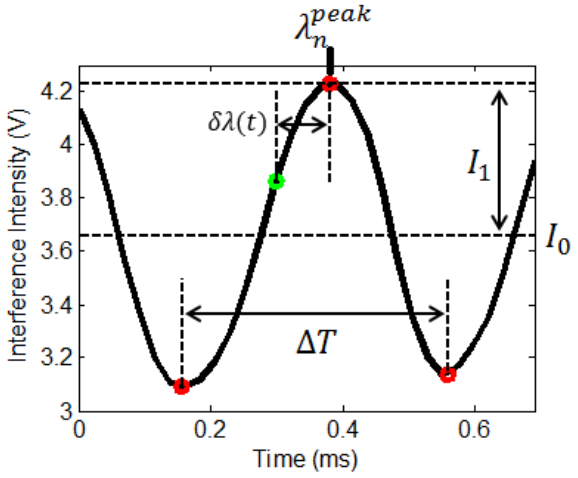

Figure 30: Interferometer recording by the detector D_2 in Figure 29, from 0 to 0.7 ms. The parameters in Equation 32 are defined on this figure. The interferometer recording contains the wavelength deviation information.

interferometer peaks. The data from D_2 is smoothened by a 40-point moving average filter (about half the length of one interferometer period) and local maxima/minima are used to identify the interferometer periods. I_0 is calculated as the average of the amplitudes of the two closets extreme points (minima or maxima) points, and I_1 is calculated as the half the difference of the amplitudes of these two extreme points. Finally, the mapped wavelength for each data point is calculated using Equation 32. Each scan of the spectrum contains around 5000 interferometer peaks. The code was capable of recognizing the scans wherein one or more of these interferometer peaks were not successfully identified. This can happen because of a drastic deviation of the laser scan during one or few of the interferometer periods. Such scans, occurring in about 5% of the cases, were removed from this study as the code has been able to identify them a priori. To avoid the occurrence of such scans, the combination of two interferometers (with fine and coarse periods) and more complex pattern recognition algorithms can be used to increase the reliability.

Next, I will experimentally investigate the efficiency of the t-λ mapping algorithm in reducing the wavelength noise of the sensor structure in Figure 29. The resonances

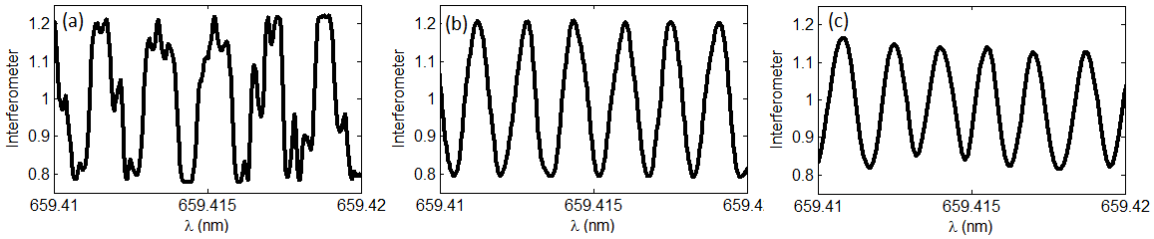

Figure 31: The interferometer recording in the setup of Figure 29 (measured by D_2) for different laser scan speeds. Forward slew rates are (a) 0.5 nm/s (b) 1 nm/s (c) 6 nm/s. The parameter λ shows the nominal wavelength, calculated by a linear mapping from the time domain (i.e., time instances at which the ADC samples the detectors) to wavelength domain, assuming that the laser scan is linear. A linear scan results in a sinusoidal recording. The deviations observed in these figures correspond to the deviations of the laser wavelength from linear scan. The deviations are random in general.

are studied in (R_i,R_j) pairs, where $|i-j| \neq 5, 10$, or 15 (to exclude the pairs corresponding to different azimuthal modes of the same resonator). This provides us with $\binom{20}{2} - \frac{20\times 3}{2} = 160$ pairs in total, where $\binom{20}{2} = 20!/2!(20-2)!$. For each pair, the standard deviation of the spectral spacing $(R_i - R_j)$ is calculated over the ensemble of 60 measurements. A representative probability distribution function for two resonances, with $R_i - R_j = 5.097\,\text{nm}$, is shown in Figure 32a.

The average over all 160 pairs using the interferometric technique is $\sigma_{int}^{avg} = 41\,\text{fm}$, compared to $\sigma_0^{avg} = 585\,\text{fm}$ without the interferometer. The smallest standard deviation in this data set is 15 fm ($3\sigma_{int} = 45\,\text{fm}$) corresponding to 11th and 13th resonances, $R_{13} - R_{11}$. The standard deviation of σ_{int} over the 160 resonance pairs is 19 fm. A histogram of the standard deviations for the resonance pairs, with and without the interferometric correction, is illustrated in Figure 32b. The ability of the interferometer-based technique for reducing wavelength error is evident in from Figure 32.

I also calculated the statistical distribution of the improvement ratio ($I.R.$) in terms of standard deviations, i.e.

$$I.R. = \frac{\sigma_0^{(i,j)}}{\sigma_{int}^{(i,j)}}, \tag{33}$$

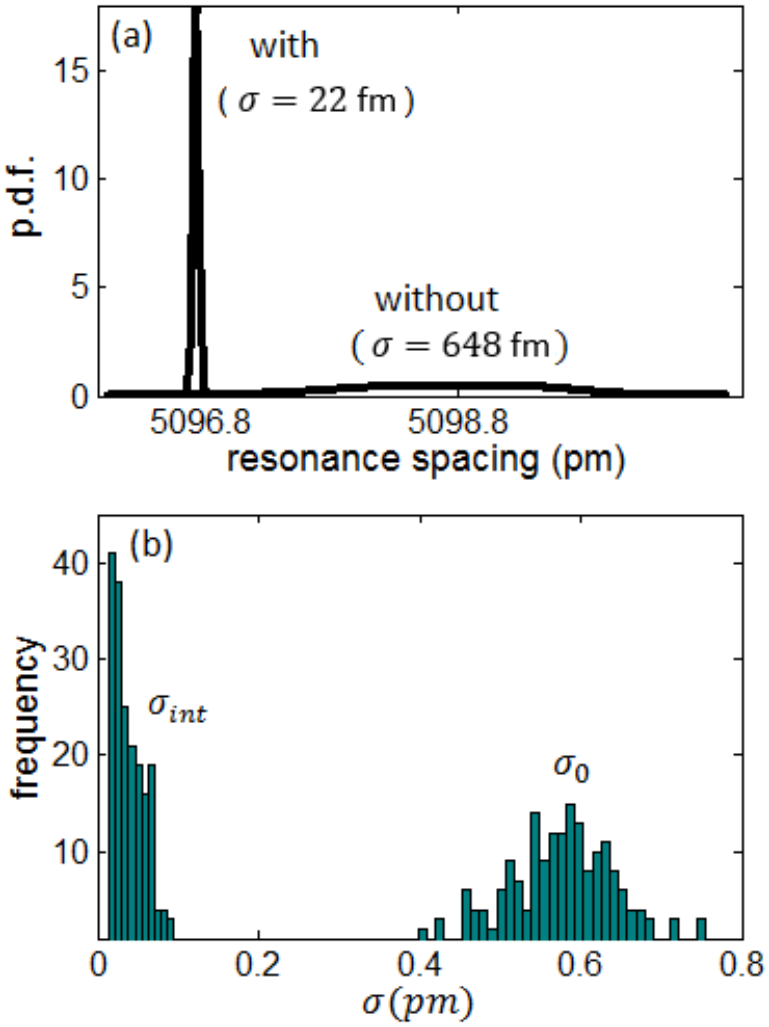

Figure 32: The comparison of the standard deviation of resonance detection with and without t-λ mapping. (a) An example of the probability distribution functions for a resonance pair with an average spectral spacing of $R_4 - R_{20} = 5.097\,\text{nm}$. (b) The histograms of standard deviations with (σ_{int}) and without (σ_0) t-λ mapping.

for above-mentioned (i, j) pairs of the resonances, where $\sigma_{int}^{(i,j)}$ and $\sigma_0^{(i,j)}$ denote the standard deviation of $R_i - R_j$ after correcting the wavelength with t-λ mapping, and that with simple linear mapping (without any correction). The improvement ratio has an average of ~ 18, a median of ~ 16, and a standard deviation of ~ 9. This clearly shows the power of our proposed correction technique in reducing the dominant noise factor in the sensor structure of Figure 25a.

5.5 Discussion

Accurate resonance wavelength detection in resonator-based lab-on-chip sensors is a crucial step for achieving low LODs and reliable, repeatable performance. The results shown in Figure 32 suggest that our t-λ mapping technique improves the detection accuracy of the sensor in Figure 25a by more than one order of magnitude down to an average standard deviation of $3\sigma = 120\,\text{fm}$, leading to an enhancement in the LOD by a similar factor. This observation reveals that the deviations in the initial system ($\sigma_0^{avg} = 585\,\text{fm}$ in Section 5.4, or equivalently, $\sqrt{2}\hat{\sigma} = 580\,\text{fm}$ from Section 5.3.1) were dominated by the wavelength noise of the laser. The results also demonstrate the possibility of achieving an accuracy of $3\sigma \sim 45\,\text{fm}$ (calculated from the 60 measurements of two specific resonances) using only one reference resonator and without cooling or temperature stabilization. The interferometer measurements are carried out in parallel to the transmission measurements of the device, and the required data processing involves a moving-average filtering and few mathematical operations per data point. Thus, even using modest processors, our technique does not reduce the detection speed.

I did not use any temperature control or cooling for our measurements. Using a cooled and thermally stabilized fiber-based interferometer, with an FSR of 40.8 MHz, a repeatability of $\sim 0.4\,\text{fm}$ has been reported for microtoroids [54]. This accuracy, however, entails a temperature stabilization better than $\sim 1 \times 10^{-4}\,\text{K}$ for an SiO_2 microtoroid resonator. Our setup does not require any temperature control on the resonators or on the interferometer. Using thermal stabilizers in our system can improve the measurement accuracy, but such techniques add considerable complexity to the sensor and limit its practical application, especially in point-of-care and resource-limited settings. Furthermore, it has been the objective of this work to achieve accuracy homogeneously over a relatively wide bandwidth (here 6 nm), which is of interest for the applications requiring a high degree of spectral multiplexing. It

should be mentioned that the use of high-end laboratory equipment might obviate the need for an interferometer, but increases the complexity, cost, and size of the system considerably [37, 52]. Note that our technique can be readily used in many existing photonic resonance-based sensor chips to improve the detection limit by at least one order of magnitude without being limited to a specific resonator type, substrate material, or an interferometer configuration.

In another report, a 25-GHz Fabry-Perot etalon has been used as a wavelength reference to achieve a root-mean-square noise of 220 fm (i.e., a 3σ noise 660 fm) for Si microrings [127]. The technique proposed here takes advantage of the amplitude of the interferometer reading at each data point to correct the associated wavelength deviation, as opposed to relying only on the data from the interferometer peaks. Therefore, this technique can correct for the sub-periodic deviations between the adjacent peaks. Such sub-periodic deviations are completely missed in the simple interpolation of the wavelength values measured only at the peaks.

Although I have used SiN microrings as the sensing resonators, the concept discussed here is applicable to other resonance tracking systems. The integrated version of this technique, e.g., realized in the form of a Mach-Zehnder interferometer, benefits point-of-care and handheld bio/chemical sensing applications [149]. Furthermore, it allows for low-cost tunable lasers to scan the spectrum without requiring complex feedback circuitry for controlling the wavelength. In another aspect, our technique mitigates the issue of laser idle time in resonance-free bands of the spectrum. Adding a coarse interferometer (with a larger period), working in tandem with the fine interferometer used here, enables higher scan rates in resonance-free bands of the spectrum without loss of accuracy. As the internal configuration of the external cavity diode laser used here is one of the most widely used configurations in commercial lasers, I expect the conclusions here to be beneficial for other studies using similar setups. It should also be noted that because of its general nature, our technique can be applied

to other on-chip resonance-based photonic sensors, such as photonic crystals and slot microrings.

To put the numbers from this study in a practical context, I discuss the specific case of cardiac biomarker detection for the diagnosis of heart failure. Cardiac Troponin I (cTnI) is one of the most widely used blood biomarkers for the detection of myocardial injury [150]. For a typical sensitivity of $\sim 100\,\mathrm{pm/nm}$ for the SiN microrings (i.e., $\sim 100\,\mathrm{pm}$ resonance shift for the deposition of a $1\,\mathrm{nm}$ layer with the refractive index of 1.45), a wavelength resolution of $3\sigma \simeq 120\,\mathrm{fm}$ demonstrated here corresponds to an equivalent layer of about $1\,\mathrm{pm}$ thick, as the thinnest layer that the sensor is able to detect on its surface. Assuming a diameter of $4\,\mathrm{nm}$ for cTnI (the typical dimension of proteins with about 200 residues, as is the case for cTnI), a $1\,\mathrm{pm}$ layer on the SiN microring sensor amounts to the volume of about 4000 cTnI molecules. With a typical surface coverage of 10^{12} antibodies per cm^2 [151], about 10^6 antibody molecules will be available on the microring surface after antibody immobilization. As the smallest number of cTnI molecules on the surface that the sensor is able to sense is 4000, the smallest cTnI concentration that the sensor can sense is $4000/10^6 \times K_D$ (K_D is dissociation constant for cTnI/anti-cTnI). Assuming a dissociation constant in the nanomolar range (i.e., $K_D \sim 1\,\mathrm{nM} \sim 24\,\mu\mathrm{g/l}$, as the molecular weight of cTnI is $24\,\mathrm{kDa}$), the smallest cTnI concentration that this sensor can sense is $\sim 0.08\,\mu\mathrm{g/l}$. This detection limit is within the clinically relevant range for cTnI [152, 153]. Therefore, using our proposed technique, clinically relevant concentrations of cTnI can be detected without the need to time-consuming sample preconcentration methods [103]. It should be noted that in order for the sensor system to take advantage of the wavelength correction technique discussed here, proper surface chemistry prohibiting non-specific binding should be used to avoid the dominance of biochemical noises in practice [154]. In this sense, the estimated value here (i.e., LOD $\sim 0.08\,\mu\mathrm{g/l}$) will be a lower bound for the LOD of the complete sensor with the surface chemistry

included.

5.6 Conclusion

A detailed study of noise sources in the laser-scanning setup for multiplexed integrated photonic sensors, which is a common configuration in many sensing scenarios, shows that the major source of noise is the inaccuracy of the laser in setting the wavelength. An efficient interferometric technique relying on sub-periodic wavelength correction was proposed and experimentally demonstrated to improve the detection accuracy by more than one order of magnitude from $3\sigma = 1.8\,\text{pm}$ to $3\sigma = 120\,\text{fm}$ (with σ being the standard deviations of measured resonance wavelength). This is the best reported repeatability at room temperature for the resonance detection of integrated microring and photonic crystal resonators to the best of our knowledge. Our technique is distinct from conventional interferometry techniques in its capability of sub-periodic wavelength correction enabled by the use of an inverse algorithm. The corresponding improvement in the LOD of the lab-on-chip sensors, by adding a simple interferometer without any temperature stabilization or cooling, is a main advantage of our technique. In addition, it allows for the realization of lab-on-chip sensor systems having a low-cost on-chip tunable laser without complicated control circuitry. Thus, our technique can remarkably benefit bio/chemical lab-on-chip resonance-based integrated photonic sensor systems.

CHAPTER VI

CONCLUSION

6.1 Summary of Achievements

Optical and photonic technologies offer unique and versatile solutions for critical applications such as public and private health monitoring, communications, and manufacturing. Novel nanofabrication techniques, on the other hand, have enabled the realization of ever shirking devices. On-chip photonic resonators, the fabrication of which was made possible in the recent decade thanks to the progress in nanofabrication, provide a sensitive and scalable transduction mechanism that can be used in biochemical sensing applications. The recognition and quantification of biological molecules is of great interest for a wide range of applications from environmental monitoring and hazard detection to early diagnosis of diseases such as cancer and heart failure.

One major aspect of this dissertation is the development of a sensitive and scalable biosensor platform based on an optimized array of silicon nitride (SiN) microring resonators for multiplexed, rapid, and label-free detection of biomolecules. The photonic design of the sensor, its nanofabrication process development, surface chemistry, microfluidics integration, and optical characterization are addressed. The optimization of the photonic sensor is investigated theoretically and experimentally, and proper estimates of fundamental figures of merit, such as the limit of detection (LOD) and false positive rate, are presented.

False positive rate and LOD in bio/chemical resonance-based sensors are determined by the minimum wavelength shift the system can resolve. I conducted an extensive investigation of the sources of noise in the sensor system. The investigation

included experimental measurements of wavelength noise, an evaluation of the thermodynamic noise floor of the resonator, and Monte Carlo simulations of the effect of additive noise. Despite employing a high-end laser in the setup (a New Focus tunable laser), the dominant noise was found to originate from the wavelength tuning mechanism of the tunable laser. Small fluctuations of the wavelength scan speed lead to deviations in the laser wavelength, which are detrimental for sensitive experiments using microrings. I proposed and demonstrated an interferometric referencing technique and an inverse function algorithm that proved to suppress this noise by more than one order of magnitude down to $3\sigma_\lambda \sim 120\,\text{fm}$. This technique does not require any temperature control in the system and operates well at the room temperature. Since other prominent manufacturers of such tunable lasers, such as Agilent and Santec, use a similar tuning mechanism[1], the interferometric technique proposed here is expected to improve the accuracy of measurements in a wide variety of characterization setups.

Achieving this level of noise, the next question in the design of the sensor was that of optimal power level. The higher the power of the light that probes the resonator, the higher the signal-to-noise ratio (SNR), and the lower the resonance detection error. However, one would like to use as low of a power as possible, while maintaining a reasonable LOD and false positive rate. There exists a threshold on the laser power above which other sources of noise, such as wavelength noise, become dominant and as a result the benefits from higher powers saturate. Therefore, the optimal design of the sensor should not surpass this threshold. To find this threshold, analytical formulas are required to calculate the error in resonance detection with respect to the additive noise in the system (e.g., shot noise, thermal noise, electronic noise, etc.) I studied this problem for two common resonance detection methods (absolute minimum method and the quadratic fit method using linear regression) and formed closed-form relations for the above-mentioned purpose. The study is based on a

[1] based on Littman/Metcalf configuration [145]

rigorous statistical analysis, and the results match the Monte Carlo simulations over a wide range of parameters. Other outcomes of this study include:

- Clarifying the conditions under which the commonly used figure of merit (FOM = $1/QS$) is an accurate measure for resonator optimization and discussing alternative figures of merit such as FOM = $1/\sqrt{Q}S$.

- A comparison of the fundamental characteristics of the absolute minimum method and the linear regression method for resonance detection, and providing guidelines to choose between the two with regard to the working conditions of the sensor.

- Proposing a novel figure of merit based on the curvature of resonance that unifies the optimization approaches relying on SNR and quality factor. This figure of merit enables systematic optimization of the sensor parameters, such as waveguide-resonator coupling.

Another aspect of this dissertation is the development and optimization of nanofabrication processes for the realization of the sensor in the SiN platform. Major nanofabrication challenges such as electron beam lithography charge-up are explained and addressed. Furthermore, a simple and effective oxide lift-off protocol using swabbing is proposed. The technique improves the reliability of lift-off for thin films with poor adhesion, compared to the conventional techniques using sonication. This method is promising for a variety of research or commercial applications facing similar adhesion problems.

The next steps of the sensor realization required surface chemistry and microfluidics integration. I developed and optimized two surface chemistry protocols (based on homobifunctional and heterobifunctional linkers) for PEGylation and NHS-activation of SiN surfaces. The protocol using the heterobifunctional linker was adopted for further experiments owing to its superior repeatability.

The microfluidic flow cell was integrated using an acrylic holder I designed and perfected to hold the flow cell and SiN chip together by applying a gentle force. While providing reasonable sealing (for flow rates up to $\sim 100\,\mu L/min$, which is considerably higher than practical requirements), this structure helped avoid using conventional bonding techniques for sealing the channels. The majority of general bonding techniques damage the delicate bio-receptor monolayer; but my approach of integration keeps it intact. The microfluidic flow cells were cast in Polydimethylsiloxane (PDMS) using an SU-8 mold. For this purpose, I developed a photolithography protocol on Microtech LW405 Laserwriter tool. This tool has different lens systems and exposes the resist through a raster scan of custom CAD (computer aided design) patterns. As a result, it was more flexible in my design phases compared to conventional photolithography using optical masks.

6.2 Future Directions

6.2.1 Multiple Interferometric Referencing

A promising direction in the continuation of the work presented in this dissertation is multiple interferometric compensation of wavelength noise. I used a single interferometer here. However, the use of two or more interferometers with different periods helps increase the reliability of the compensation. For example, an interferometer with a larger period can be used for coarse tracking of the wavelength, while another interferometer with a smaller period measures the fine deviations of the laser wavelength. This combination can further suppress the wavelength noise in the system.

6.2.2 Resonance Detection Error Analysis

I used the linear regression method for fitting a quadratic function to the resonance lineshape. The linear regression method can be used as well for fitting higher order polynomials to the lineshape. Following the same rationale I have outlined, it is possible to derive closed-form relations for the error when higher order polynomials

are fit to the resonance. This study will be interesting as it can lead to closed-form relations for a general parametric fit, such as a Lorentzian fit, with an arbitrary Taylor expansion.

Another possible theoretical direction concerns the error in the absolute minimum method. As discussed in Section 4.3.1, the resonance detection error in this method depends on the specific probability distribution function (p.d.f) of noise. However, as observed in Figure 22, the error for all three noise p.d.fs studied (i.e., Gaussian, uniform, and Laplacian) converges at a sampling rate of $\delta/\Lambda \sim 0.05$. Identifying a *golden* sampling rate at which the error is independent of the noise p.d.f provides further insight into the performance characteristics of this method.

6.2.3 Low-temperature Porous Oxide Coating

I have observed the formation of porous SiO_2 when the oxide deposition is performed at low temperatures. Figure 33a shows a multi-layer structure showing several types of SiO_2. Although larger pores can be created using HF etching, the exposure of low-temperature SiO_2 (deposited by e-beam evaporation or PECVD at 100^oC) to oxygen plasma results in nanopores observable in an SEM image of the material. My measurements of a microring sensor covered with the porous oxide formed through HF exposure showed that this device is sensitive to the changes in ambient humidity, which makes this device a candidate for humidity sensing [155, 156].

6.2.4 Toxin Detection Using Glycans

In addition to the glycan/lectin pairs discussed here, I performed tests on several other glycan/lectin pairs. The result of my experiments on a surrogate of Cholera toxin (B subunit of Cholera toxin, CTB) is reported in Reference [62]; and my experiment on Concanavalin A in Reference [157]. Using higher orders of multiplexing, the sensor is readily scalable to accommodate the detection of more proteins or toxins by having a larger panel of glycans immobilized on the microrings. A challenge in this regard is the

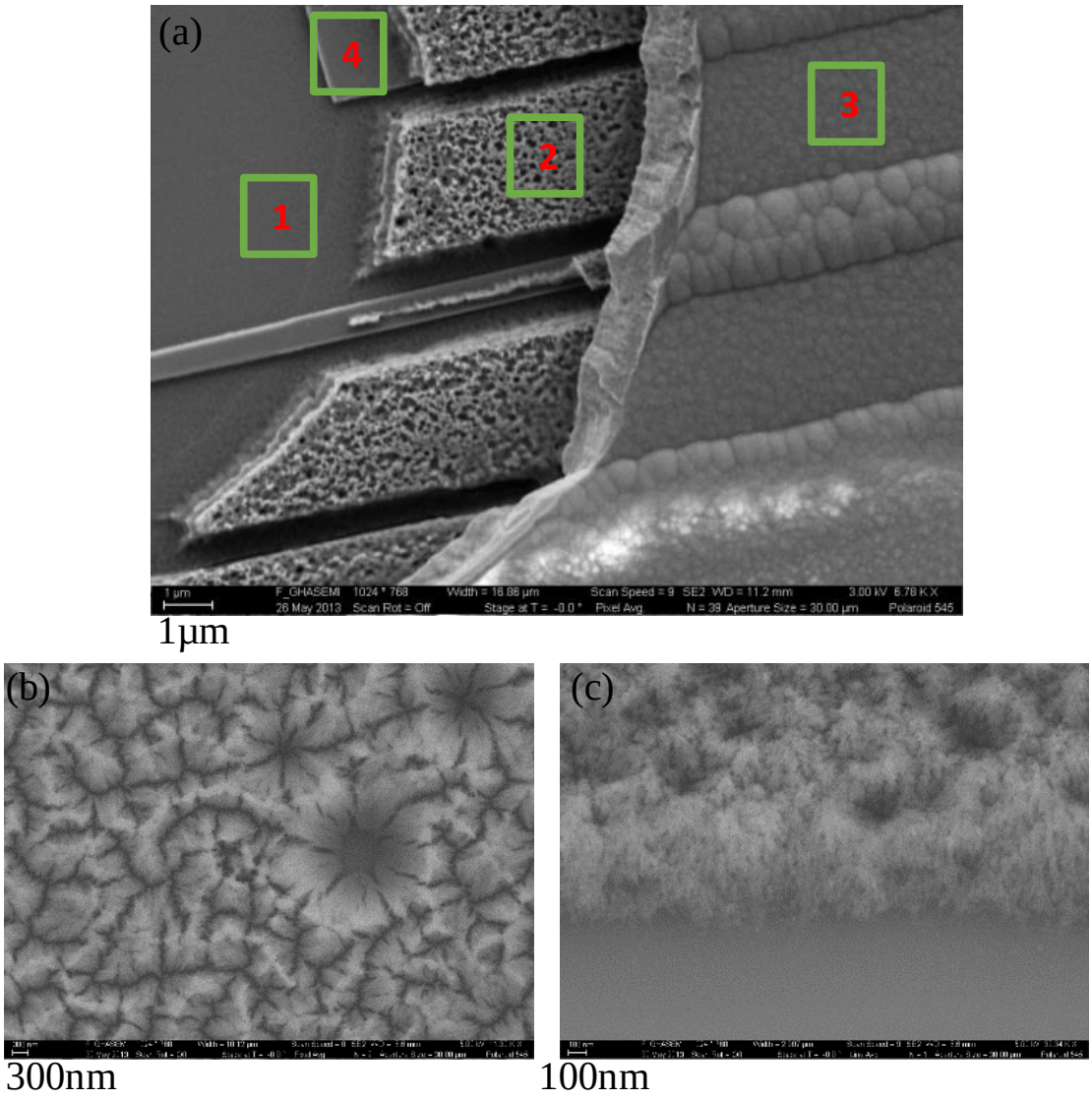

Figure 33: An SEM of samples with porous SiO_2. (a) 1: Thermal oxide, 2: HF-etched evaporated oxide, 3: Evaporated oxide (by CHA Industries, Inc. e-beam evaporator), 4: Stoichiometric LPCVD SiN. (b) and (c) HF-etched low-temperature PECVD oxide.

use of the BioForce Nano-eNabler tool for local printing of the glycans. This printing tool requires a highly humid chamber for proper printing. However, high humidity de-activates the NHS functional groups on the microrings. Inkjet printers have been used for the printing of multiple bio-receptor solutions previously [73]. But, inkjet printers typically require a relatively large volume of the solution in their reservoir

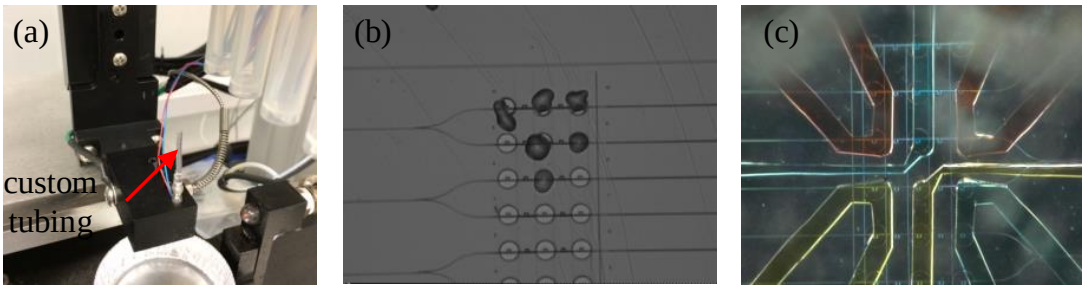

Figure 34: (a) The custom-made tubing to fit on the inkjet printer tool. The solution is fed by a micro-pipette into the tubing. (b) Several drops of a PBS buffer printed on a SiN surface using the custom-made tubing. (c) Microfluidic flow cells as an alternative for the local delivery of bio-receptor solutions.

to work properly. To address this issue, I modified the analyte intake section of the inkjet printer available at the Georgia Tech shared cleanroom facility by replacing its analyte input channel with a custom tubing through which I could feed small volumes of the glycan solution ($\sim 1 - 10\,\mu L$). This custom-made system is shown in Figure 34a, and the result of printing several drops of a PBS buffer is shown in Figure 34b.

Another solution to get around the above-mentioned problem is developing microfluidic flow cells for the delivery of the glycan solutions. The same microfluidic structure used for analyte delivery can be used for this purpose. I designed and fabricated the mold and PDMS flow cell, and I tested this method with colored water as shown in Figure 34c. The colors did not mix at least for 12 hours, which shows the potential of this method for immobilizing multiple types of glycans.

In order for the sensor to be able to accommodate larger panels of glycans, I designed, fabricated, and tested a spectrally/spatially multiplexed sensor. The devices, shown in Figures 35a-e, have power dividers delivering the light to parallel waveguides. I fabricated the power divider using smooth Y-junctions and also using 3-dB couplers [158]. Both methods of dividing power worked properly and this structure can be used for the realization of higher orders of multiplexing.

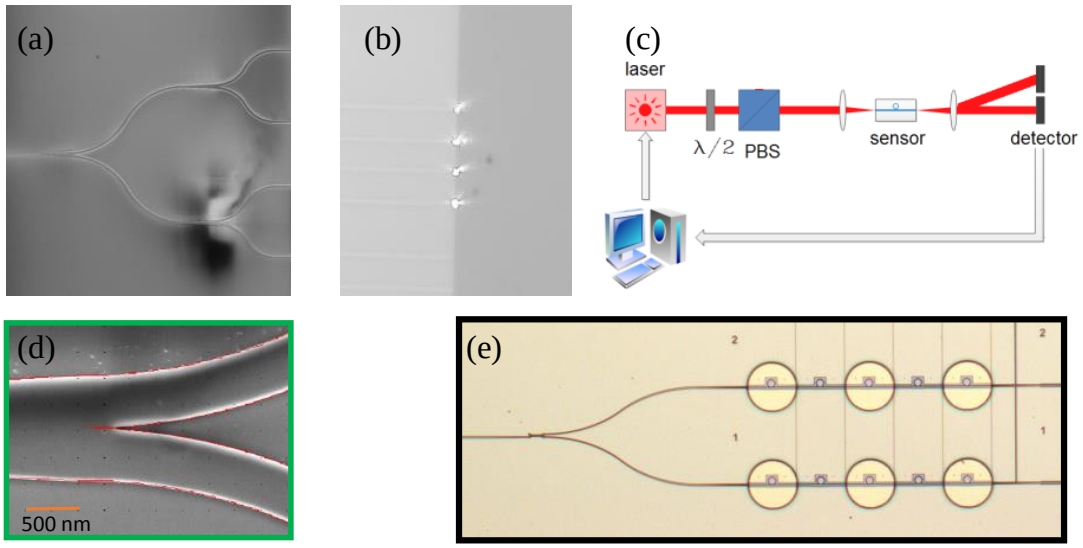

Figure 35: Spectrally and spatially multiplexed sensor devices. (a) An SEM of the device with Y-junction power dividers. (b) A microscope image of the output waveguides under test. The output laser light scatters to the top at the cleaved edges of the waveguides. (c) A schematic diagram of a setup with two detectors simultaneously recording the signal from two parallel waveguides. (d) An enlarged view of the SEM of the Y-junction power divider. (e) A microscope image of the device with a 3-dB coupler power divider.

APPENDIX A

STATISTICAL ANALYSIS OF ABSOLUTE MINIMUM METHOD

In this appendix, the error resulting from amplitude noise is calculated for absolute minimum method. I start from the exact form of p.d.f for the error of resonance detection; derive proper scaling rules under self-similarity assumption of noise p.d.f, and employ these rules in a parameter-reduction process; and simplify the problem by discussing different terms of the Taylor expansion of the error. Finally, the asymptotic behavior of the error is calculated using extreme value theory [159], and a parametric relation for the error is presented.

The amplitude of the i-th measured sample, D_i, is

$$D_i = R_i + n_i, \tag{A.1}$$

where the resonance function R_i is the ideal resonance function (power transmission of the device) for the wavelength at which the i-th sample is measured, i.e. $R(\lambda_i)$. n_i is the amplitude noise of this measurement. The probability of the i-th sample to be the absolute minimum is:

$$\begin{aligned} p(i) &= \int_{n_i=-\infty}^{+\infty} \prod_{j\neq i} P(R_i + n_i < R_j + n_j) p_n(n_i)\ \mathrm{d}n_i \\ &= \int_{n_i} \prod_{j\neq i} P(n_j > R_i - R_j + n_i) p_n(n_i)\ \mathrm{d}n_i \\ &= \int_{n_i} \prod_{j\neq i} Q(n_j)\ p_n(n_i) \mathrm{d}n_i, \end{aligned} \tag{A.2}$$

where the function $P(.)$ denotes the probability that the condition inside the parentheses is true. $Q(.)$ is defined as:

$$Q(x) = \int_{n=x}^{+\infty} p_n(n)\ \mathrm{d}n, \tag{A.3}$$

where p.d.f of the noise is denoted by $p_n(n)$.

Assuming a symmetric lineshape and sampling points, and with a minimum point at $\lambda = 0$, the average detected resonance is zero and the standard deviation of the detected resonance is

$$\begin{aligned} \sigma_\lambda^2 &= \textstyle\sum_i p(i) \,.\, (i\delta)^2 \\ &= \textstyle\sum_i (i\delta)^2 \int_{n_i} \prod_{j\neq i} Q(R_i - R_j + n_i) p_n(n_i) \, \mathrm{d}n_i. \end{aligned} \tag{A.4}$$

For small-noise cases, where σ_λ is much smaller than resonance linewidth, the resonance can be approximated by its leading Taylor expansion term. For a Lorentzian resonance with a normalized amplitude we have

$$R(\lambda) = 1 - \frac{1}{1 + (2\lambda/\Lambda)^2} \tag{A.5a}$$

$$\approx \frac{4}{\Lambda^2}\lambda^2, \tag{A.5b}$$

where Λ denotes the full-width at half-maximum (FWHM) linewidth. Sampling this function with a resolution (i.e., the wavelength difference between adjacent samples) of δ results in $R_i \approx (2i\delta/\Lambda)^2$. The rest of our analysis here is based on the assumption that the resonance function can be approximated by a quadratic function around its resonance, which is for instance the case for Lorentzian and Fano resonances (Although Fano resonance is asymmetric, for small intervals around its extremum points it can be considered a symmetric quadratic function). Thus,

$$\sigma_\lambda^2 = \sum_i (i\delta)^2 \int_n \prod_{j\neq i} Q((2\frac{\delta}{\Lambda})^2(i^2 - j^2) + n) p_n(n) \, \mathrm{d}n. \tag{A.6}$$

I assume that the noise samples are independent and identically distributed (iid), and replace n_i with n from this point. The three parameters of our interest here are Λ, σ_n (noise standard deviation), and δ. It can be seen from Equation A.6 that for

any arbitrary $\alpha > 0$,

$$\sigma_\lambda(\Lambda, \sigma_n, \alpha\delta) = \alpha\ \sigma_\lambda(\Lambda/\alpha, \sigma_n, \delta), \tag{A.7}$$

$$\sigma_\lambda(\Lambda, \alpha\sigma_n, \delta) = \sigma_\lambda(\sqrt{\alpha}\Lambda, \sigma_n, \delta). \tag{A.8}$$

In the above equations, the noise p.d.f is assumed to be self-similar for various values of standard deviation, so that if we scale the standard deviation by α we have $p_n^{'}(n) = p_n(n/\alpha)/\alpha$. The scaling rules allow us to reduce the three initial parameters to one parameter by defining the function $\bar{\sigma_\lambda}$ as

$$\sigma_\lambda(\Lambda, \sigma_n, \delta) = \delta\ \bar{\sigma}_\lambda(\frac{\Lambda}{\delta}\sqrt{\sigma_n}). \tag{A.9}$$

Using the Taylor expansion of $\bar{\sigma}_\lambda(\Lambda\sqrt{\sigma_n}/\delta)$, i.e.:

$$\bar{\sigma}_\lambda(\frac{\Lambda}{\delta}\sqrt{\sigma_n}) \approx \alpha_0 + \alpha_1\frac{\Lambda}{\delta}\sqrt{\sigma_n} + \alpha_2(\frac{\Lambda}{\delta}\sqrt{\sigma_n})^2 + ..., \tag{A.10}$$

we arrive at

$$\sigma_\lambda(\Lambda, \sigma_n, \delta) \approx \delta\alpha_0 + \Lambda\sqrt{\sigma_n}\alpha_1 + \frac{1}{\delta}(\Lambda\sqrt{\sigma_n})^2\alpha_2 + ... \tag{A.11}$$

In order for $\sigma_\lambda(\Lambda, \sigma_n, \delta)$ to be non-singular at $\delta \to 0$, we should have $\alpha_i = 0$ for $i > 1$. Therefore, the dominant term in Equation A.11 at the limit of $\delta \to 0$, is the second term:

$$\sigma_\lambda(\Lambda, \sigma_n, \delta) \approx \Lambda\sqrt{\sigma_n}\alpha_1. \tag{A.12}$$

Note that the $\sigma_\lambda \sim \Lambda\sqrt{\sigma_n}$ trend is not limited to a Gaussian noise, although the parameter α_1 does depend on the specifics of the noise distribution. Following a similar line of discussion, it can be shown that if the first non-zero term is the fourth order term we would have $\sigma_\lambda \sim \Lambda\sqrt[4]{\sigma_n}$.

According to the above analysis, the behavior of σ_λ is mainly dominated by Λ and σ_n. In the next step, in order to include the smaller effect of δ as well, I let α_1 be a function of δ (normalized to the linewidth Λ) so that:

$$\sigma_\lambda(\Lambda, \sigma_n, \delta) \approx \Lambda\sqrt{\sigma_n}\ \alpha_1(\frac{\delta}{\Lambda}). \tag{A.13}$$

Finding a general relation for α_1 is involved. However, the asymptotic behavior of $\alpha_1(\delta/\Lambda)$ at $\delta/\Lambda \to 0$ provides helpful insight. Although in practice one may design the system at non-asymptotic regimes of sampling resolution, the study of this regime reveals the principle trends in σ_λ, based on which some parametric models can be proposed to cover both asymptotic and non-asymptotic regimes accurately. The importance of these parametric models is discussed in Section 4.3.1.

Let us assume that the resonance function is densely sampled so that $\delta \ll \Lambda, \sigma_\lambda$. Now consider the case of doubling the sampling density. We can assume that each single sample will be replaced by a bundle of two adjacent samples, $\delta/2$ apart in their wavelength. Within each bundle represented by $\{D_i \text{ and } D_{i+1}\}$, we can discard the larger sample, because the larger sample will not be the *absolute minimum* of the whole data set. Since $\delta \ll \Lambda$, we have $R_i \simeq R_{i+1}$. So, the same argument for D can be extended to the noise because $D_i = R_i + n_i$. That is to say, within each bundle, the sample with larger noise (n_i or n_{i+1}) will be discarded; and I only keep the sample with smaller noise as the dominant sample of the bundle. The dominant noise of this bundle will then be a random variable defined as $n_{min(2)} = min\{n_i, n_{i+1}\}$. As a result, doubling the sampling resolution (as far as σ_λ is concerned) is equivalent to replacing the distribution function of n with that of $n_{min(2)}$ (without doubling the sampling resolution). Similar argument can be made for the case of an m-fold increase in the sampling resolution: changing the sampling resolution from δ to δ/m is equivalent to replacing $p_n(n)$ with $p_N(n)$, which is the p.d.f of the random variable N defined as the minimum of m iid random variables with a p.d.f of $p_n(n)$.

According to extreme value theory, for any well-behaved [160] p.d.f $p_n(n)$, there exists scaling factors $a_m > 0$ and b_m such that:

$$\lim_{m\to\infty} Q_N(a_m^{-1}n + b_m) = Q_n^m(a_m^{-1}n + b_m) \to G(n) \triangleq e^{-e^{-n}}, \tag{A.14}$$

where Q_n and Q_N are defined according to Equation A.3 for the noise (n), and for

the minimum of a bundle of m noise samples (N). In general, $G(n)$ is the cumulative distribution function of one of three well known *extreme distributions*: Gumbel, Frechet, Weibull. However, for the majority of noise statistics of practical interest, $G(n)$ is the Gumbel distribution as defined in Equation A.14. Thus,

$$\sigma_\lambda(\Lambda, \sigma_n, \delta) = \sigma_{G,\lambda}(\Lambda, \frac{1}{a_m}\sigma_n, m\delta). \tag{A.15}$$

Note that the σ_λ on the left corresponds to any arbitrary distribution function within Gumbel domain of attraction [159], while the $\sigma_{G,\lambda}$ on the right corresponds to that for a Gumbel distribution. Using Equations A.7 and A.8 we have

$$\begin{aligned}\sigma_\lambda(\Lambda, \sigma_n, \delta) &= \sigma_{G,\lambda}(\frac{1}{\sqrt{a_m}}\Lambda, \sigma_n, m\delta) \\ &= \frac{1}{\sqrt{a_m}}\sigma_{G,\lambda}(\Lambda, \sigma_n, m\sqrt{a_m}\delta).\end{aligned} \tag{A.16}$$

To simplify the relations, I define:

$$k \triangleq m\sqrt{a_m} \approx A_1 m^{1+\epsilon_1}, \tag{A.17}$$

with which Equation A.16 turns to

$$\sigma_\lambda(\Lambda, \sigma_n, \delta) = \frac{1}{\sqrt{a_m}}\sigma_{G,\lambda}(\Lambda, \sigma_n, k\delta). \tag{A.18}$$

This relation is important as it expresses the scaling behavior of σ_λ with δ. Changing the sampling resolution from δ to δ/k scales σ_λ with $1/\sqrt{a_m}$, where $m \approx A_2 k^{1+\epsilon_2} \approx A(\Lambda/\delta)^{1+\epsilon}$. This approximation leads to

$$\alpha_1(\frac{\delta}{\Lambda}) = \frac{A}{\sqrt{a_m}};\ \text{where } m = B(\frac{\Lambda}{\delta})^{1+\epsilon}. \tag{A.19}$$

A, B, and ϵ parameters depend on the noise statistics. I will use this parametric model in in Section 4.3.1 to propose accurate estimates for $\alpha_1(\frac{\delta}{\Lambda})$.

APPENDIX B

BINDING DYNAMICS MODEL

Simultaneous presence of multiple active molecules in the solution results in a competition among them in binding to the recognition elements. Here a simple model of the dynamics of the binding is presented. For every binding site containing a single glycan; G; n different lectins; $L_1, ..., L_n$; compete for binding. Changes in the number of glycans bound to a specific lectin L_i, denoted as $GL_i(t)$, obeys:

$$\frac{d}{dt}GL_i(t) = k_{a,i}C_i(G - \sum_{j=1}^{n} GL_j(t)) - k_{d,i}GL_i(t), \tag{B.1}$$

where $k_{a,i}$ and $k_{d,i}$ are association and dissociation constants for this glycan(G)/lectin(L_i) pair. C_i is the concentration of the lectin L_i, and G is total number of glycan molecules available on the surface. Represented in matrix form, we have:

$$\frac{d}{dt}\mathbf{GL}(t) = \mathbf{B}G - \mathbf{A}.\mathbf{GL}(t), \tag{B.2}$$

$$\mathbf{A} = \begin{bmatrix} k_{a,1} & 0 & 0 \\ 0 & ... & 0 \\ 0 & 0 & k_{a,n} \end{bmatrix} . \mathbf{C} . [1 \ ... \ 1]_{1\times n} - \begin{bmatrix} k_{d,1} & 0 & 0 \\ 0 & ... & 0 \\ 0 & 0 & k_{d,n} \end{bmatrix} .$$

$$\mathbf{B} = \begin{bmatrix} k_{a,1} & 0 & 0 \\ 0 & ... & 0 \\ 0 & 0 & k_{a,n} \end{bmatrix} \mathbf{C}.$$

$$\mathbf{C} = \begin{bmatrix} C_1 \\ ... \\ C_n \end{bmatrix}.$$

At steady state, rearranging this formula yields

$$\mathbf{GL}(\infty) = \mathbf{A^{-1}B}G. \tag{B.3}$$

Since different lectins have different masses, the resonance shift (which is *the observable* here) is approximately a weighted sum of the number of bound glycan/lectin pairs (GL_i), with the weights proportional to the molecular mass of the lectin. The response in terms of resonance shift is

$$R(t) = \delta\lambda_{1Da} \sum_{i=1}^{n} M_i \; GL_i(t), \tag{B.4}$$

where M_i is the molecular mass of the lectin L_i and $\delta\lambda_{1Da}$ is the resonance shift per one Dalton of bound mass ($\sim 1\,\mathrm{am}$). I assume the volume of the molecule linearly depends on its molecular mass, and that the refractive index is almost uniform over the volume of the molecule. As a result, the resonance shifts linearly with the captured mass. At steady state, Equation (B.4) can be further simplified using Equation (B.2) to

$$R(\infty) = \delta\lambda_{1Da} \; \mathbf{M} \; \mathbf{GL}(\infty) = \delta\lambda_{1Da} \; \mathbf{M} \; \mathbf{A^{-1}} \; \mathbf{B} \; G, \tag{B.5}$$

$$\mathbf{M} = [M_1 \; ... \; M_n]$$

This formula is then used to calculate the expected resonance shift in terms of concentrations (which appear in the definitions of $\mathbf{A}$ and $\mathbf{B}$).

Bibliography

[1] "Biosensors - a global market overview," ReportLinker, Tech. Rep., March 2012.

[2] "Biophotonics market: Focus on life sciences & health applications," Yole Dveloppement, Tech. Rep., April 2013.

[3] D. R. Thévenot, K. Toth, R. A. Durst, and G. S. Wilson, "Electrochemical biosensors: recommended definitions and classification," *Biosensors and Bioelectronics*, vol. 16, no. 1, pp. 121–131, 2001.

[4] X. Fan, I. M. White, S. I. Shopova, H. Zhu, J. D. Suter, and Y. Sun, "Sensitive optical biosensors for unlabeled targets: A review," *analytica chimica acta*, vol. 620, no. 1, pp. 8–26, 2008.

[5] C. Hagleitner, A. Hierlemann, D. Lange, A. Kummer, N. Kerness, O. Brand, and H. Baltes, "Smart single-chip gas sensor microsystem," *Nature*, vol. 414, no. 6861, pp. 293–296, 2001.

[6] T. G. Drummond, M. G. Hill, and J. K. Barton, "Electrochemical dna sensors," *Nature biotechnology*, vol. 21, no. 10, pp. 1192–1199, 2003.

[7] J. Wang, "Electrochemical biosensors: towards point-of-care cancer diagnostics," *Biosensors and Bioelectronics*, vol. 21, no. 10, pp. 1887–1892, 2006.

[8] M. Abdolahad, M. Taghinejad, H. Taghinejad, M. Janmaleki, and S. Mohajerzadeh, "A vertically aligned carbon nanotube-based impedance sensing biosensor for rapid and high sensitive detection of cancer cells," *Lab on a Chip*, vol. 12, no. 6, pp. 1183–1190, 2012.

[9] R. Thusu, "Strong growth predicted for biosensors market," Frost & Sullivan, Tech. Rep., October 2010.

[10] J. Arlett, E. Myers, and M. Roukes, "Comparative advantages of mechanical biosensors," *Nature nanotechnology*, vol. 6, no. 4, pp. 203–215, 2011.

[11] N. Backmann, C. Zahnd, F. Huber, A. Bietsch, A. Plückthun, H.-P. Lang, H.-J. Güntherodt, M. Hegner, and C. Gerber, "A label-free immunosensor array using single-chain antibody fragments," *Proceedings of the National Academy of Sciences of the United States of America*, vol. 102, no. 41, pp. 14 587–14 592, 2005.

[12] T. Braun, M. K. Ghatkesar, N. Backmann, W. Grange, P. Boulanger, L. Letellier, H.-P. Lang, A. Bietsch, C. Gerber, and M. Hegner, "Quantitative time-resolved measurement of membrane protein–ligand interactions using microcantilever array sensors," *Nature nanotechnology*, vol. 4, no. 3, pp. 179–185, 2009.

[13] T. Braun, V. Barwich, M. K. Ghatkesar, A. H. Bredekamp, C. Gerber, M. Hegner, and H. P. Lang, "Micromechanical mass sensors for biomolecular detection in a physiological environment," *Physical Review E*, vol. 72, no. 3, p. 031907, 2005.

[14] M. K. Ghatkesar, V. Barwich, T. Braun, J.-P. Ramseyer, C. Gerber, M. Hegner, H. P. Lang, U. Drechsler, and M. Despont, "Higher modes of vibration increase mass sensitivity in nanomechanical microcantilevers," *Nanotechnology*, vol. 18, no. 44, p. 445502, 2007.

[15] M. G. von Muhlen, N. D. Brault, S. M. Knudsen, S. Jiang, and S. R. Manalis, "Label-free biomarker sensing in undiluted serum with suspended microchannel resonators," *Analytical chemistry*, vol. 82, no. 5, pp. 1905–1910, 2010.

[16] P. S. Waggoner, M. Varshney, and H. G. Craighead, "Detection of prostate

specific antigen with nanomechanical resonators," *Lab on a Chip*, vol. 9, no. 21, pp. 3095–3099, 2009.

[17] N. Kim, D.-K. Kim, and Y.-J. Cho, "Development of indirect-competitive quartz crystal microbalance immunosensor for c-reactive protein," *Sensors and Actuators B: Chemical*, vol. 143, no. 1, pp. 444–448, 2009.

[18] S. Kurosawa, M. Nakamura, J.-W. Park, H. Aizawa, K. Yamada, and M. Hirata, "Evaluation of a high-affinity qcm immunosensor using antibody fragmentation and 2-methacryloyloxyethyl phosphorylcholine (mpc) polymer," *Biosensors and Bioelectronics*, vol. 20, no. 6, pp. 1134–1139, 2004.

[19] J. Kirsch, C. Siltanen, Q. Zhou, A. Revzin, and A. Simonian, "Biosensor technology: recent advances in threat agent detection and medicine," *Chemical Society Reviews*, vol. 42, no. 22, pp. 8733–8768, 2013.

[20] N. J. Ronkainen, H. B. Halsall, and W. R. Heineman, "Electrochemical biosensors," *Chemical Society Reviews*, vol. 39, no. 5, pp. 1747–1763, 2010.

[21] M. Pumera, S. Sanchez, I. Ichinose, and J. Tang, "Electrochemical nanobiosensors," *Sensors and Actuators B: Chemical*, vol. 123, no. 2, pp. 1195–1205, 2007.

[22] B. Munge, G. Liu, G. Collins, and J. Wang, "Multiple enzyme layers on carbon nanotubes for electrochemical detection down to 80 dna copies," *Analytical chemistry*, vol. 77, no. 14, pp. 4662–4666, 2005.

[23] N. Zhu, Z. Chang, P. He, and Y. Fang, "Electrochemical dna biosensors based on platinum nanoparticles combined carbon nanotubes," *Analytica chimica acta*, vol. 545, no. 1, pp. 21–26, 2005.

[24] T. M. Squires, R. J. Messinger, and S. R. Manalis, "Making it stick: convection, reaction and diffusion in surface-based biosensors," *Nature biotechnology*, vol. 26, no. 4, pp. 417–426, 2008.

[25] E. Stern, J. F. Klemic, D. A. Routenberg, P. N. Wyrembak, D. B. Turner-Evans, A. D. Hamilton, D. A. LaVan, T. M. Fahmy, and M. A. Reed, "Label-free immunodetection with cmos-compatible semiconducting nanowires," *Nature*, vol. 445, no. 7127, pp. 519–522, 2007.

[26] E. Stern, R. Wagner, F. J. Sigworth, R. Breaker, T. M. Fahmy, and M. A. Reed, "Importance of the debye screening length on nanowire field effect transistor sensors," *Nano letters*, vol. 7, no. 11, pp. 3405–3409, 2007.

[27] J. H. Chua, R.-E. Chee, A. Agarwal, S. M. Wong, and G.-J. Zhang, "Label-free electrical detection of cardiac biomarker with complementary metal-oxide semiconductor-compatible silicon nanowire sensor arrays," *Analytical chemistry*, vol. 81, no. 15, pp. 6266–6271, 2009.

[28] M. M.-C. Cheng, G. Cuda, Y. L. Bunimovich, M. Gaspari, J. R. Heath, H. D. Hill, C. A. Mirkin, A. J. Nijdam, R. Terracciano, T. Thundat *et al.*, "Nanotechnologies for biomolecular detection and medical diagnostics," *Current opinion in chemical biology*, vol. 10, no. 1, pp. 11–19, 2006.

[29] J. Homola, "Surface plasmon resonance sensors for detection of chemical and biological species," *Chemical reviews*, vol. 108, no. 2, pp. 462–493, 2008.

[30] S. Roh, T. Chung, and B. Lee, "Overview of the characteristics of micro-and nano-structured surface plasmon resonance sensors," *Sensors*, vol. 11, no. 2, pp. 1565–1588, 2011.

[31] Y. Gao, Z. Xin, B. Zeng, Q. Gan, X. Cheng, and F. J. Bartoli, "Plasmonic

interferometric sensor arrays for high-performance label-free biomolecular detection," *Lab on a Chip*, vol. 13, no. 24, pp. 4755–4764, 2013.

[32] E. Petryayeva and U. J. Krull, "Localized surface plasmon resonance: nanostructures, bioassays and biosensinga review," *Analytica chimica acta*, vol. 706, no. 1, pp. 8–24, 2011.

[33] K. A. Willets and R. P. Van Duyne, "Localized surface plasmon resonance spectroscopy and sensing," *Annu. Rev. Phys. Chem.*, vol. 58, pp. 267–297, 2007.

[34] M. Piliarik, H. Šípová, P. Kvasnička, N. Galler, J. R. Krenn, and J. Homola, "High-resolution biosensor based on localized surface plasmons," *Optics Express*, vol. 20, no. 1, pp. 672–680, 2012.

[35] S. Chen, M. Svedendahl, M. Käll, L. Gunnarsson, and A. Dmitriev, "Ultrahigh sensitivity made simple: nanoplasmonic label-free biosensing with an extremely low limit-of-detection for bacterial and cancer diagnostics," *Nanotechnology*, vol. 20, no. 43, p. 434015, 2009.

[36] K. M. Mayer, F. Hao, S. Lee, P. Nordlander, and J. H. Hafner, "A single molecule immunoassay by localized surface plasmon resonance," *Nanotechnology*, vol. 21, no. 25, p. 255503, 2010.

[37] V. Dantham, S. Holler, V. Kolchenko, Z. Wan, and S. Arnold, "Taking whispering gallery-mode single virus detection and sizing to the limit," *Applied Physics Letters*, vol. 101, no. 4, pp. 043 704–043 704, 2012.

[38] S. Arnold, V. R. Dantham, S. Holler, C. Barbre, D. Keng, and V. Kolchenko, "Label-free detection of single protein using a nanoplasmonic-photonic hybrid microcavity," *Nano Letters*, 2013.

[39] R. Polzius, E. Dießel, F. F. Bier, and U. Bilitewski, "Real-time observation of affinity reactions using grating couplers: determination of the detection limit and calculation of kinetic rate constants," *Analytical biochemistry*, vol. 248, no. 2, pp. 269–276, 1997.

[40] L. H. Rindorf, J. B. Jensen, H. M. Dufva, L. H. Pedersen, P. E. Hoiby, and O. Bang, "Photonic crystal fiber long-period gratings for biochemical sensing," *Optics Express*, vol. 14, no. 18, pp. 8224–8231, 2006.

[41] R. Heideman, R. Kooyman, and J. Greve, "Performance of a highly sensitive optical waveguide mach-zehnder interferometer immunosensor," *Sensors and Actuators B: Chemical*, vol. 10, no. 3, pp. 209–217, 1993.

[42] A. Densmore, M. Vachon, D.-X. Xu, S. Janz, R. Ma, Y.-H. Li, G. Lopinski, A. Delâge, J. Lapointe, C. Luebbert *et al.*, "Silicon photonic wire biosensor array for multiplexed, real-time and label-free molecular detection," *Optics letters*, vol. 34, no. 23, pp. 3598–3600, 2009.

[43] A. Brandenburg and R. Henninger, "Integrated optical young interferometer," *Applied optics*, vol. 33, no. 25, pp. 5941–5947, 1994.

[44] J. Xu, D. Suarez, and D. S. Gottfried, "Detection of avian influenza virus using an interferometric biosensor," *Analytical and bioanalytical chemistry*, vol. 389, no. 4, pp. 1193–1199, 2007.

[45] M. J. Swann, L. L. Peel, S. Carrington, and N. J. Freeman, "Dual-polarization interferometry: an analytical technique to measure changes in protein structure in real time, to determine the stoichiometry of binding events, and to differentiate between specific and nonspecific interactions," *Analytical biochemistry*, vol. 329, no. 2, pp. 190–198, 2004.

[46] A. Ymeti, J. Kanger, J. Greve, G. Besselink, P. Lambeck, R. Wijn, and R. Heideman, "Integration of microfluidics with a four-channel integrated optical young interferometer immunosensor," *Biosensors and Bioelectronics*, vol. 20, no. 7, pp. 1417–1421, 2005.

[47] E. Chow, A. Grot, L. Mirkarimi, M. Sigalas, and G. Girolami, "Ultracompact biochemical sensor built with two-dimensional photonic crystal microcavity," *Optics letters*, vol. 29, no. 10, pp. 1093–1095, 2004.

[48] S. Mandal and D. Erickson, "Nanoscale optofluidic sensor arrays," *Optics Express*, vol. 16, no. 3, p. 1623, 2008.

[49] D. Dorfner, T. Zabel, T. Hürlimann, N. Hauke, L. Frandsen, U. Rant, G. Abstreiter, and J. Finley, "Photonic crystal nanostructures for optical biosensing applications," *Biosensors and Bioelectronics*, vol. 24, no. 12, pp. 3688–3692, 2009.

[50] A. Di Falco, L. OFaolain, and T. Krauss, "Chemical sensing in slotted photonic crystal heterostructure cavities," *Applied physics letters*, vol. 94, no. 6, pp. 063 503–063 503, 2009.

[51] F. Liang, N. Clarke, P. Patel, M. Loncar, and Q. Quan, "Scalable photonic crystal chips for high sensitivity protein detection," *Optics Express*, vol. 21, no. 26, pp. 32 306–32 312, 2013.

[52] Q. Quan, D. L. Floyd, I. B. Burgess, P. B. Deotare, I. W. Frank, S. K. Tang, R. Ilic, and M. Loncar, "Single particle detection in cmos compatible photonic crystal nanobeam cavities," *Optics Express*, vol. 21, no. 26, pp. 32 225–32 233, 2013.

[53] F. Vollmer, S. Arnold, and D. Keng, "Single virus detection from the reactive

shift of a whispering-gallery mode," *Proceedings of the National Academy of Sciences*, vol. 105, no. 52, pp. 20 701–20 704, 2008.

[54] T. Lu, H. Lee, T. Chen, S. Herchak, J.-H. Kim, S. E. Fraser, R. C. Flagan, and K. Vahala, "High sensitivity nanoparticle detection using optical microcavities," *Proceedings of the National Academy of Sciences*, vol. 108, no. 15, pp. 5976–5979, 2011.

[55] M. Soltani, S. Yegnanarayanan, and A. Adibi, "Ultra-high q planar silicon microdisk resonators for chip-scale silicon photonics," *Optics express*, vol. 15, no. 8, pp. 4694–4704, 2007.

[56] E. Shah Hosseini, S. Yegnanarayanan, A. H. Atabaki, M. Soltani, and A. Adibi, "High quality planar silicon nitride microdisk resonators for integrated photonics in the visible wavelength range," *Optics express*, vol. 17, no. 17, pp. 14 543–14 551, 2009.

[57] M. Sodagar, A. H. Hosseinnia, H. Moradinejad, A. H. Atabaki, A. A. Eftekhar, and A. Adibi, "Field-programmable optical devices based on resonance elimination," *Optics letters*, vol. 39, no. 15, pp. 4545–4548, 2014.

[58] C.-Y. Chao, W. Fung, and L. J. Guo, "Polymer microring resonators for biochemical sensing applications," *Selected Topics in Quantum Electronics, IEEE Journal of*, vol. 12, no. 1, pp. 134–142, 2006.

[59] K. De Vos, J. Girones, S. Popelka, E. Schacht, R. Baets, and P. Bienstman, "Soi optical microring resonator with poly (ethylene glycol) polymer brush for label-free biosensor applications," *Biosensors and Bioelectronics*, vol. 24, no. 8, pp. 2528–2533, 2009.

[60] R. Orghici, P. Lützow, J. Burgmeier, J. Koch, H. Heidrich, W. Schade, N. Welschoff, and S. Waldvogel, "A microring resonator sensor for sensitive

detection of 1, 3, 5-trinitrotoluene (tnt)," *Sensors*, vol. 10, no. 7, pp. 6788–6795, 2010.

[61] Y. Sun and X. Fan, "Optical ring resonators for biochemical and chemical sensing," *Analytical and bioanalytical chemistry*, vol. 399, no. 1, pp. 205–211, 2011.

[62] F. Ghasemi, A. A. Eftekhar, D. S. Gottfried, X. Song, R. D. Cummings, and A. Adibi, "Self-referenced silicon nitride array microring biosensor for toxin detection using glycans at visible wavelength," in *SPIE BiOS*. International Society for Optics and Photonics, 2013, pp. 85 940A–85 940A.

[63] M. Soltani, "Novel integrated silicon nanophotonic structures using ultra-high Q resonators," Ph.D. dissertation, Georgia Institute of Technology, 2009.

[64] A. H. Atabaki, "Reconfigurable silicon photonic devices for optical signal processing," Ph.D. dissertation, Georgia Institute of Technology, 2011.

[65] Q. Li, "Densely integrated photonic structures for on-chip signal processing," Ph.D. dissertation, Georgia Institute of Technology, 2013.

[66] D. G. Rabus, *Integrated ring resonators*. Springer, 2007.

[67] A. W. Snyder and J. Love, *Optical waveguide theory*. Springer, 1983, vol. 190.

[68] T. Claes, W. Bogaerts, and P. Bienstman, "Experimental characterization of a silicon photonic biosensor consisting of two cascaded ring resonators based on the vernier-effect and introduction of a curve fitting method for an improved detection limit," *Optics express*, vol. 18, no. 22, pp. 22 747–22 761, 2010.

[69] R. Heideman, M. Hoekman, and E. Schreuder, "Triplex-based integrated optical ring resonators for lab-on-a-chip and environmental detection," *Selected Topics in Quantum Electronics, IEEE Journal of*, vol. 18, no. 5, pp. 1583–1596, 2012.

[70] S. Lee, S. C. Eom, J. S. Chang, C. Huh, G. Y. Sung, and J. H. Shin, "Label-free optical biosensing using a horizontal air-slot sin¡ sub¿ x¡/sub¿ microdisk resonator," *Optics express*, vol. 18, no. 20, pp. 20 638–20 644, 2010.

[71] C. Ciminelli, F. Dell'Olio, M. N. Armenise, F. M. Soares, and W. Passenberg, "High performance inp ring resonator for new generation monolithically integrated optical gyroscopes," *Optics express*, vol. 21, no. 1, pp. 556–564, 2013.

[72] K. B. Gylfason, C. F. Carlborg, A. Kazmierczak, F. Dortu, L. Vivien, C. A. Barrios, W. van der Wijngaart, G. Stemme *et al.*, "On-chip temperature compensation in an integrated slot-waveguide ring resonator refractive index sensor array," *Optics Express*, vol. 18, no. 4, pp. 3226–3237, 2010.

[73] J. T. Kirk, G. E. Fridley, J. W. Chamberlain, E. D. Christensen, M. Hochberg, and D. M. Ratner, "Multiplexed inkjet functionalization of silicon photonic biosensors," *Lab on a Chip*, vol. 11, no. 7, pp. 1372–1377, 2011.

[74] F. G. Della Corte, G. Cocorullo, M. Iodice, and I. Rendina, "Temperature dependence of the thermo-optic coefficient of inp, gaas, and sic from room temperature to 600 k at the wavelength of 1.5 μm," *Applied physics letters*, vol. 77, no. 11, pp. 1614–1616, 2000.

[75] A. Arbabi and L. L. Goddard, "Measurements of the refractive indices and thermo-optic coefficients of si3n4 and siox using microring resonances," *Optics letters*, vol. 38, no. 19, pp. 3878–3881, 2013.

[76] G. Gülşen and M. Naci Inci, "Thermal optical properties of tio¡ sub¿ 2¡/sub¿ films," *Optical materials*, vol. 18, no. 4, pp. 373–381, 2002.

[77] L. Kou, D. Labrie, and P. Chylek, "Refractive indices of water and ice in the 0.65-to 2.5-μm spectral range," *Applied Optics*, vol. 32, no. 19, pp. 3531–3540, 1993.

[78] F. Ghasemi, M. Chamanzar, E. Hosseini, A. Eftekhar, Q. Li, A. Atabaki, and A. Adibi, "Compact fluorescence sensor using on-chip silicon nitride microdisk," in *Photonics Conference (PHO), 2011 IEEE*. IEEE, 2011, pp. 151–152.

[79] Y. Chen, Z. Li, H. Yi, Z. Zhou, and J. Yu, "Microring resonator for glucose sensing applications," *Frontiers of Optoelectronics in China*, vol. 2, no. 3, pp. 304–307, 2009.

[80] C. A. Barrios, B. Sánchez, K. B. Gylfason, A. Griol, H. Sohlström, M. Holgado, and R. Casquel, "Demonstration of slot-waveguide structures on silicon nitride/silicon oxide platform," *Optics express*, vol. 15, no. 11, pp. 6846–6856, 2007.

[81] I. Goykhman, B. Desiatov, and U. Levy, "Ultrathin silicon nitride microring resonator for biophotonic applications at 970 nm wavelength," *Applied Physics Letters*, vol. 97, no. 8, pp. 081 108–081 108, 2010.

[82] L. Jin, M. Li, and J.-J. He, "Highly-sensitive silicon-on-insulator sensor based on two cascaded micro-ring resonators with vernier effect," *Optics Communications*, vol. 284, no. 1, pp. 156–159, 2011.

[83] S. T. Fard, V. Donzella, S. A. Schmidt, J. Flueckiger, S. M. Grist, P. Talebi Fard, Y. Wu, R. J. Bojko, E. Kwok, N. A. Jaeger *et al.*, "Performance of ultra-thin soi-based resonators for sensing applications," *Optics Express*, vol. 22, no. 12, pp. 14 166–14 179, 2014.

[84] I. M. White and X. Fan, "On the performance quantification of resonant refractive index sensors," *Optics Express*, vol. 16, no. 2, pp. 1020–1028, 2008.

[85] D. F. Smith, X. Song, and R. D. Cummings, "Chapter nineteen-use of glycan microarrays to explore specificity of glycan-binding proteins," *Methods in enzymology*, vol. 480, pp. 417–444, 2010.

[86] K. De Vos, I. Bartolozzi, E. Schacht, P. Bienstman, and R. Baets, "Silicon-on-insulator microring resonator for sensitive and label-free biosensing," *Opt. Express*, vol. 15, no. 12, pp. 7610–7615, 2007.

[87] F. Ghasemi, H. Zhou, and A. Adibi, "The effect of amplitude noise on the accuracy of resonance detection using spectrum scans," unpublished manuscript.

[88] M. Soltani, S. Yegnanarayanan, Q. Li, and A. Adibi, "Systematic engineering of waveguide-resonator coupling for silicon microring/microdisk/racetrack resonators: theory and experiment," *Quantum Electronics, IEEE Journal of*, vol. 46, no. 8, pp. 1158–1169, 2010.

[89] E. Shah Hosseini, S. Yegnanarayanan, A. H. Atabaki, M. Soltani, and A. Adibi, "Systematic design and fabrication of high-q single-mode pulley-coupled planar silicon nitride microdisk resonators at visible wavelengths," *Optics express*, vol. 18, no. 3, pp. 2127–2136, 2010.

[90] D. A. Lauffenburger and J. J. Linderman, *Receptors: models for binding, trafficking, and signaling*. Oxford University Press New York:, 1993, vol. 365.

[91] A. R. Goldfarb, L. J. Saidel, and E. Mosovich, "The ultraviolet absorption spectra of proteins," *Journal of Biological Chemistry*, vol. 193, no. 1, pp. 397–404, 1951.

[92] J. Kim, P. Seidler, C. Fill, and L. S. Wan, "Investigations of the effect of curing conditions on the structure and stability of amino-functionalized organic films on silicon substrates by Fourier transform infrared spectroscopy, ellipsometry, and fluorescence microscopy," *Surface Science*, vol. 602, no. 21, pp. 3323–3330, Nov. 2008.

[93] E. A. Smith and W. Chen, "How to prevent the loss of surface functionality derived from aminosilanes," *Langmuir*, vol. 24, no. 21, pp. 12 405–12 409, 2008.

[94] X. Song, B. Xia, S. R. Stowell, Y. Lasanajak, D. F. Smith, and R. D. Cummings, "Novel fluorescent glycan microarray strategy reveals ligands for galectins," *Chemistry & biology*, vol. 16, no. 1, pp. 36–47, 2009.

[95] S. von Gunten, D. F. Smith, R. D. Cummings, S. Riedel, S. Miescher, A. Schaub, R. G. Hamilton, and B. S. Bochner, "Intravenous immunoglobulin contains a broad repertoire of anticarbohydrate antibodies that is not restricted to the IgG2 subclass." *The Journal of allergy and clinical immunology*, vol. 123, no. 6, pp. 1268–76.e15, Jun. 2009.

[96] J. H. Lee, Y.-A. Song, and J. Han, "Multiplexed proteomic sample preconcentration device using surface-patterned ion-selective membrane," *Lab on a Chip*, vol. 8, no. 4, pp. 596–601, 2008.

[97] X. Quan and E. S. Fry, "Empirical equation for the index of refraction of seawater," *Applied Optics*, vol. 34, no. 18, pp. 3477–3480, 1995.

[98] F. Ghasemi, M. Chamanzar, A. A. Eftekhar, and A. Adibi, "An efficient technique for the reduction of wavelength noise in resonance-based integrated photonic sensors," *Analyst*, 2014.

[99] M. S. Luchansky, A. L. Washburn, T. A. Martin, M. Iqbal, L. C. Gunn, and R. C. Bailey, "Characterization of the evanescent field profile and bound mass sensitivity of a label-free silicon photonic microring resonator biosensing platform," *Biosensors and Bioelectronics*, vol. 26, no. 4, pp. 1283–1291, 2010.

[100] D. Xu, A. Densmore, A. Delâge, P. Waldron, R. McKinnon, S. Janz, J. Lapointe, G. Lopinski, T. Mischki, E. Post *et al.*, "Folded cavity soi microring sensors for high sensitivity and real time measurement of biomolecular binding," *Optics Express*, vol. 16, no. 19, pp. 15 137–15 148, 2008.

[101] H. Zhu, I. M. White, J. D. Suter, P. S. Dale, and X. Fan, "Analysis of biomolecule detection with optofluidic ring resonator sensors," *Optics Express*, vol. 15, no. 15, pp. 9139–9146, 2007.

[102] L. F. Cheow, A. Sarkar, S. E. Kolitz, D. A. Lauffenburger, and J. Han, "Detecting kinase activities from single cell lysate using concentration-enhanced mobility shift assay," *Analytical chemistry*, vol. 86, no. 15, pp. 7455–7462, 2014.

[103] R. Kwak, S. J. Kim, and J. Han, "Continuous-flow biomolecule and cell concentrator by ion concentration polarization," *Analytical chemistry*, vol. 83, no. 19, pp. 7348–7355, 2011.

[104] D. Vernooy, V. S. Ilchenko, H. Mabuchi, E. Streed, and H. Kimble, "High-q measurements of fused-silica microspheres in the near infrared," *Optics Letters*, vol. 23, no. 4, pp. 247–249, 1998.

[105] L. M. Freeman and A. M. Armani, "Photobleaching of cy5 conjugated lipid bilayers determined with optical microresonators," *Selected Topics in Quantum Electronics, IEEE Journal of*, vol. 18, no. 3, pp. 1160–1165, 2012.

[106] J. Hu, X. Sun, A. Agarwal, and L. C. Kimerling, "Design guidelines for optical resonator biochemical sensors," *JOSA B*, vol. 26, no. 5, pp. 1032–1041, 2009.

[107] R. Yan, S. P. Mestas, G. Yuan, R. Safaisini, and K. L. Lear, "Response of local evanescent array-coupled biosensors to organic nanofilms," *Selected Topics in Quantum Electronics, IEEE Journal of*, vol. 15, no. 5, pp. 1469–1477, 2009.

[108] B. E. Saleh and M. Teich, "Fundamentals of photonics wiley series in pure and applied optics," *NY, NY*, 1991.

[109] L. Chrostowski and M. Hochberg, *Silicon photonics design*. Lulu. com, 2013.

[110] E. Stenberg, B. Persson, H. Roos, and C. Urbaniczky, "Quantitative determination of surface concentration of protein with surface plasmon resonance using radiolabeled proteins," *Journal of colloid and interface science*, vol. 143, no. 2, pp. 513–526, 1991.

[111] S. Sjoelander and C. Urbaniczky, "Integrated fluid handling system for biomolecular interaction analysis," *Analytical Chemistry*, vol. 63, no. 20, pp. 2338–2345, 1991.

[112] K. S. Johnston, K. S. Booksh, T. M. Chinowsky, and S. S. Yee, "Performance comparison between high and low resolution spectrophotometers used in a white light surface plasmon resonance sensor," *Sensors and Actuators B: Chemical*, vol. 54, no. 1, pp. 80–88, 1999.

[113] K. Kukanskis, J. Elkind, J. Melendez, T. Murphy, G. Miller, and H. Garner, "Detection of dna hybridization using the tispr-1 surface plasmon resonance biosensor," *Analytical biochemistry*, vol. 274, no. 1, pp. 7–17, 1999.

[114] N. J. Goddard, D. Pollard-Knight, and C. H. Maule, "Real-time biomolecular interaction analysis using the resonant mirror sensor," *Analyst*, vol. 119, no. 4, pp. 583–588, 1994.

[115] T. M. Chinowsky, L. S. Jung, and S. S. Yee, "Optimal linear data analysis for surface plasmon resonance biosensors," *Sensors and Actuators B: Chemical*, vol. 54, no. 1, pp. 89–97, 1999.

[116] V. Thomsen, D. Schatzlein, and D. Mercuro, "Limits of detection in spectroscopy," *Spectroscopy*, vol. 18, no. 12, pp. 112–114, 2003.

[117] C. Jacoboni and P. Lugli, *The Monte Carlo method for semiconductor device simulation*. Springer, 1989, vol. 3.

[118] G. G. Nenninger, M. Piliarik, and J. Homola, "Data analysis for optical sensors based on spectroscopy of surface plasmons," *Measurement Science and Technology*, vol. 13, no. 12, p. 2038, 2002.

[119] G. A. Seber and A. J. Lee, *Linear regression analysis*. John Wiley & Sons, 2012, vol. 936.

[120] H. W. Ott and H. W. Ott, *Noise reduction techniques in electronic systems*. Wiley New York, 1988.

[121] J. J. Lillie, M. A. Thomas, N.-M. Jokerst, S. E. Ralph, K. A. Dennis, and C. L. Henderson, "Multimode interferometric sensors on silicon optimized for fully integrated complementary-metal-oxide-semiconductor chemical-biological sensor systems," *JOSA B*, vol. 23, no. 4, pp. 642–651, 2006.

[122] B. Luk'yanchuk, N. I. Zheludev, S. A. Maier, N. J. Halas, P. Nordlander, H. Giessen, and C. T. Chong, "The fano resonance in plasmonic nanostructures and metamaterials," *Nature materials*, vol. 9, no. 9, pp. 707–715, 2010.

[123] D. M. Bates and D. G. Watts, *Nonlinear regression: iterative estimation and linear approximations*. Wiley Online Library, 1988.

[124] A. Hassibi, H. Vikalo, and A. Hajimiri, "On noise processes and limits of performance in biosensors," *Journal of applied physics*, vol. 102, no. 1, pp. 014 909–014 909, 2007.

[125] Z. Mkhitaryan, A. Shatveryan, V. Aroutiounian, M. Ghulinyan, L. Pavesi, L. Kish, and C. G. Granqvist, "Current–voltage and low-frequency noise characteristics of structures with porous silicon layers exposed to different gases," *Physica E: Low-dimensional Systems and Nanostructures*, vol. 38, no. 1, pp. 160–163, 2007.

[126] K. De Vos, J. Girones, T. Claes, Y. De Koninck, S. Popelka, E. Schacht, R. Baets, and P. Bienstman, "Multiplexed antibody detection with an array of silicon-on-insulator microring resonators," *Photonics Journal, IEEE*, vol. 1, no. 4, pp. 225–235, 2009.

[127] M. Iqbal, M. A. Gleeson, B. Spaugh, F. Tybor, W. G. Gunn, M. Hochberg, T. Baehr-Jones, R. C. Bailey, and L. C. Gunn, "Label-free biosensor arrays based on silicon ring resonators and high-speed optical scanning instrumentation," *Selected Topics in Quantum Electronics, IEEE Journal of*, vol. 16, no. 3, pp. 654–661, 2010.

[128] X. S. Yao and L. Maleki, "Optoelectronic microwave oscillator," *JOSA B*, vol. 13, no. 8, pp. 1725–1735, 1996.

[129] L. Chrostowski, S. Grist, J. Flueckiger, W. Shi, X. Wang, E. Ouellet, H. Yun, M. Webb, B. Nie, and Z. Liang, "Silicon photonic resonator sensors and devices," in *SPIE LASE*. International Society for Optics and Photonics, 2012, pp. 823 620–823 620.

[130] K. Kurihara, K. Nakamura, and K. Suzuki, "Asymmetric spr sensor response curve-fitting equation for the accurate determination of spr resonance angle," *Sensors and Actuators B: Chemical*, vol. 86, no. 1, pp. 49–57, 2002.

[131] F. Ghasemi and A. Adibi, "An accurate interferometric referencing method for resonance tracking in lab-on-chip applications," in *Conference on Lasers and Electro-Optics*. Optical Society of America, 2014, p. STh4H.4.

[132] J. S. Orcutt, A. Khilo, C. W. Holzwarth, M. A. Popović, H. Li, J. Sun, T. Bonifield, R. Hollingsworth, F. X. Kärtner, H. I. Smith, V. Stojanovic, and R. J. Ram, "Nanophotonic integration in state-of-the-art cmos foundries," *Optics express*, vol. 19, no. 3, pp. 2335–2346, 2011.

[133] J. Teng, P. Dumon, W. Bogaerts, H. Zhang, X. Jian, X. Han, M. Zhao, G. Morthier, and R. Baets, "Athermal silicon-on-insulator ring resonators by overlaying a polymer cladding on narrowed waveguides," *Opt. Express*, vol. 17, no. 17, pp. 14 627–14 633, 2009.

[134] T. Retajczyk Jr and A. Sinha, "Elastic stiffness and thermal expansion coefficients of various refractory silicides and silicon nitride films," *Thin Solid Films*, vol. 70, no. 2, pp. 241–247, 1980.

[135] J.-H. Zhao, T. Ryan, P. S. Ho, A. J. McKerrow, and W.-Y. Shih, "Measurement of elastic modulus, poisson ratio, and coefficient of thermal expansion of on-wafer submicron films," *Journal of applied physics*, vol. 85, no. 9, pp. 6421–6424, 1999.

[136] P. Alipour, E. S. Hosseini, A. A. Eftekhar, B. Momeni, and A. Adibi, "Athermal performance in high-q polymer-clad silicon microdisk resonators," *Optics letters*, vol. 35, no. 20, pp. 3462–3464, 2010.

[137] M. L. Gorodetsky and I. S. Grudinin, "Fundamental thermal fluctuations in microspheres," *JOSA B*, vol. 21, no. 4, pp. 697–705, 2004.

[138] A. Yariv, *Introduction to optical electronics*. Holt, Rinehart and Winston, Inc., New York, NY, 1976.

[139] X. Zhou, L. Zhang, A. Armani, D. Zhang, X. Duan, J. Liu, H. Zhang, and W. Pang, "On-chip biological and chemical sensing with reversed fano lineshape enabled by embedded microring resonators," *Selected Topics in Quantum Electronics, IEEE Journal of*, vol. 20, no. 3, pp. 1–10, 2014.

[140] P. Bienstman, K. De Vos, T. Claes, P. Debackere, R. Baets, J. Girones, and E. Schacht, "Biosensors in silicon on insulator," *Proceedings of SPIE*, vol. 7220, pp. 72 200O–72 200O–9, 2009.

[141] V. M. Passaro and F. De Leonardis, "Modeling and design of a novel high-sensitivity electric field silicon-on-insulator sensor based on a whispering-gallery-mode resonator," *Selected Topics in Quantum Electronics, IEEE Journal of*, vol. 12, no. 1, pp. 124–133, 2006.

[142] M. J. Heck, H.-W. Chen, A. W. Fang, B. R. Koch, D. Liang, H. Park, M. N. Sysak, and J. E. Bowers, "Hybrid silicon photonics for optical interconnects," *Selected Topics in Quantum Electronics, IEEE Journal of*, vol. 17, no. 2, pp. 333–346, 2011.

[143] D. Liang and J. E. Bowers, "Recent progress in lasers on silicon," *Nature Photonics*, vol. 4, no. 8, pp. 511–517, 2010.

[144] F. Aflatouni and H. Hashemi, "Wideband tunable laser phase noise reduction using single sideband modulation in an electro-optical feed-forward scheme," *Optics Letters*, vol. 37, no. 2, pp. 196–198, 2012.

[145] M. G. Littman and H. J. Metcalf, "Spectrally narrow pulsed dye laser without beam expander," *Applied Optics*, vol. 17, no. 14, pp. 2224–2227, 1978.

[146] S. Lecomte, E. Fretel, G. Mileti, and P. Thomann, "Self-aligned extended-cavity diode laser stabilized by the zeeman effect on the cesium d_2 line," *Applied optics*, vol. 39, no. 9, pp. 1426–1429, 2000.

[147] J. Hall and S. Lee, "Interferometric real-time display of cw dye laser wavelength with sub-doppler accuracy," *Applied Physics Letters*, vol. 29, no. 6, pp. 367–369, 1976.

[148] P. Fox, R. Scholten, M. Walkiewicz, and R. Drullinger, "A reliable, compact, and low-cost michelson wavemeter for laser wavelength measurement," *American Journal of Physics*, vol. 67, p. 624, 1999.

[149] L. Gervais, N. De Rooij, and E. Delamarche, "Microfluidic chips for point-of-care immunodiagnostics," *Advanced Materials*, vol. 23, no. 24, pp. H151–H176, 2011.

[150] F. S. Apple and P. O. Collinson, "Analytical characteristics of high-sensitivity cardiac troponin assays," *Clinical chemistry*, vol. 58, no. 1, pp. 54–61, 2012.

[151] P. Peluso, D. S. Wilson, D. Do, H. Tran, M. Venkatasubbaiah, D. Quincy, B. Heidecker, K. Poindexter, N. Tolani, M. Phelan *et al.*, "Optimizing antibody immobilization strategies for the construction of protein microarrays," *Analytical Biochemistry*, vol. 312, no. 2, pp. 113–124, 2003.

[152] P. A. Kavsak, A. R. MacRae, M.-J. Yerna, and A. S. Jaffe, "Analytic and clinical utility of a next-generation, highly sensitive cardiac troponin i assay for early detection of myocardial injury," *Clinical chemistry*, vol. 55, no. 3, pp. 573–577, 2009.

[153] S. Konstantinides, A. Geibel, M. Olschewski, W. Kasper, N. Hruska, S. Jäckle, and L. Binder, "Importance of cardiac troponins i and t in risk stratification of patients with acute pulmonary embolism," *Circulation*, vol. 106, no. 10, pp. 1263–1268, 2002.

[154] A. Qureshi, Y. Gurbuz, and J. H. Niazi, "Biosensors for cardiac biomarkers detection: a review," *Sensors and Actuators B: Chemical*, vol. 171, pp. 62–76, 2012.

[155] T. Hutter, N. Bamiedakis, and S. R. Elliott, "Theoretical study of porous silicon waveguides and their applicability for vapour sensing," in *Proceedings of the COMSOL Conference 2010 Paris*. COMSOL, 2011.

[156] H. Taghinejad, M. Taghinejad, M. Abdolahad, A. Saeidi, and S. Mohajerzadeh, "Fabrication and modeling of high sensitivity humidity sensors based on doped

silicon nanowires," *Sensors and Actuators B: Chemical*, vol. 176, pp. 413–419, 2013.

[157] A. A. Eftekhar, Z. Xia, F. Ghasemi, and A. Adibi, "Ultra-compact multiplexed lab-on-chip sensors using miniaturized integrated photonic resonators," in *Photonics Conference (IPC), 2012 IEEE*. IEEE, 2012, pp. 439–440.

[158] P. Alipour, A. A. Eftekhar, A. H. Atabaki, Q. Li, S. Yegnanarayanan, C. K. Madsen, and A. Adibi, "Fully reconfigurable compact rf photonic filters using high-q silicon microdisk resonators," *Optics express*, vol. 19, no. 17, pp. 15 899–15 907, 2011.

[159] M. Leadbetter, G. Lindgren, and H. Rootzen, *Extreme and Related Properties of Random Sequences and Series*. Springer Verlag, New York, 1983.

[160] L. De Haan, "Sample extremes: an elementary introduction," *Statistica Neerlandica*, vol. 30, no. 4, pp. 161–172, 1976.